



**Michigan
Technological
University**

Michigan Technological University
Digital Commons @ Michigan Tech

Dissertations, Master's Theses and Master's Reports

2018

PROBING QUANTUM TRANSPORT IN THREE-TERMINAL NANOJUNCTIONS

Meghnath Jaishi

Michigan Technological University, mjaishi@mtu.edu

Copyright 2018 Meghnath Jaishi

Recommended Citation

Jaishi, Meghnath, "PROBING QUANTUM TRANSPORT IN THREE-TERMINAL NANOJUNCTIONS", Open Access Dissertation, Michigan Technological University, 2018.

<https://doi.org/10.37099/mtu.dc.etr/663>

Follow this and additional works at: <https://digitalcommons.mtu.edu/etr>

 Part of the [Condensed Matter Physics Commons](#)

PROBING QUANTUM TRANSPORT IN THREE-TERMINAL NANOFUNCTIONS

By

Meghnath Jaishi

A DISSERTATION

Submitted in partial fulfillment of the requirements for the degree of

DOCTOR OF PHILOSOPHY

In Physics

MICHIGAN TECHNOLOGICAL UNIVERSITY

2018

© 2018 Meghnath Jaishi

This dissertation has been approved in partial fulfillment of the requirements for the Degree of DOCTOR OF PHILOSOPHY in Physics.

Department of Physics

Dissertation Advisor: *Dr. Ranjit Pati*

Committee Member: *Dr. Ravindra Pandey*

Committee Member: *Dr. Maximilian J. Seel*

Committee Member: *Dr. Gregory M. Odegard*

Department Chair: *Dr. Ravindra Pandey*

To

My Parents

and to

Gyanu & Aadhya

Contents

List of Figures	xi
List of Tables	xxi
Acknowledgments	xxiii
Abstract	xxvii
1 Introduction	1
2 Density Functional Theory	7
2.1 Introduction	7
2.2 Many-Body Schrödinger Wave Equation	8
2.2.1 Born-Oppenheimer Approximation	9
2.3 Hartree Product	10
2.4 Slater Determinants	12
2.5 The Hartree-Fock Approximation	13
2.6 Thomas-Fermi Model	18
2.7 The Hohenberg-Kohn Theorem	20

2.8	The Kohn-Sham Approach	24
2.9	Local Density Approximation	27
2.10	General Gradient Approximation	29
2.11	Hybrid Functionals	30
3	Quantum Transport Theory	33
3.1	Introduction	33
3.2	An Overview of Fundamental Lengthscales in Solids	34
3.3	Device Modeling	37
3.3.1	Electronic Transport in a Nanoscale Junction: Landauer’s Ap- proach	39
3.3.2	Single Particle Many-Body Green’s Function Approach	45
3.3.3	Theory of Spin Transport	51
4	Semiconductor Core-Shell Nanowire Field Effect Transistors	55
4.1	Introduction	55
4.2	Superior Performance of a Si-Ge Core-Shell Nanowire Field Effect Tran- sistor	58
4.2.1	Computational Methods	60
4.2.2	Results and Discussions	66
4.2.2.1	Current-Voltage Characteristics	66
4.2.2.2	Transconductance	68
4.2.2.3	Transmission	69

4.2.2.4	Orbital Level Explanation	72
4.2.2.5	Length-dependent Transport	74
4.2.2.6	Conclusions	76
4.3	Imaging the Quantum Path of Electron in Real Space Inside a Ge-Si Core-Shell Nanowire Transistor	77
4.3.1	Quantum Modeling	78
4.3.2	Results and Discussion	88
4.3.2.1	Current-Voltage Characteristics	88
4.3.2.2	Transconductance and Transmission	91
4.3.2.3	Role of Frontier Orbitals and Interfacial Coupling	94
4.3.2.4	Conclusions	97
5	Tunnel Magnetoresistance in a Three Terminal Carbon Nanotube Junction	99
5.1	Introduction	99
5.2	Computational Methods	102
5.3	Results & Discussions	105
5.3.1	Magnetoresistance in CNT-based Tunnel Junction	105
5.3.2	Current-Voltage Characteristics in (8,0) SWCNT-Ni MTJ	107
5.3.3	Spin-resolved Current-Voltage Characteristics	108
5.3.4	Multichannel Transmission Function	110
5.3.5	Nonlinear Interfacial Coupling	112
5.3.6	Effects Induced by an Oxide Tunnel Barrier	113

5.4	Conclusions	115
6	Conclusions and Future Perspectives	117
6.1	Conclusions	117
6.2	Future Perspectives — A bird’s-eye view	120
	References	121
A	Copyrights	133
B	Copyrights	135

List of Figures

3.1	A prototypical three-terminal nanoscale junction with a nanotube spacer. The connection between the channel and the semi-infinite external electrodes is made via left and right leads of the <i>active scattering region</i> ; ϵ_g represents the gate field applied perpendicular to the channel.	38
3.2	Schematic representation of a typical nanoscale junction	40
4.1	Optimized structures of the H-passivated Si and Si-Ge core-shell nanowires along the $\langle 110 \rangle$ direction. A cross-sectional view of (a) Si nanowire and (b) Si-Ge core-shell nanowire; extended view of (c) Si nanowire and (d) Si-Ge core-shell nanowire. (Reprinted with permission from K. B. Dhungana, M. Jaishi, and R. Pati, <i>Nano Letters</i> 2016, 16, 3995–4000. Copyright (2016) American Chemical Society.)	60

4.2	Gate bias dependent current-voltage characteristics. (a, b) Si nanowire quantum dot FETs of channel lengths 13.65 and 17.55 Å, respectively. (c, d) Si-Ge core-shell nanowire quantum dot FETs of channel lengths 14.30 and 18.40 Å, respectively. (Reprinted with permission from K. B. Dhungana, M. Jaishi, and R. Pati, <i>Nano Letters</i> 2016, 16, 3995–4000. Copyright (2016) American Chemical Society.)	67
4.3	Source-drain current (I_{sd}) and transconductance as a function of gate bias (V_g) for the Si and Si-Ge core-shell nanowire quantum dot FETs at a fixed source-drain bias of ~ 0.2 V. (a, c) Channel lengths for the Si and Si-Ge nanowire devices are 13.65 and 14.30 Å, respectively. (b, d) Channel lengths for the Si and Si-Ge nanowire devices are 17.55 and 18.40 Å, respectively. (Reprinted with permission from K. B. Dhungana, M. Jaishi, and R. Pati, <i>Nano Letters</i> 2016, 16, 3995–4000. Copyright (2016) American Chemical Society.)	68
4.4	Transmission as a function of injection energy for different gate bias at equilibrium ($V_{sd} = 0.0$ V). (a, b) Data for a Si nanowire FET of channel length 17.55 Å. (c, d) Data for a Si-Ge core-shell nanowire FET of channel length 18.40 Å. (Reprinted with permission from K. B. Dhungana, M. Jaishi, and R. Pati, <i>Nano Letters</i> 2016, 16, 3995–4000. Copyright (2016) American Chemical Society.)	70

4.5 Transmission as a function of injection energy for different source-drain bias ($V_g=9.5$ V; channel length is 14.30 Å) in the Si-Ge core-shell nanowire FET. (a) Transmission in the energy window of $[-0.5$ eV, 0.5 eV]. (b) Zoomed-in version of the transmission in the energy window of $[-0.15$ eV, 0.15 eV]; the dotted lines represent the chemical potential window for the respective applied bias. (Reprinted with permission from K. B. Dhungana, M. Jaishi, and R. Pati, *Nano Letters* 2016, 16, 3995–4000. Copyright (2016) American Chemical Society.) 72

4.6 A schematic to elucidate the electronic orbital control mechanism for the superior performance of a (b) Si-Ge core-shell nanowire quantum dot FET over (a) the Si nanowire quantum dot FET. For the ON state, carrier transport is restricted to the shell layer. The p_z orbitals provide the pathway for tunneling of electrons. (Reprinted with permission from K. B. Dhungana, M. Jaishi, and R. Pati, *Nano Letters* 2016, 16, 3995–4000. Copyright (2016) American Chemical Society.) 73

4.7 Variation of current with the source-drain bias for different channel lengths (L) of (a) Si nanowire junction and (b) Si-Ge core-shell nanowire junction, in the absence of gate bias. The I_{sd} is fitted to a straight line to calculate the conductance (G_C) for different wire lengths (L). The inset shows the $\ln(G_C)$ vs. L plot, which is fitted to a straight line to calculate the electron tunneling decay constant (β) of 0.37 and 0.24 \AA^{-1} for Si and Si-Ge core-shell nanowire junction respectively. (Reprinted with permission from K. B. Dhungana, M. Jaishi, and R. Pati, *Nano Letters* 2016, 16, 3995–4000. Copyright (2016) American Chemical Society.) 75

4.8 Atomic model of the Ge-Si core-shell nanowire. A perspective view of the optimized nanowire structure along the $\langle 110 \rangle$ direction. (a) Core (Ge) diameter is 11.7 \AA . (b) Core (Ge) diameter is 4.7 \AA . (Reprinted with permission from M. Jaishi, and R. Pati, *Nanoscale* 2017, 9, 13425–13431. Copyright (2017) Royal Society of Chemistry.) 78

<p>4.9 Electronic band structure, band-decomposed charge density, and device configuration. Atom decomposed electronic band structure of surface passivated Ge-Si core-shell nanowires. (a) Ge core-diameter 11.7 Å. (b) Ge core-diameter 4.7 Å. Size of the circle determines the weightage of the atom. (c) & (d) Represent charge density plot (2D) at valence band maximum (VBM) and conduction band minimum (CBM) respectively for core diameter 11.7 Å. (e) & (f) Represent charge density plot at VBM and CBM respectively (core diameter 4.7 Å). (g) Schematic representation of a core-shell nanowire field effect transistor. (Reprinted with permission from M. Jaishi, and R. Pati, <i>Nanoscale</i> 2017, 9, 13425–13431. Copyright (2017) Royal Society of Chemistry.)</p>	85
<p>4.10 Current (I)-Voltage (V) characteristics of the transistor. (a, b) Ge-Si core-shell nanowire quantum dot FET with a core diameter of 11.7 Å. (c, d) Ge-Si core-shell nanowire quantum dot FET with a core diameter of 4.7 Å. (Reprinted with permission from M. Jaishi, and R. Pati, <i>Nanoscale</i> 2017, 9, 13425–13431. Copyright (2017) Royal Society of Chemistry.)</p>	89
<p>4.11 Drain current vs. Gate voltage plot at a fixed source-drain bias in a Ge-Si core-shell nanowire FETs; (a) Ge-core diameter 11.7 Å, and (b) Ge-core diameter 4.7 Å. (Reprinted with permission from M. Jaishi, and R. Pati, <i>Nanoscale</i> 2017, 9, 13425–13431. Copyright (2017) Royal Society of Chemistry.)</p>	90

4.12 Transconductance and transmission function in two representative nanowire junctions. Gate bias dependent transmission is plotted at a fixed source-drain bias of $V_{ds} \sim 0.27$ V; dotted lines represent the chemical potential window. (a, b) Ge-Si core-shell nanowire quantum dot FET with a core diameter of 11.7 Å. (c, d) Ge-Si core-shell nanowire quantum dot FET with a core diameter of 4.7 Å. Lower panels in the transmission plots represent the ON states and upper panels represent the OFF states. (Reprinted with permission from M. Jaishi, and R. Pati, *Nanoscale* 2017, 9, 13425–13431. Copyright (2017) Royal Society of Chemistry.) 92

4.13 Gate bias dependent transmission at a fixed source-drain bias of V_{ds} (0.27 V) in Ge- Si core-shell nanowire FETs. (a) Ge-core diameter is 11.7 Å, (b) Ge-core diameter is 4.7 Å; dotted lines represent the chemical potential window. (Reprinted with permission from M. Jaishi, and R. Pati, *Nanoscale* 2017, 9, 13425–13431. Copyright (2017) Royal Society of Chemistry.) . 94

4.14 Decoupling of carrier transport. Schematic illustration of the gate biased induced decoupling of electron transport between the core and shell region of the Ge-Si core-shell nanowire channel in the x-z plane; z-axis is the current carrying axis; gate field is applied along the x-axis; alternative atoms are in different planes. (a) Peak state of the current (ON state): p_z orbital of the Ge atom at the core-shell interface provides the most probable tunneling pathway for carrier transport. (b) One of the intermediate states between the ON and OFF states shows the decreased participation of Ge with the increase of gate bias. (c) Valley state of the current (OFF state): p_z orbital at the shell Si atom provides the current path; core Ge atoms do not participate in tunneling. (Reprinted with permission from M. Jaishi, and R. Pati, *Nanoscale* 2017, 9, 13425–13431. Copyright (2017) Royal Society of Chemistry.) 95

4.15 Sketch of the proposed experiment. Plausible four probe junctions for studying gate bias induced decoupling of carrier transport in co-axially gated Ge-Si core-shell nanowire junction. I_{d1} refers to the drain current from the Ge core and I_{d2} refers to the drain current from the Si shell of the nanowire. (Reprinted with permission from M. Jaishi, and R. Pati, *Nanoscale* 2017, 9, 13425–13431. Copyright (2017) Royal Society of Chemistry.) 96

5.1	Band Structure plot of (8,0) SWCNT showing a fundamental gap of 0.58 eV at Γ point; the presence of a definite band gap ascertains the semiconductor behavior of (8,0) SWCNT.	104
5.2	A three terminal (8,0) single-wall carbon nanotube-Ni magnetic tunnel junction; ϵ_g represents the gate field applied perpendicular to the channel axis. PC and APC refer to the parallel and antiparallel spin configuration of ferromagnetic source and drain electrodes.	105
5.3	TMR in an MTJ built out of semiconductor (8,0) SWCNT. TMR is plotted as a function of gate bias for the fixed source-drain bias of (a) \sim 0.80 V and (b) \sim 1.55 V.	106
5.4	Current-voltage characteristics in an (8,0) SWCNT-Ni MTJ. Drain current (I_{DS}) is plotted as a function of gate bias (V_g) for the fixed source-drain bias of (a) \sim 0.80 V and (b) \sim 1.55 V; PC and APC refer to parallel and antiparallel spin alignments between the Ni electrodes.	109
5.5	Spin-resolved current-voltage characteristics in an (8,0) SWCNT-Ni MTJ. Drain current (I_{DS}) contributions from the majority and minority spin carriers is plotted as a function of gate bias (V_g) for the fixed source-drain bias of (a) \sim 0.80 V and (b) \sim 1.55 V; Up and Down represent the respective drain current contributions from spin-up and spin-down electrons.	110

5.6	Spin-dependent transmission in a semiconductor SWCNT contacted with Ni electrodes. Transmission function is plotted at different gate bias for the fixed source-drain bias of ~ 0.80 V; (a) and (b) represent the majority (Up) and minority (Down) states' contribution to transmission in PC and APC, respectively.	111
5.7	Schematic highlighting the distinct nature of the spin-dependent hybridization between the Ni and C atoms at the interface of the (8,0) SWCNT-Ni MTJ at different gate bias points. The width of the line indicates the strength of the coupling; V_{G1} , V_{G2} and V_{G3} refer to three different gate voltages.	112
5.8	Tuning the spin-transport characteristics by inserting an Aluminum oxide (Al_2O_3) tunnel barrier at the (8,0) SWCNT-Ni contacts. (a) & (b) represent the respective TMR and I_{DS} vs. V_g plots at the $V_{DS} = 1.50$ V; PC and APC represent the parallel and parallel spin alignment of Ni electrodes. . . .	114

List of Tables

4.1	The optimized coordinates of the atoms in a $\langle 110 \rangle$ Si nanowire unit cell. (Reprinted with permission from K. B. Dhungana, M. Jaishi, and R. Pati, <i>Nano Letters</i> 2016, 16, 3995–4000. Copyright (2016) American Chemical Society.)	62
4.2	The optimized coordinates of the atoms in a $\langle 110 \rangle$ Si-Ge core-shell nanowire unit cell. (Reprinted with permission from K. B. Dhungana, M. Jaishi, and R. Pati, <i>Nano Letters</i> 2016, 16, 3995–4000. Copyright (2016) American Chemical Society.)	63
4.3	Dipole moment and polarizability. Components of dipole moment (α) and polarizability (β) for the Si and Si-Ge core-shell nanowire junctions. The channel lengths for Si and Si-Ge core-shell nanowires are 17.55 Å and 18.40 Å, respectively. (Reprinted with permission from K. B. Dhungana, M. Jaishi, and R. Pati, <i>Nano Letters</i> 2016, 16, 3995–4000. Copyright (2016) American Chemical Society.)	74

4.4	Optimized atomic coordinates in the unit cell of Ge-Si core-shell nanowire grown along $\langle 110 \rangle$; Ge-core diameter is 4.7 Å; lattice parameter is 3.91 Å. (Reprinted with permission from M. Jaishi, and R. Pati, <i>Nanoscale</i> 2017, 9, 13425–13431. Copyright (2017) Royal Society of Chemistry.)	80
4.5	Optimized atomic coordinates in the unit cell of Ge-Si core-shell nanowire grown along $\langle 110 \rangle$; Ge-core diameter is 11.7 Å; lattice parameter is 3.96 Å. (Reprinted with permission from M. Jaishi, and R. Pati, <i>Nanoscale</i> 2017, 9, 13425–13431. Copyright (2017) Royal Society of Chemistry.)	82
5.1	The optimized coordinates of the atoms in an (8,0) SWCNT unit cell. . .	103
5.2	Dipole moment and polarizability. Components of dipole moment (α) and polarizability (β) in a CNT-Ni MTJ.	113

Acknowledgments

First and foremost, I would like to express my sincere gratitude to my advisor Prof. Ranjit Pati. His mentoring has always been the source of inspiration which motivated me to perform well and finish my thesis in a timely manner. I appreciate all his time and effort that he has put on me during my Ph.D. to make this journey very productive and thought-provoking. I thank him for the moral support he provided during the tough times in the initial days of my Ph.D. I would always be grateful to him for all the tireless and stimulating discussions that we had together during my Ph.D. The passion and enthusiasm that he has for his research and for the science is truly inspirational.

My sincere thanks go to Prof. Ravindra Pandey, chair of the physics department, for his invaluable suggestions and unconditional support during my Ph.D. I thank him for his encouragement and regular guidance at several critical point of times during my Ph.D. I am thankful to him for providing me the opportunity to attend the CRYSTAL workshop at the University of Minnesota-Minneapolis during the summer of 2017.

I thank Prof. Maximilian J. Seel for all his fruitful suggestions during my Ph.D. I owe my gratitude to him for writing letters on my behalf to various global institutions.

I would like to thank my advisory committee members, Prof. Ranjit Pati, Prof. Ravindra Pandey, Prof. Maximilian J. Seel and Prof. Gregory M. Odegard for critically revising my

thesis and providing me with insightful comments.

My sincere thanks go to the Henes Center for Quantum Phenomena and its head Prof. Jacek Borysow for the financial support that the center provided for my trip to APS and MRS conferences. I am highly grateful to Prof. Borysow for awarding me the Henes center fellowship at a very critical point of time in my Ph.D. I thank him for his enthusiasm and ardent support for the science.

I am thankful to my senior colleague Dr. Kamal Dhungana, for helping me learn various computational techniques and providing me with insightful suggestions during the starting days of my Ph.D.

My sincere thanks are due to Dr. William Slough, lab coordinator of the physics department, for his timely suggestions, supervision, encouragement, and support. I appreciate his considerate gesture on many occasions during the tough times of my Ph.D. pursuit.

I am thankful to all the faculties and staff members of physics department for their support and encouragement during my Ph.D.

I am grateful to the IT Department at MTU for providing me with computing resources during the entire length of my Ph.D. My sincere thanks are due to Dr. Gowtham, Director of research computing, for helping me with issues related to high-performance computing cluster and for providing me with L^AT_EX template for compiling this dissertation.

I am thankful to all my friends who have helped and supported me during the different phases of my stay at the Michigan Technological University. Special thanks go to all my office mates of Rekhi 322 for bearing with me and supporting me with everything I needed during my Ph.D. I have received enormous love and support from all my friends and their family members at Houghton. Thank you all for making this journey of my life joyful and memorable.

I would also like to take this opportunity to thank my special friend Mr. Lal Prasad Dangal (LPD) for his help and moral support during my pre-MTU days.

I owe my deepest gratitude to my parents for their endless support and encouragement for whatever I have intended in my life so far. I would always be indebted to them for all the sacrifices they had done for me. I also would like to thank my brothers and my in-laws for their continued guidance and support during the different stages of my life.

It would have been impossible for me to finish this thesis without the selfless support and encouragement from my wife Gyanu. During this toughest part of my life, she has always been there supporting me in all my pursuits. My heartfelt thanks go to you my dear for all your sacrifices that made it possible for me. Finally, I would like to thank my little daughter Aadhya for bringing a lot of joy and happiness in our life. Your blissful presence has made it much easier for me to cover this journey of my life.

Abstract

One-dimensional (1D) nanoscale systems — structures with the lateral dimensions ranging from 1 nm to 100 nm — have received significant research interest due to their unique structure-guided properties that promise functionalities far more superior than their bulk counterparts. The quantum confinement effect in 1D nanostructures provides us with a very powerful tool to tune their electrical, magnetic, optical and thermal properties and opens the gateway for their multifunctional usages in next-generation electronics. In particular, carbon nanotubes and semiconductor nanowires are found to offer tremendous opportunities to form the junction devices with controlled electronic and optoelectronic properties crucial to predictable device functions. Along with the experimental progress in synthesis and fabrication techniques leading to nano-dimensional devices with diverse applications, theoretical insights at the level of electronic structure is equally important to tune various material properties for achieving greater device performance coupled with a wider range of functionalities. This thesis provides a theoretical description of the quantum transport properties in semiconductor core-shell nanowire field effect transistors (FETs) and (8,0) single-wall carbon nanotube contacted to ferromagnetic electrodes using the *first principles* density functional theory (DFT) in conjunction with the coherent single-particle many-body Green's functions approach. The first project of the thesis outlines the *superior* performance of a semiconductor Si-Ge core-shell nanowire quantum dot FET over its pristine Si nanowire counterpart. In this work, we have unlocked the switching mechanism

responsible for the superior performance of the Si-Ge nanowire FET with the p_z -orbitals in the (outer)shell-layer providing the carrier pathway in both nanowire FETs. This is followed by a work on charge transport in semiconductor Ge-Si core-shell nanowire quantum dot FETs of two different Ge-core diameters. Here, we have identified the most probable tunneling pathway of electrons in Ge-Si FETs with an orbital spatial level resolution which demonstrates the gate-bias-driven *decoupling* of carrier transport between the core and shell-region. Our calculations hold a qualitative agreement with the experimentally reported results. Irrespective of the Ge core diameter, we observed excellent FET characteristics within a certain threshold gate bias after which the drain current is found to drop rapidly leading to the negative differential resistance (NDR). An orbital level analysis reveals a strong coupling between the p_z -orbitals of the core-Ge and the s -orbitals of the gold electrode giving rise to the peak state of NDR; no such coupling is found at the valley NDR state for which the contribution comes solely from the p_z -orbitals of the shell-Si. The final project of this thesis comprises the result of our work on spin transport in an (8,0) single-wall carbon nanotube - nickel magnetic tunnel junction. We found an oscillatory tunnel magnetoresistance showing a wide variation in its amplitude and width with the gate bias coupled with TMR sign reversals as observed in the experiment. Analysis of our calculation revealed a *nonlinear* coupling at the interface with s - and d -orbitals of different Ni atoms hybridized with p_z orbitals of different interfacial carbon atoms at each gate bias points. Inserting an oxide layer at the interface is found to tune the oscillation in TMR in a predictable manner resulting in a much smoother oscillation critical to its application.

Chapter 1

Introduction

With the unparalleled advancements made over the last two decades, developments in modern-day electronics have left every other sector far behind. The relentless quest of creating more advanced electronic devices have revolutionized the world of electronics with the modern-day devices becoming thinner, smarter and ever more powerful and yet, cheaper. The enormous growth of the semiconductor industry since the 1960s is powered by the exponential increase in the number of the transistors packed inside the microprocessor chip of a device[1, 2]. Moore's law[3, 4], in this regard, has been the guiding principle in shaping the semiconductor industry from the last five decades[5]. Unlike any other law in physics, it is rather a prediction made by Gordon Moore, in 1965, that the number of transistors in a microprocessor chip will double each year and so will be the performance of the device[2, 3]. Later in 1975, Moore revised his prediction for the transistor doubling time

and made a more realistic estimate of two years[4]. Justifying Richard Feynmann's famous lecture "*There's plenty of room at the bottom*", the law is followed with an uncanny accuracy until the first decade of the 21st century. The exponential growth that Moore predicted transformed the world of electronics with the bulky home computers of the 1970s turning into the more advanced machines of 1980s and from there to the high-speed internet, mobile and wearable electronics, and automated self-driving cars[1]. The simple guiding principle of scaling down the feature size for a faster chip performance with lesser power consumption followed, quite well, until the early 2000s[1, 2]. But as the transistor size began to shrink below 90 nm, too much heat produced due to a faster movement of electrons through the miniaturized silicon circuitry, became a matter of serious concern[1, 2]. To get rid of this problem, manufacturers slowed down the clock rates and put a limit on electrons speed inside the chip[1, 2]. To maintain Moore's law performance curve, the idea of multiple processors in a single chip, then, came into practice by building machines with up to 16 cores. Though shrinking the transistor size to be in line with Moore's law is made possible by using above measures, scaling further down will soon be halted as quantum effects come into play when the feature size will reach atomic dimension. The effect has already been felt with the state-of-the-art devices being stuck at the 14 nm node from the last couple of years. Further scaling will soon bring the feature size to few atoms across, at which, the behavior the electron will be governed by the probabilistic nature of quantum mechanics; the electrons will leak across the miniaturized silicon circuitry resulting in an unreliable transistor performance[1, 2].

To clear the impasse looming over the future of Moore's law, researchers all over the world are in pursuit of a viable alternative that can bring greater device functionality with lesser consumption of energy than the existing silicon-based CMOS technology. Efforts in this direction have led to the design and discovery of several nano-dimensional (0, 1- and 2-dimensional) semiconductor materials. Among various candidate materials, one-dimensional semiconductor core-shell nanowires [6–29] have shown an enormous promise in recent years. Core-shell nanowires are one-dimensional radial heterostructures having a different atomic composition in the core and the shell region[6, 8, 13]. The pioneering effort in this direction was made from Charles Lieber's group with the synthesis of semiconductor Si/Ge and Ge/Si core-shell and core-multishell nanowires using the chemical vapor deposition method[6]. They reported that the lattice mismatch at the core-shell interface in these nanowires results in band-offsets between the core and shell region; this provides an unique opportunity to drive the carrier transport either through the core or the shell region, thus, making it an excellent candidate material for the next-generation electronics[6]. A high-performance behavior of Ge/Si core-shell nanowire field-effect-transistor (FET) have also been reported experimentally[8]; it is found to exhibit a ballistic transport with the mean free path of ~ 500 nm at a low bias. Furthermore, the scaled transconductance and on-current values in Ge/Si FET is reported to be more than 3 to 4 times higher than that of state-of-the-art metal-oxide-semiconductor field effect transistors (MOSFETs)[8]. These nanowires can also be produced in high yield with reproducible electronic properties which is imperative to build the large-scale integrated systems[8]. The opportunity of

coaxial gating in these nanowire FETs enables an excellent control over the off-state leakage current which helps to increase the device performance[6, 22]. Moreover, the Ge/Si core-shell nanowires are also used to build the Josephson junctions[9]. For a Si/Ge core-shell nanowire FET, studies have reported a significant enhancement in carrier mobility in comparison to its pristine counterparts[30]. Because of their compatibility with the current Si technology, the Si/Ge, and Ge/Si core-shell nanowires are seen as one of the most promising alternatives to existing Si technology.

Besides, using electron spin instead of charge to transfer, process and store information has also been perceived as a viable option; doing this would help to unite the memory and processor into a single chip and would no longer require the electron to shuttle between memory and CPU at every time we retrieve some information. This, if possible, would result in a substantial reduction of heat generated during the faster transport of charge through various chip components. But to build such a spintronic device requires a material with a long spin-flip scattering time to ascertain the coherent transport of spin through the channel[31]. Carbon nanotube (CNT), owing to its low atomic number, is found to experience a negligible spin-orbit coupling. Also, the abundant isotope of carbon, carbon-12, is not affected by the hyperfine interaction due to the absence of any unpaired electron. Because of these ideal features, semiconductor CNTs are considered an ideal candidate to be used as the spin tunneling channel in magnetic tunnel junctions[31]. The long spin-flip scattering length of 130 nm has already been reported in a ferromagnetically contacted CNT tunnel junction[31]. Experiment showing the phase coherence length of

250 nm and the elastic scattering length of 60 nm have also been observed[32]. The longer spin lifetime found in CNTs has projected them as a strong candidate material to build devices with higher tunnel magnetoresistance(TMR). TMR which underpins the modern high-density data storage device is the relative difference in resistance between the parallel and antiparallel spin alignments of the ferromagnetic contacts spacing a tunneling channel in between them. Several experimental groups have, so far, measured the TMR in two and three terminal junctions; however, the difficulties in fabricating the reproducible ferromagnetic contacts have resulted in a variation in the TMR values reported by them[31, 33–40]. Of particular interest is an experimental result published by Sahoo et al. in 2005, where they have reported an oscillatory variation of TMR with gate bias in CNT junctions contacted with ferromagnetic PdNi electrodes[37]. They have shown an *aperiodic* oscillatory behavior in both single and multiwall CNT junctions with sizable variation in amplitude coupled with TMR sign reversals[37]. Though they have suggested quantum interference as a possible reason, no electronic structure level description have so far been given to address the observed oscillatory TMR feature. An attempt in this direction requires an electronic structure level understanding of the gate bias effect on the contacts as well as on the CNT channel structure.

This thesis aims to understand at the electronic structure level, the charge and spin transport properties in various one-dimensional semiconductor tunnel junctions discussed above. We used density functional theory (DFT)[41] in conjunction with the coherent single particle many-body Green's functions approach (NEGF)[42] to study the quantum transport in

nanoscale junctions. In chapter two, the theoretical background for solving the many-body Schrödinger wave equation is discussed starting from the single particle Slater determinant to all the way up to density functional theory utilizing the hybrid exchange-correlation functional. Chapter three describes our quantum transport approach which includes a detail discussion regarding the construction of Green's function in the nonequilibrium condition of spin-restricted and spin-polarized nanoscale tunnel junctions; the Landauer-Büttiker formalism to obtain the drain current by integrating the transmission function within the calculated chemical potential window is discussed further. In chapter four, the results of the work done on one-dimensional semiconductor Si/Ge and Ge/Si core-shell nanowire field effect transistors are described. The first part of this chapter discusses the observed superior performance of the Si/Ge core-shell nanowire quantum dot field effect transistor in comparison to its pristine silicon counterpart[43]. Similarly, the second part describes the mechanism behind the gate driven negative differential resistance (NDR) behavior observed in the Ge/Si core-shell nanowire quantum dot FETs[44]. The fifth chapter of the thesis discusses, in detail, the results of the work done to elucidate the mechanism behind the experimentally reported oscillatory TMR feature in ferromagnetically contacted carbon nanotube junction. Finally, the thesis is concluded by proposing some future work as an extension of the work done during my Ph.D.

Chapter 2

Density Functional Theory

2.1 Introduction

The solution of the quantum many-body problem is central to understand the various physical, chemical and biological processes in nature. However, due to computational complexities arising from the requirement of having an infinite basis set, the exact solution of a many-body Schrödinger wave equation (SWE) is not possible. Thus, to obtain a reasonably accurate description of the quantum many-body problem, various approximation methods have been developed and the Hartree-Fock method of solving the Schrödinger wave equation is the foremost of this kind [45–47]. It is a wavefunction based approach

that gives very accurate results for smaller system, however, with the increase in the number of electrons, the computational cost goes dramatically high making it almost impossible to use this method for systems having a large number of electrons. To overcome this problem, a density-based approach is introduced by considering electron density $n(r)$ instead of the wavefunction as the fundamental quantity to calculate all the physical observables in nature [48–55]. This method of solving the quantum many-body problem is known as density functional theory (DFT) [41]. With the availability of sufficiently accurate exchange-correlation functional, it is one of the most widely used computational tools in the modern era of computational sciences [56, 57]. In this section, the basic formalism of these approximation methods for solving the quantum many-body problem will be discussed.

2.2 Many-Body Schrödinger Wave Equation

The time-independent SWE for a many electron system is an energy eigen-value equation which can be expressed as [45–47]:

$$\hat{H}\Psi(r_1, r_2, \dots, r_N) = E\Psi(r_1, r_2, \dots, r_N) \quad (2.1)$$

where \hat{H} is the Hamiltonian operator, E is the total energy and $\Psi(r_1, r_2, \dots, r_N)$ represents

the wavefunction of the N-electron system. The Hamiltonian operator of a system with N-electron and M nuclei is expressed as [45–47]:

$$\hat{H} = -\sum_{i=1}^N \frac{1}{2} \nabla_i^2 - \sum_{\alpha=1}^M \frac{1}{2M_\alpha} \nabla_\alpha^2 - \sum_{i=1}^N \sum_{\alpha=1}^M \frac{Z_\alpha}{r_{i\alpha}} + \sum_{i=1}^N \sum_{j>i}^N \frac{1}{r_{ij}} + \sum_{\alpha=1}^M \sum_{\beta>\alpha}^M \frac{Z_\alpha Z_\beta}{R_{\alpha\beta}} \quad (2.2)$$

where M_α is the ratio of the mass of nucleus α to the mass of an electron; Z_α is the atomic number of nucleus α ; r_{ij} is the distance between electron i and j ; $R_{\alpha\beta}$ is the distance between nucleus α and nucleus β . The first and second terms in Eq. (2.2) are the respective kinetic energy operators of electrons and nuclei; the third term gives the Coulomb attraction between electrons and nuclei; the fourth and the final terms are the respective representations of the repulsion between electrons and between nuclei.

2.2.1 Born-Oppenheimer Approximation

Being much heavier than the electrons, the motion of the nuclei is negligible compared to that of electrons. Thus, to a good approximation, the electrons can be considered to be moving in the field of fixed nuclei. This approximation in quantum chemistry is widely known as the *Born-Oppenheimer approximation* [47, 58]. Following this approximation, the kinetic energy term of the nuclei in (2.2) can be neglected and the final term which gives the repulsion between nuclei can be considered a constant. Thus, *Born-Oppenheimer*

approximation reduces the Hamiltonian (2.2) to a form

$$\hat{H} = -\sum_{i=1}^N \frac{1}{2} \nabla_i^2 - \sum_{i=1}^N \sum_{A=1}^M \frac{Z_A}{r_{iA}} + \sum_{i=1}^N \sum_{j>i}^N \frac{1}{r_{ij}} \quad (2.3)$$

This is known as *electronic* Hamiltonian.

2.3 Hartree Product

Let us consider a non-interacting N-electron system. The Hamiltonian for such a system consisting of non-interacting electrons can be written as

$$\hat{H} = \sum_{i=1}^N \hat{h}(i) \quad (2.4)$$

where $\hat{h}(i)$ is the operator representation for the kinetic and potential energy of the i^{th} electron. This represents the full electronic Hamiltonian if we neglect the electron-electron repulsion. $\hat{h}(i)$, on the other hand, might be thought of as an effective one-electron Hamiltonian which includes the averaged electron-electron repulsion. Therefore, the operator $\hat{h}(i)$ will have a set of individual electron wavefunction $\{\phi(i)\}$ obeying the eigenvalue equation:

$$\hat{h}(i)\phi(i) = \epsilon_i\phi(i) \quad (2.5)$$

As we can see that the total Hamiltonian \hat{H} , is a sum of one electron Hamiltonian, it's eigenfunction will, thus, be the wavefunction obtained from the simple product of individual electron wavefunction

$$\Psi(r_1, r_2, \dots, r_N) = \phi_1(r_1) \phi_2(r_2) \dots \phi_N(r_N) \quad (2.6)$$

with eigenvalue E given as

$$E = \epsilon_1 + \epsilon_2 + \dots + \epsilon_N \quad (2.7)$$

This many-electron wavefunction Eq.(2.6) is defined as *Hartree product*[45, 47]. It is an uncorrelated electron wavefunction because

$$|\Psi(r_1, r_2, \dots, r_N)|^2 dr_1 dr_2 \dots dr_N = |\phi_1(r_1)|^2 dr_1 |\phi_2(r_2)|^2 dr_2 \dots |\phi_N(r_N)|^2 dr_N \quad (2.8)$$

which means that the simultaneous probability of finding the electrons in their respective volume elements is equal to the product of the probabilities of finding the individual electrons in their volume element. Thus, it does not consider the indistinguishability of electrons into account and hence, violates the antisymmetry principle[47].

2.4 Slater Determinants

As it has been already mentioned that the Hartree product violates the antisymmetry principle which requires that the electronic wavefunction be antisymmetric with respect to the interchange of the coordinates of any two electrons. To resolve this issue of antisymmetry violation, the many-electron wavefunction is represented as a single determinant[47, 59]:

$$\Psi(r_1, r_2, \dots, r_N) = (N!)^{-\frac{1}{2}} \begin{vmatrix} \phi_1(r_1) & \phi_2(r_1) & \dots & \phi_N(r_1) \\ \phi_1(r_2) & \phi_2(r_2) & \dots & \phi_N(r_2) \\ \cdot & \cdot & \dots & \cdot \\ \cdot & \cdot & \dots & \cdot \\ \phi_1(r_N) & \phi_2(r_N) & \dots & \phi_N(r_N) \end{vmatrix} \quad (2.9)$$

which is known as *Slater determinant*[47, 59]. In above equation, the factor $(N!)^{-\frac{1}{2}}$ is the normalizing constant. This determinant has N electrons occupying N spin orbitals; rows of this N-electron Slater determinant are labeled by the position of electrons whereas the columns are labeled by the spin orbitals. So, the interchange of any two rows in this Slater determinant would represent the interchange of the coordinates of any two electrons. As per the rule of the determinant, this interchange would change the sign of the determinant and hence, the antisymmetry is properly conserved. Next, the condition of two electrons occupying the same spin orbital just like having two columns of the Slater determinant

equal, thus making the determinant zero. Therefore, no more than one electron can occupy the same spin orbital. This is the *Pauli exclusion principle*[45, 47]. Slater determinant description of the wavefunction leads to the concept of exchange-correlation which implies that the motion of electrons with parallel spins is correlated whereas the motion of opposite spin is not.

2.5 The Hartree-Fock Approximation

The Hartree-Fock method is the most widely used traditional approximation method to solve the many-electron Schrödinger wave equation. The derivation of Hartree-Fock equation (integrodifferential equation) utilizes the concept of variational principle[47, 60] which states that for the ground state wavefunction, the expectation value of the Hamiltonian is an upper bound to the exact ground state energy. Within the framework of this Hartree-Fock approximation, each electron in an N-electron system is assumed to move in the average potential produced by all electrons including itself plus the potential due to the fixed nuclei[45, 47]. The wavefunction for the N-electron quantum mechanical system is represented by a single Slater determinant with individual electron wavefunction of the form [45, 47, 59]:

$$\Psi_{HF} = \frac{1}{(N!)^{\frac{1}{2}}} \det[\phi_1 \phi_2 \dots \phi_N] \quad (2.10)$$

The expectation value of the N-electron Hamiltonian for the ground state wavefunction (Slater determinant) gives the Hartree-Fock energy of the form [45, 47]:

$$E_{HF} = \langle \Psi_{HF} | \hat{H} | \Psi_{HF} \rangle = \sum_{i=1}^N H_i + \frac{1}{2} \sum_{i,j=1}^N (J_{ij} - K_{ij}) \quad (2.11)$$

where,

$$H_i = \int \phi_i^*(x) \left[-\frac{1}{2} \nabla_i^2 + \sum_{a=1}^M \frac{Z_a}{r_{ia}} \right] \phi_i(x) dx = \int \phi_i^*(x) h(i) \phi_i(x) dx \quad (2.12)$$

$$J_{ij} = \int \int \phi_i^*(x_1) \phi_j^*(x_2) \frac{1}{r_{12}} \phi_i(x_1) \phi_j(x_2) dx_1 dx_2 \quad (2.13)$$

$$K_{ij} = \int \int \phi_i^*(x_1) \phi_j^*(x_2) \frac{1}{r_{12}} \phi_i(x_2) \phi_j(x_1) dx_1 dx_2 \quad (2.14)$$

The respective integrals J_{ij} and K_{ij} are known as Coulomb and exchange integrals. These are real integrals which satisfy the relation $J_{ij} \geq K_{ij} \geq 0$ [45, 47]. The Hartree-Fock energy E_{HF} in Eq.(2.11) is the function of spin orbitals ϕ_i . Thus, an infinitesimal variation $\delta\phi_i$ in spin orbital leads to the energy variation [45, 47]:

$$\delta E = \sum_i \delta H_i + \frac{1}{2} \sum_{i,j} (\delta J_{ij} - \delta K_{ij}) \quad (2.15)$$

Now to obtain the Hartree-Fock equations, we need to minimize the energy E_{HF} with

respect to the spin orbitals ϕ_i subject to the constraint that the spin orbitals are orthonormal [45, 47]:

$$\int \phi_i^*(x_1)\phi_j(x_1)dx_1 = \delta_{ij}$$

$$\Rightarrow \langle \phi_i | \phi_j \rangle = \delta_{ij} \quad (2.16)$$

For energy minimization, we will use the method of Lagrange's multiplier[45, 47] and define a function \mathcal{L} of spin orbitals ϕ_i such that

$$\mathcal{L}[\{\phi_i\}] = E_{HF}[\{\phi_i\}] - \sum_{i,j}^N \epsilon_{ij}(\langle \phi_i | \phi_j \rangle - \delta_{ij}) \quad (2.17)$$

where ϵ_{ij} form a set of Lagrange multipliers. Since \mathcal{L} is real and $\langle \phi_i | \phi_j \rangle = \langle \phi_j | \phi_i \rangle^*$, the Lagrange multipliers must be Hermitian.

Now the minimization of energy E_{HF} is obtained by minimizing \mathcal{L} . Thus, setting the first variation in \mathcal{L} equal to zero

$$\delta \mathcal{L} = \delta E_{HF} - \sum_{i,j}^N \epsilon_{ij} \delta \langle \phi_i | \phi_j \rangle = 0 \quad (2.18)$$

leads to the result

$$f(i)\phi_i(x) = \epsilon_i\phi_i(x) \quad (2.19)$$

where

$$\begin{aligned}
 f(i) &= h(i) + \sum_{\beta} \mathcal{J}_{\beta}(i) - \mathcal{K}_{\beta}(i) \\
 &= h(i) + v^{HF}(i)
 \end{aligned}
 \tag{2.20}$$

is a one-electron operator called the Fock operator[45, 47] which is the sum of the core Hamiltonian operator $h(i)$ and an effective one-electron potential operator called the *Hartree-Fock potential* $v^{HF}(i)$. Multiplying both sides of Eq.(2.19) by ϕ_i^* from the left and integrating, we get

$$\varepsilon_i = H_i + \sum_j (J_{ij} - K_{ij})
 \tag{2.21}$$

Now if we simply add up all the orbital energies corresponding to N ground state electrons by summing over i on both sides of Eq.(2.21), we get

$$\sum_i^N \varepsilon_i = \sum_i^N H_i + \sum_{i,j}^N (J_{ij} - K_{ij})
 \tag{2.22}$$

Comparing these result with Eq.(2.11), we found that

$$E_{HF} \neq \sum_i^N \varepsilon_i
 \tag{2.23}$$

which clearly indicates that the total energy of the state Ψ_{HF} is not equal to the sum of the orbital energies. The reasoning goes as follows: Since we are summing up twice the exchange and Coulomb interaction term in Eq.(2.22), separately for the spin orbitals ϕ_i and

ϕ_j , the electron-electron interaction between the electrons in ϕ_i and ϕ_j are added twice, and thus, leads to the above discrepancy [45, 47]. Therefore, the correct Hartree-Fock ground state energy is obtained by subtracting this extra summation term as shown

$$E_{HF} = \sum_i^N \varepsilon_i - \sum_{j>i}^N (J_{ij} - K_{ij}) \quad (2.24)$$

The Hartree-Fock approximation gives a very accurate result for smaller systems but fails to do so in the case of bigger many-body systems. Though it includes the exact exchange between the electrons with parallel spin, the Hartree-Fock approximation does not take into account the correlation arising due to the many-body interactions. This results in a significant deviation from the exact non-relativistic ground state energy. To resolve this discrepancy, many post-Hartree-Fock methods have been developed such as configuration interaction (CI), many-body perturbation approach, and single particle many-body Green's function technique [41, 47]. Though all of these post-Hartree-Fock methods provide an accurate description of the many body system by including the correlation interaction into account, it comes at the expense of very high computational cost [41, 47]. To illustrate this computational complexity, let us consider a wavefunction, $\Psi(r_1, r_2, \dots, r_N)$ representing an N electron system in real space; the total number of coordinates needed to describe the wavefunction Ψ will be $3N$ [61]. If each of these coordinates is segmented using a mesh with 100 integration grids, it will require 100^{3N} values to fully describe the wavefunction Ψ [61]. But a mesh with only 100 grids is not sufficient to provide a reasonably accurate result. For that, we need multiple higher number of integration grids which will make

it almost impossible to go beyond systems with few numbers of atoms. Therefore, an alternate approach which is based on the density of electrons $n(\mathbf{r})$ rather than wavefunction is developed for solving larger many-body systems; all physical observables of a quantum many-body system in this approach is calculated using the electron density. Since electron density is a function of three spatial coordinates, it requires only 100^3 values to describe an N -electron system using a mesh with the same number of grids. Particularly, in the case of Kohn-Sham density functional theory (DFT) which has largely been employed in this thesis, a set of N single-particle orbitals are further added to form the electron density. Therefore, it requires only $N \times 100^3$ values to represent the N -electron system and makes a significant reduction in the computational cost in comparison to wavefunction based methods [61]. This makes DFT, a viable alternative to wavefunction based approach in solving the many-body quantum mechanical problem with the higher number of atoms. Further details regarding the formulation of many-body DFT is discussed in the following sections.

2.6 Thomas-Fermi Model

The concept of energy minimization with respect to local electron density to calculate the ground state energy of many electron systems was initially formulated by Thomas and Fermi in 1920 [41, 62]. Thomas-Fermi model assumes a uniform distribution of electrons inside an atom. Now to derive the kinetic energy as a function of electron density, this

model assumes that each phase space volume given by h^3 , where h is the Planck's constant, is occupied by two electrons and the electrons are moving in an effective potential field determined by the nuclear charge. The density of ΔN electrons in real space within a cube of side l is given by [41]:

$$n(r) = \frac{\Delta N}{v} = \frac{\Delta N}{l^3} \quad (2.25)$$

Within this assumption, the total kinetic energy as a functional of local electron density of an atom is written as [41]:

$$T^{TF}[n] = 2.871 \int n^{5/3}(r) dr \quad (2.26)$$

This expression is known as Thomas-Fermi kinetic energy functional [62]. Further addition of classical electrostatic energy terms corresponding to electron-nucleus attraction and electron-electron repulsion to Eq.(2.26) leads to the total energy functional expressed as [41]:

$$E_{TF}[n(r)] = 2.871 \int n^{5/3}(r)dr - Z \int \frac{n(r)}{r} dr + \frac{1}{2} \int \int \frac{n(r_1)n(r_2)}{|r_1 - r_2|} dr_1 dr_2 \quad (2.27)$$

This is the Thomas-Fermi total energy functional. Now to obtain the ground state energy, we need to minimize the energy functional (2.27) with respect to local electron density subject to the constraint that[41]

$$N = N[n(r)] = \int n(r) dr \quad (2.28)$$

Therefore, by using the Lagrange's multiplier scheme of functional variation as in section 2.5, we obtain

$$\mu_{FT} = \frac{\delta E_{FT}[n]}{\delta n(r)} = \frac{5}{3} \times 2.87n^{2/3}(r) - \frac{z}{r} + \int \frac{n(r_2)}{|r-r_2|} dr_2 \quad (2.29)$$

This is known as Thomas-Fermi equation [41]. Though this model predicts a reasonably good description of atoms, it is oversimplified and is not as accurate as other approximate methods. Utilizing this idea of using density functional for solving the many-body problem, Hohenberg and Kohn in 1964 proved two fundamental theorems known as the Hohenberg-Kohn theorem [48, 49]. Within the framework of this theorem, the Thomas-Fermi model for the ground state may be considered as an approximation to the density functional theory [41].

2.7 The Hohenberg-Kohn Theorem

Theorem 1. (First Hohenberg-Kohn Theorem) *For any system of interacting particles in an external potential $V_{ext}(r)$, the potential $V_{ext}(r)$ is uniquely determined by the ground state particle density $n(r)$.*

The proof of this theorem is through reasoning by contradiction. Let us rewrite the Hamiltonian for an N-electron system with the non-degenerate ground state wavefunction Ψ as

$$\hat{H} = -\sum_{i=1}^N \frac{1}{2} \nabla_i^2 - \sum_{i=1}^N \sum_{A=1}^M \frac{Z_A}{r_{iA}} + \sum_{i=1}^N \sum_{j>i}^N \frac{1}{r_{ij}} = \hat{T} + \hat{V}_{ext} + \hat{V}_{elec} \quad (2.30)$$

where \hat{T} is the kinetic energy, \hat{V}_{ext} is the external potential, \hat{V}_{elec} is the Coulomb repulsive potential between electrons. The electronic density for this ground state wavefunction is defined as:

$$n(r) = \langle \Psi | \Psi \rangle = \int d^3 r_2 \dots \int d^3 r_N |\Psi(r, r_2, \dots, r_N)|^2 \quad (2.31)$$

Let us suppose there exist another Hamiltonian

$$\hat{H}' = \hat{T} + \hat{V}'_{ext} + \hat{V}_{elec} \quad (2.32)$$

corresponding to different ground state wavefunction Ψ' such that the external potentials \hat{V}_{ext} and \hat{V}'_{ext} differ by more than a constant but yield the same ground state density. Then by applying the variation principle, the following relation holds true:

$$\begin{aligned} \varepsilon' &= \langle \Psi' | \hat{H}' | \Psi' \rangle \\ &< \langle \Psi | \hat{H}' | \Psi \rangle \\ &< \langle \Psi | \hat{H} + \hat{V}'_{ext} - \hat{V}_{ext} | \Psi \rangle \end{aligned} \quad (2.33)$$

which implies that

$$\varepsilon' < \varepsilon + \int (\hat{V}'_{ext} - \hat{V}_{ext})n(r)dr \quad (2.34)$$

Similarly, we can show that

$$\varepsilon < \varepsilon' + \int (\hat{V}_{ext} - \hat{V}'_{ext})n(r)dr \quad (2.35)$$

Adding above Eq.(2.34) and Eq.(2.35), we get

$$\varepsilon' + \varepsilon < \varepsilon + \varepsilon' \quad (2.36)$$

which is an obvious contradiction. Thus, it proves that the ground state electronic density uniquely determines the external potential up to an additive constant.

Theorem 2. (Second Hohenberg-Kohn Theorem) *The ground state energy E is also uniquely determined by the ground-state charge density: the density that minimizes the total energy is the exact ground state density.*

The proof of second Hohenberg-Kohn (H-K) theorem immediately follows from the first

H-K theorem. The energy as a functional of density $n(\mathbf{r})$ can be expressed as [41, 63]:

$$\begin{aligned}
 E[n(\mathbf{r})] &= \langle \Psi | \hat{T} + \hat{V}_{elec} + \hat{V}_{ext} | \Psi \rangle \\
 &= T[n(\mathbf{r})] + V_{elec}[n(\mathbf{r})] + V_{ext}[n(\mathbf{r})] \\
 &= F[n(\mathbf{r})] + \int n(\mathbf{r}) V_{ext} d\mathbf{r}
 \end{aligned} \tag{2.37}$$

As it is proved in the previous theorem that the external potential is uniquely determined by the density which as shown above determines the Hamiltonian as well as its associated ground state wavefunction. This means that the wavefunction Ψ is also a functional of density $n(\mathbf{r})$ and hence, for any arbitrary operator \hat{O} :

$$\langle \Psi | \hat{O} | \Psi \rangle = O[n(\mathbf{r})] \tag{2.38}$$

Now, as the ground state energy can be uniquely determined from the ground state density $n(\mathbf{r})$, we get

$$\begin{aligned}
 \varepsilon[n(\mathbf{r})] &= \langle \Psi | \hat{H} | \Psi \rangle \\
 &= \langle \Psi | \hat{F} + \hat{V}_{ext} | \Psi \rangle
 \end{aligned} \tag{2.39}$$

From the variational principle, we know that density $n'(r)$ other than the ground state density $n(r)$ must give a higher energy [41, 63]:

$$\varepsilon = \varepsilon[n(r)] = \langle \Psi | \hat{F} + \hat{V}_{ext} | \Psi \rangle < \langle \Psi' | \hat{F} + \hat{V}_{ext} | \Psi' \rangle = \varepsilon[n'(r)] = \varepsilon' \quad (2.40)$$

Therefore, it is proved using a variational approach that by minimizing the total energy with respect to $n(r)$, we obtain the total ground state energy. So, the correct density that minimizes the total energy is the exact ground state density.

2.8 The Kohn-Sham Approach

In 1965, Kohn and Sham (KS) formulated the density functional theory in a more convenient way that made it possible to implement this theory in practice [50, 52–54]. The main idea behind the KS theory is to map the system of interacting electrons onto a fictitious system of non-interacting electrons with both of them having the same ground state charge density[50]. According to this formulation, the ground state charge density of a system of non-interacting electrons is expressed as

$$n(r) = 2 \sum_{i=1}^{N/2} |\phi_i|^2 \quad (2.41)$$

where ϕ_i represent the one-electron Kohn-Sham orbitals. The factor two in above equation comes from two spin states of an electron. Despite this KS orbital representation, it is the ground state charge density which acts as the fundamental variable in determining all the properties of a quantum many-body system. The total energy in functional in the Kohn-Sham formulation of DFT is expressed as[50]:

$$E[n] = T_s[n] + J_H[n] + E_{xc}[n] + \int v_{ext}(r)n(r)dr \quad (2.42)$$

where the first term

$$T_s[n] = -\frac{1}{2} \sum_i^N \langle \phi_i | \nabla^2 | \phi_i \rangle \quad (2.43)$$

is the kinetic energy of the non-interacting electrons calculated in terms of KS orbitals [41, 50]. The second term

$$J_H[n] = \frac{1}{2} \int \int \frac{n(r_1)n(r_2)}{|r_1 - r_2|} dr_1 dr_2 \quad (2.44)$$

is known as the Hartree energy which, in fact, is the classical Coulomb repulsive interaction between the electrons[41, 50]. The third term $E_{xc}[n]$ is called the *exchange-correlation* energy which accounts for all the errors that crept in while mapping the real interacting system of electrons onto a fictitious non-interacting electrons [41, 50]. Within this framework of KS orbitals, the total energy functional can further be expressed as:

$$E[n] = \sum_i^N \int \phi_i^*(r) \left(-\frac{1}{2} \nabla^2 \right) \phi_i(r) dr + J_H[n] + E_{xc}[n] + \int v_{ext}(r)n(r)dr \quad (2.45)$$

Using the method of Lagrange's undetermined multiplier to minimize the total energy subject to the constraint that the KS orbitals are orthonormal

$$\int \phi_i^*(r)\phi_j(r)dr = \delta_{ij} \quad (2.46)$$

leads to following variational expression

$$\delta \left[E[n] - \sum_{ij} \epsilon_{ij} \int \phi_i^*(r)\phi_j(r)dr \right] = 0 \quad (2.47)$$

The final expression obtained upon simplifying the above equation can be written as [41, 50]:

$$\left[-\frac{1}{2}\nabla^2 + v_{eff}(r) \right] \phi_i(r) = \epsilon_i \phi_i(r) \quad (2.48)$$

This is known as the Kohn-Sham equation of DFT. Here,

$$v_{eff}(r) = \int \frac{n(r')}{|r-r'|} dr' + v_{xc}(r) + v_{ext}(r) \quad (2.49)$$

is known as the effective potential with the exchange-correlation potential $v_{xc}(r)$ expressed as [41, 50]:

$$v_{xc}(r) = \frac{\delta E_{xc}[n]}{\delta n(r)} \quad (2.50)$$

The Kohn-Sham DFT Eq.(2.48) looks similar to that of Hartree-Fock equation with the only difference being the replacement of exact exchange term with that of exchange-correlation potential $v_{xc}(r)$. The actual implementation of the Kohn-Sham DFT calculation is done

using self-consistent field (SCF) method. According to this method, the calculation is started taking a guessed value of the charge density $n(r)$ which iterates through the KS equation (2.48) until the difference between the newly obtained $n(r)$ and the last one used to construct the KS effective potential $v_{eff}(r)$ is insignificant. Once the SCF cycle is converged, the ground state energy is then computed using the finally obtained charge density. Though DFT incorporates both the exchange and correlation interaction between the particles in a many-body system, the difficulty in obtaining the explicit expression of exchange-correlation term mandates to approximate the functional $E_{xc}[n]$ following some educated assumptions. The level of accuracy of the DFT calculation, thus, depends upon the choice of an exchange-correlation energy functional [41]. In the next section, details regarding some of the widely used exchange-correlation functional are discussed.

2.9 Local Density Approximation

The *Local density approximation* (LDA) is the simplest and the oldest approximation to the exchange-correlation energy functional which is derived using the uniform-electron-gas model of an atom [41]. Therefore, the exchange and correlation energy within this approximation are considered same as that of locally uniform electron gas having same electron density [41]. In general, the exchange-correlation energy functional under the

LDA is expressed as [41]:

$$E_{xc}^{LDA}[n] = \int n(r) \epsilon_{xc}^{hom}(n) dr \quad (2.51)$$

where $n(r)$ represents the local density of uniform electron gas. The corresponding exchange-correlation potential under the LDA scheme then is written as [41]:

$$\begin{aligned} v_{xc}^{LDA}(r) &= \frac{\delta E_{xc}^{LDA}}{\delta n(r)} \\ &= \epsilon_{xc}(n) + n(r) \frac{\delta \epsilon_{xc}}{\delta n} \end{aligned} \quad (2.52)$$

The function $\epsilon_{xc}(n)$ can further be separated into exchange and correlation contributions as [41]:

$$\epsilon_{xc}(n) = \epsilon_x(n) + \epsilon_c(n) \quad (2.53)$$

The exchange part in the above equation due to the Dirac exchange energy functional which is expressed as [41]:

$$\epsilon_x(n) = -C_x n(r)^{1/3} \quad (2.54)$$

where,

$$C_x = \frac{3}{4} \left(\frac{3}{\pi} \right)^{1/3} \quad (2.55)$$

The correlation energy for the homogeneous electron gas cannot be calculated in an analytic form and is, thus, often fitted to an accurate quantum Monte Carlo calculation [41, 64].

The LDA has long been used to successfully calculate various properties such as total energy, band structure, vibrational frequencies, elastic moduli etc. of a bulk solid. It is mostly found that LDA underestimate the correlation energy whereas it overestimates the exchange energy; this inherent property of systematic error cancellation qualifies it to produce a reasonably accurate value of exchange-correlation energy [41]. However, it fails miserably in predicting the binding energies, bond lengths and lattice constants in the case of insulators and semiconductors.

2.10 General Gradient Approximation

LDA assumes the behavior of the system of interacting electrons exactly same as that of the homogeneous electron gas. But in reality, the electron density in any such system is inhomogeneous. To incorporate this inhomogeneous nature of electron density, the *general gradient approximation* (GGA) makes the exchange-correlation energy functional to also depend on local gradient of electron density in addition to the local density of electrons.

The general functional form of GGA is written as:

$$E_{xc}^{GGA}[n] = \int f(n(r), |\nabla n(r)|) n(r) dr \quad (2.56)$$

Unlike LDA, there is no unique form for the GGA functional, thus it exists in many flavors which are developed to meet the requirements of the specific kind of systems. The most

widely used GGA functional in recent times is GGA-PBE, which is due to Perdew, Burke, and Ernzerhof [65]. In general, the GGA gives a better estimate of bond length and binding energies but like LDA, it also fails to account for the van der Waal interaction [66, 67].

2.11 Hybrid Functionals

Hybrid functionals are another class of approximations developed to account for the shortcomings of LDA and GGA. It incorporates a portion of exact exchange taken from the Hartree-Fock theory in addition to the exchange and correlation contributions from other available functional. In recent times, these are the most reliable class of exchange-correlation functional which predict very accurate results than other available functional [52–54]. These are also known as implicit density functionals because the exact exchange is expressed in terms of Kohn-Sham orbitals rather than density. One of the most widely used functional, as such, in recent times, is known as B3LYP functional [53, 68–70]. The correlation contribution in B3LYP comes from LYP(Lee-Yang-Parr) GGA and the exchange part is taken from the Becke’s three-parameter hybrid functional B3. [53, 68–70]. The B3LYP hybrid exchange-correlation functional is expressed as [70]:

$$E_{xc}^{B3LYP} = E_{xc}^{LDA} + a_0(E_x^{HF} - E_x^{LDA}) + a_x(E_x^{GGA} - E_x^{LDA}) + a_c(E_c^{GGA} - E_c^{LDA}) \quad (2.57)$$

where $a_0 = 0.20$, $a_x = 0.72$, and $a_c = 0.81$ are the semi-empirical parameters calculated by appropriately fitting the data of experimental atomization energies, ionization potentials, proton affinities, and total atomic energies.

Though hybrid functionals deal with the exchange and correlation in a more accurate manner than LDA and GGA, it comes at the cost of more computational power. Therefore, to use this functional for bigger systems that involve hundreds of atoms is still a challenge.

Chapter 3

Quantum Transport Theory

3.1 Introduction

This chapter describes in detail, the theory of electronic transport in nanoscale junctions. At this lengthscale, the quantum effects play a major role in dictating the electronic transport behavior in a junction, thus, it cannot be described by a classical transport theory [42, 71, 72]. Therefore, to have a complete understanding of the electronic transport phenomena, one needs to incorporate the quantum nature of electron by explicitly including the electron-electron interaction into account [42, 72]. Since a minor fluctuation in device length at nano-regime can potentially distort the whole process of electronic transport, a basic understanding of various fundamental lengthscales is crucial to developing an efficient

nano junction device. Therefore, the first section of this chapter presents an overview of various characteristic lengthscales in relation to the electronic transport through the nano-junction. This will then be followed by a section on device modeling, in which, details regarding (i) the Landauer's formalism of electronic transport, (ii) the single-particle many-body Green's function approach, and (iii) the formalism of spin-dependent transport will be discussed.

3.2 An Overview of Fundamental Lengthscales in Solids

The idea of wave-particle duality developed by de Broglie (de Broglie hypothesis) interprets electron both as a particle and a wave [73]. The wavelength of an electron, also known as de Broglie's wavelength [73], plays a crucial role in determining the transport. It is found that at low temperature only those electrons which are in the immediate vicinity of the Fermi energy do contribute to the electronic transport. This further depends on the scattering potential due to disorder or lattice vibration in the solid state system and requires it to be comparable to the Fermi wavelength of the electrons for the quantum effects to be more prominent. [37]. Quantitatively, the Fermi wavelength of an electron is expressed as

[42, 72]:

$$\begin{aligned}\lambda_f &= 2\pi/k_f \\ &= 2\pi/\sqrt{2\pi n_s} \\ &= \sqrt{2\pi/n_s}\end{aligned}\tag{3.1}$$

where k_f and n_s are the respective Fermi wave vector and electron density of a two-dimensional electron gas.

Now scatterings in solids can further be divided into two types: elastic scattering and inelastic scattering, depending upon the energy changes during the scattering process. If the energy during the process is conserved, it is known as an elastic scattering otherwise, the process becomes inelastic. Moreover, the average distance traveled by an electron between two successive elastic scatterings is material characteristic known as the elastic mean free path; during this scattering process, the phase of the electron wavefunction, too, remains conserved. The general expression for the elastic mean free path is given as [42, 71, 72]:

$$l_m = v_f \tau_m\tag{3.2}$$

where v_f and τ_m are the respective Fermi velocity and momentum relaxation time. In relation to the above-discussed lengthscale l_m , the electronic transport in a nanoscale junction becomes *ballistic* if the channel length of the device is smaller than its elastic mean free

path, beyond which the particle is scattered during the transport, resulting into a diffusive process.

In contrast to the above-explained elastic scattering process, there occurs a dephasing of electron wavefunction when it encounters an inelastic scattering during the transport. This, in turn, originates another material characteristic lengthscale known as phase coherence length; it is defined as the average distance traveled by an electron during successive inelastic scatterings. It is of utmost importance when considering transport through a mesoscopic junction as the quantum interference effect comes into existence only if the channel length of a device is smaller than its phase coherence length; the transport in such cases is said to be *coherent* in relation to the conservation of electron wave function [42, 71, 72]. The general expression of phase coherence length is given as

$$l_{\phi} = v_f \tau_{\phi} \quad (3.3)$$

where τ_{ϕ} is the phase relaxation time.

Finally, this section is concluded by discussing, yet another, nanoscopic lengthscale related to spin orientation of electrons. This lengthscale known as spin diffusion length is defined as the distance over which an electron keeps its spin (memory) intact during the transport. Spin coherence length in terms of diffusion constant (D) and spin relaxation time τ is

expressed as [37]:

$$l_{sd} = \sqrt{D\tau} \quad (3.4)$$

Since it is a material property that depends on spin-orbit coupling and hyperfine interaction, the materials with low atomic numbers (Z) are found to have the longer spin-coherence length.[74]. For instance, the spin-coherence length of carbon nanotube is reported to be 130 nm [31].

3.3 Device Modeling

A typical nanoscale junction consists of a channel (spacer) sandwiched between the two electrodes (semi-infinite charge reservoir). The electrode from which electrons are pumped into the spacer is called the *source* and the one into which it pumps out is called the *drain*. Figure (3.1) shows a prototypical three-terminal nanoscale junction device. The electronic transport in a nanoscale junction constitutes a non-equilibrium statistical problem [42, 72]. To solve this problem, following assumptions are made: the current in the junction is constant over time and the energy levels inside the channel are discrete and stationary.

However, to work as a junction device, the channel requires to exchange its energy and electrons with the external semi-infinite electrodes which constitute an *open* system. To model such an open junction device of nano-dimension, we partition it into three different

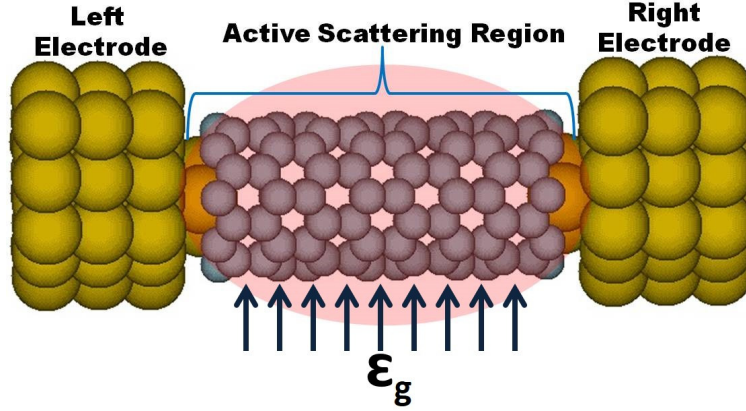


Figure 3.1: A prototypical three-terminal nanoscale junction with a nanotube spacer. The connection between the channel and the semi-infinite external electrodes is made via left and right leads of the *active scattering region*; ϵ_g represents the gate field applied perpendicular to the channel.

regions; the channel, the *leads* and the semi-infinite electrodes [42, 75]. The channel together with the strongly coupled leads on its both ends form the *active scattering region*. The leads at both ends of the channel are composed of few atoms, equal in number, and are attached to the left and right semi-infinite electrodes. When attached to the extended structure (active scattering region), the semi-infinite electrodes remain unperturbed and are assumed to retain their bulk properties [42, 75]. To make electrons flow through the channel, we need to have a non-equilibrium situation in which the chemical potentials in the left and right electrodes are not equal. The difference in the chemical potential is expressed as $\mu_{1,2} = E_f \mp V_{low,high}$, where $\mu_{1,2}$ are the respective chemical potential at left and right electrodes; E_f is the equilibrium Fermi energy and $V_{low,high}$ are the voltage drops at the respective electrodes [75]. To obtain the voltage drop at each applied dipole perturbative field, the self-consistently calculated potentials at finite bias is averaged over the total number of atoms at each lead which is then subtracted from the similarly calculated average

potential at zero bias for the same lead [75]. The potential difference between the source and drain is then obtained by subtracting V_{low} from V_{high} ; at equilibrium $V_{low} = V_{high} = 0$ [75]. To model the effect of the electrostatic gating, a dipole interaction term, $\vec{\epsilon}_g \cdot \sum_i \vec{r}(i)$ is added to the core Hamiltonian of the active scattering region; $\vec{\epsilon}_g$ is the gate field applied perpendicular to the channel axis and $\vec{r}(i)$ represents the coordinate of i th electron [76, 77]. The self-consistent addition of dipole interaction term in the core Hamiltonian let us incorporate the first and higher order Stark effect explicitly in our calculation [76, 77]. Finally, the calculation of tunneling current is performed by using the Landauer approach to be discussed in the following section.

3.3.1 Electronic Transport in a Nanoscale Junction: Landauer's Approach

The Landauer's approach to describing the electronic transport in a semiconductor nanoscale junction is found to be valid only for the coherent transport regime ; the device size should be shorter than the phase coherence length of the electron [42, 72, 78, 79]. Figure (3.2) shows the schematic diagram of a nanoscale junction device. Leads at both sides of the

scattering region (channel) are identical with the electrons free to travel along the x-direction and confined in y and z-directions. The Hamiltonian for the active scattering

region is given as [42, 72]:

$$H_S = -\frac{\hbar^2}{2m}\nabla^2 + V(r) \quad (3.5)$$

which satisfies the following asymptotic conditions [42, 72]:

$$\lim_{x \rightarrow -\infty} H_S = -\frac{\hbar^2}{2m}\nabla^2 + V_L(r) \equiv H_L, \quad (3.6)$$

and

$$\lim_{x \rightarrow +\infty} H_S = -\frac{\hbar^2}{2m}\nabla^2 + V_R(r) \equiv H_R \quad (3.7)$$

Since the solutions of the Schrödinger wave equation (SWE) for both H_L and H_R are similar, once solved for the one, it can be generalized for the other. Therefore, the SWE for H_L is expressed as

$$\left[-\frac{\hbar^2}{2m}\nabla^2 + V_L(r) \right] \psi_{nk}(r) = E_n \psi_{nk}(r) \quad (3.8)$$

The general solution for Eq.(3.8) is expressed as the product of the transverse and longitudinal components [72]:

$$\psi_{nk}(r) = \sqrt{\frac{1}{L_x}} u_n(r_\perp) e^{ikx}, \quad -\infty < k < +\infty \quad (3.9)$$

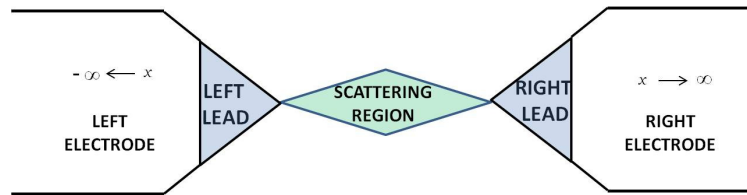


Figure 3.2: Schematic representation of a typical nanoscale junction

with the eigen-energy

$$E_n(k) = \varepsilon_n + \frac{\hbar^2 k^2}{2m} \quad (3.10)$$

Though Eq.(3.9) gives a finite probability of finding electron everywhere in space, only non-decaying solutions of Eq.(3.8) do contribute to the probability density [42, 72]. Now the solutions for H_R can be obtained in a similar way.

With these, for a given E , the SWE for the Hamiltonian is written as

$$\left[-\frac{\hbar^2}{2m} \nabla^2 + V(r) \right] \phi_{nk}(r) = E \phi_{nk}(r) \quad (3.11)$$

where the solutions $\phi_{nk}(r)$ can be determined using the asymptotic boundary conditions:

$$\lim_{x \rightarrow \mp \infty} \phi_{nk}(r) = \psi_{nkL,R}(r) \quad (3.12)$$

Out of the possible eigenstates traveling both ways in the active scattering region, let's consider the one traveling from left to right. For this, consider an electron with energy E_i at the region $x \rightarrow -\infty$ with the initial eigenstate $\psi_{ik_i}(r)$. It is difficult to exactly specify the state of an electron in the active scattering region due to the complex nature of $V(r)$, however, in the region $x \rightarrow +\infty$ of the right electrode, the electron eigenstate can simply be obtained from a linear combination of eigenstates of H_R expressed as [42, 72]:

$$\phi_{ik_i}^+(r) \rightarrow \sum_{f=1}^{N_R} t_{if} \psi_{fk_f}(r), \quad x \rightarrow +\infty \quad (3.13)$$

where N_R represents the number of eigenchannels in the right lead corresponding to a given energy and t_{if} are complex coefficients. The state of the electron in Eq.(3.13) is labeled with a '+' symbol to show that it originated from wavefunction $\psi_{ik_i}(r)$. Furthermore, the state of an electron in the deep left lead is not only due to the incident wave but also has some contribution from the back-scattered states from the junction. Considering the above fact, the electron state at the deep left lead can be written as [42, 72]:

$$\phi_{ik_i}^+(r) \rightarrow \psi_{ik_i}(r) + \sum_{f=1}^{N_L} r_{if} \psi_{fk_f}(r), \quad x \rightarrow -\infty \quad (3.14)$$

where N_L is the number of channels in the lead for the given energy and r_{if} are the complex coefficients.

Therefore, the average current $I(E_i)$ carried by the state at energy E_i across a surface perpendicular to the x-axis is obtained as

$$\begin{aligned} I_i(E_i) &= e \langle \phi_{ik_i}^+ | \hat{j} | \phi_{ik_i}^+ \rangle \\ &= \frac{e\hbar}{2im} \int_{-\infty}^{+\infty} dy \int_{-\infty}^{+\infty} dz \left[[\phi_{ik_i}^+(r)]^* \frac{\partial \phi_{ik_i}^+(r)}{\partial x} - \phi_{ik_i}^+(r) \frac{\partial [\phi_{ik_i}^+(r)]^*}{\partial x} \right] \\ &= \frac{e\hbar k_i}{mL_x} \\ &= \frac{ev_i(k_i)}{L_x} \end{aligned} \quad (3.15)$$

Following the steady-state assumption of the current throughout the system, the current in

the deep left lead in accordance with its electron state takes the form [42, 72]:

$$I_L(E_i) = I_i(E_i) \left(1 - \sum_{f=1}^{N_L} R_{if}(E_i) \right) \quad (3.16)$$

where the quantity $R_{if}(E_i)$ is known as the reflection coefficient which is expressed as

$$R_{if}(E_i) \equiv |r_{if}|^2 \frac{|I_f(E_i)|}{|I_i(E_i)|} \quad (3.17)$$

where $I_i(E_i)$ is the current carried by the initial state ψ_{ik_i} .

Similarly, the current deep into the right lead can be expressed as [42, 72]:

$$I_R(E_i) = I_i(E_i) \sum_{f=1}^{N_R} T_{if}(E_i) \quad (3.18)$$

with the Transmission coefficient, $T_{if}(E_i)$ expressed as:

$$T_{if}(E_i) \equiv |t_{if}|^2 \frac{|I_f(E_i)|}{|I_i(E_i)|} \quad (3.19)$$

Assuming a steady current throughout the device requires deep left and deep right leads to having the same current. This implies that if we start from the right electrode with initial wavefunction ψ_{ik_i} , we would reach to similar expressions of current for the above two leads due to the transmitted and reflected states [42, 72].

Total Current: Considering the fact that at a finite bias, the left and right electrodes will be

at two different chemical potentials ($\mu_{L,R}$), the distribution or the occupancy of electrons in these electrodes will be different too. Following this in addition to the assumption that the participating eigenchannels are independent, the total current which is the sum of currents carried by all channels at all energies is given as [42, 72]:

$$I = 2 \int dE \left[\sum_{i=1}^{N_L} \sum_{f=1}^{N_R} f_L(E) D_i(E_i) I_i(E_i) T_{if}(E_i) - \sum_{i=1}^{N_R} \sum_{f=1}^{N_L} f_R(E) D_i(E_i) I_i(E_i) T_{if}(E_i) \right] \quad (3.20)$$

where the factor 2 arises to account for the two different electronic spin degree of freedom;

f_L and f_R represent the Fermi distribution function

$$f_{L,R} = \frac{1}{e^{(E-\mu_{L,R})/K_B T} + 1} \quad (3.21)$$

in the left and right electrodes.

The density of state $D_i(E_i)$ of a 1-D lead is given as

$$\begin{aligned} D_i(E_i) &= \frac{L_x}{2\pi} \frac{dk_i}{dE_i} \\ &= \frac{L_x}{2\pi\hbar v_i} \end{aligned} \quad (3.22)$$

The transmission coefficients from right to left and left to right defined in terms of transmission probabilities can be expressed as [42, 72]:

$$T_{RL}(E) = \sum_{i=1}^{N_R} \sum_{f=1}^{N_L} T_{if}(E), \quad R \rightarrow L \quad (3.23)$$

and

$$T_{LR}(E) = \sum_{i=1}^{N_L} \sum_{f=1}^{N_R} T_{if}(E), \quad L \rightarrow R \quad (3.24)$$

These transmission coefficients must be equal to conserve the particle flux during the transport. Therefore,

$$T_{LR} = T_{RL} = T(E) \quad (3.25)$$

Finally, substituting the expressions for density of states $D_i(E_i)$ and current $I_i(E_i)$ in Eq.(3.19), the total current in terms of transmission function $T(E)$ becomes [42, 72]:

$$\begin{aligned} I &= \frac{e}{\pi\hbar} \int dE [f_L(E) - f_R(E)] T(E) \\ &= \frac{2e}{h} \int dE [f_L(E) - f_R(E)] T(E) \end{aligned} \quad (3.26)$$

3.3.2 Single Particle Many-Body Green's Function Approach

The Landauer's approach discussed in the previous section derived the expression for electronic current in a nanoscale junction in terms of the transmission function. In this section,

the calculation of transmission function in a nanoscale junction using the real space single particle many-body Green's function approach is discussed [42, 72]. As discussed previously, the nanoscale device is partitioned into three different regions; the left electrode, the active scattering region including the leads and the right electrode. The electrodes do not interact directly with each other but are coupled to the active scattering region via coupling potentials, thereby, making the total Hamiltonian of the partitioned nanoscale heterostructure take the form [42, 72]:

$$\begin{aligned}
H &= H_L + H_R + H_S + C_{LS} + C_{LS}^\dagger + C_{SR} + C_{SR}^\dagger \\
&= H_L + H_R + H_S + C_{LS} + C_{SL} + C_{SR} + C_{RS}
\end{aligned} \tag{3.27}$$

where H_L , H_R , and H_S are the respective Hamiltonians of the left electrode, right electrode, and the middle scattering region; (C_{LS}, C_{SL}) and (C_{SR}, C_{RS}) are the coupling potentials representing the coupling of the middle region with left and right electrodes, respectively [42, 72]. The Schrödinger wave equation for the Hamiltonian in the matrix form can be written as [42, 72]:

$$\begin{pmatrix} H_L & C_{LS} & 0 \\ C_{LS}^\dagger & H_S & C_{SR}^\dagger \\ 0 & C_{SR} & H_R \end{pmatrix} \begin{pmatrix} |\Phi_L\rangle \\ |\Phi_S\rangle \\ |\Phi_R\rangle \end{pmatrix} = E \begin{pmatrix} |\Phi_L\rangle \\ |\Phi_S\rangle \\ |\Phi_R\rangle \end{pmatrix} \tag{3.28}$$

where $|\Phi_L\rangle$, $|\Phi_S\rangle$, and $|\Phi_R\rangle$ are the single particle wavefunction representing the eigenfunctions of H_L , H_S , and H_R , respectively; E is injection energy of the tunneling electron.

Simplifying the above matrix equation (3.28), we get:

$$H_L|\Phi_L\rangle + C_{LS}|\Phi_S\rangle = E|\Phi_L\rangle \quad (3.29)$$

$$C_{LS}^\dagger|\Phi_L\rangle + H_S|\Phi_S\rangle + C_{SR}^\dagger|\Phi_R\rangle = E|\Phi_S\rangle \quad (3.30)$$

$$C_{SR}|\Phi_S\rangle + H_R|\Phi_R\rangle = E|\Phi_R\rangle \quad (3.31)$$

Solving Eq.(3.29), we get:

$$|\Phi_L\rangle = G_L C_{LS}|\Phi_S\rangle \quad (3.32)$$

Similarly, solving (3.31), gives:

$$|\Phi_R\rangle = G_R C_{SR}|\Phi_S\rangle \quad (3.33)$$

where,

$$G_{L,R} = \frac{1}{E - H_{L,R}} \quad (3.34)$$

is the Green's function for left and right electrodes.

Now, substituting the solutions (3.32) and (3.33) in Eq.(3.30) and solving it, we get:

$$\begin{aligned} C_{LS}^\dagger G_L C_{LS} |\Phi_S\rangle + H_S |\Phi_S\rangle + C_{SR}^\dagger G_R C_{SR} |\Phi_S\rangle &= E |\Phi_S\rangle \\ \Rightarrow (E - H_S - \Sigma_L - \Sigma_R) |\Phi_S\rangle &= 0 \end{aligned} \quad (3.35)$$

where $\Sigma_L = C_{LS}^\dagger G_L C_{LS}$ and $\Sigma_R = C_{SR}^\dagger G_R C_{SR}$ are the respective self-energy functions for the left and right interfaces which enable the exchange of electron and energy between the channel and the external electrodes.

Now, the Green's function associated with Eq.(3.35) is given as [42, 72]:

$$G(E) = \frac{1}{E - H_S - \Sigma_L - \Sigma_R} \quad (3.36)$$

The above result (3.36) is also known as retarded Green's function which, in the time domain, acts as a response function to an impulse excitation at time $t=0$ [42]. Thus, we have transformed the very complicated problem involving the entire system into the problem of active scattering region, which is *open* to both the electrodes through the use of self-energy function [42, 72]. The self-energy functions are non-Hermitian matrices whose imaginary part gives the broadening function; it broadens the energy levels in the active scattering region when attached to the semi-infinite electrodes. The broadening function, thus, is defined as [42, 72]:

$$\Gamma_{L,R} = i[\Sigma_{L,R} - \Sigma_{L,R}^\dagger] \quad (3.37)$$

After having defined the retarded Green's function and the broadening function in terms of self-energy function, we are now ready to define the transmission function as [42, 72]:

$$T(E) = Tr[\Gamma_L G \Gamma_R G^\dagger] \quad (3.38)$$

which gives the sum of transmission coefficients over all the eigenchannels available in the active scattering region. The transmission function gives the probability of crossing the active scattering region by the electron while on its way from source to drain.

Now, to calculate the self-energy matrices and the Green's function for a real system under the non-equilibrium situation, we apply an electric field $\vec{\epsilon}$ along the channel axis. We incorporate this field effect in the Hamiltonian of the active scattering region by defining a perturbed Hamiltonian as [42, 72]:

$$H(E, \epsilon) = H_0 + \vec{\epsilon} \cdot \sum_i \vec{r}(i) \quad (3.39)$$

where H_0 and $\vec{r}(i)$ are the respective *unperturbed* Hamiltonian of the active scattering region and the coordinates of the i^{th} electron. The single electron energy levels of the active scattering region are obtained through self-consistent field calculation using the finite cluster density functional theory. The use of real space approach for the active scattering region allows the partition of $H(E, \epsilon)$ to obtain the molecular Hamiltonian $H_M(E, \epsilon)$ representing only the channel part [42, 72]. The bias-dependent single particle Green's function of the

molecular or the channel portion of the active scattering region is then given as

$$G_M(E, \varepsilon) = [E \times S - H_M(\varepsilon) - \Sigma_L(\varepsilon) - \Sigma_R(\varepsilon)]^{-1} \quad (3.40)$$

where E is the injection energy of the tunneling electron; S is an overlap matrix of the same dimension as that of H_M ; Σ_L and Σ_R are the respective bias-dependent self-energy functions which enable the lead-molecule interaction. The bias-dependent self-energy functions $\Sigma_{L,R}$ are related to the orthogonalized bias-dependent coupling matrices $C_{L,R}$ through the relation [42, 72]:

$$\Sigma_{L,R} = C_{L,R}^\dagger G_p C_{L,R} \quad (3.41)$$

where G_p is the Green's function for both the leads as we considered same leads on either side of the channel. In the wideband approximation, G_p is obtained by calculating first the bulk density of states (DOS) of the metal of which the lead is made from. Then, we calculate the DOS per electron in the unit cell ($\eta(E)$) and use it to express G_p as:

$$G_p(E) = -i\pi\eta(E) \times I \quad (3.42)$$

where I represents an $n \times n$ identity matrix; n is the total number of Gaussian basis functions used to represent the atoms forming the leads in the active scattering region.

3.3.3 Theory of Spin Transport

The discussion of the electronic transport, done so far, emphasized only the charge aspect of an electron. Since our study of electronic transport includes both the charge (spin-unpolarized) as well as the spin (spin-polarized) transport, this section is devoted to discussing the spin-polarized electron transport in a nanoscale junction. Utilizing the spin degree of freedom to build the nanoscale magnetic devices can be realized in two different ways: the first one is to take the magnetic electrodes such as Ni, Co, and Fe and a non-magnetic channel; the other way is to take the non-magnetic electrodes and the magnetic channel. A device built with a non-magnetic channel sandwiched in between two magnetic electrodes is known as a spin valve device [80–82]. And, the one in which a magnetic channel is sandwiched in between two non-magnetic electrodes is called a spin filtering device [83, 84]. Let us first discuss the transport in a spin-valve device. Depending upon the magnetic orientation of the electrodes, there are two possible configurations of the spin valve device. The one in which both the electrodes are having the same magnetic orientation is known as parallel configuration (PC) and the other configuration in which two electrodes are magnetized in the opposite direction is known as antiparallel configuration (APC). Attaching a non-magnetic channel with the magnetic electrodes partially magnetizes the channel at the interface due to the magnetic proximity effect [75]. Because of this, the molecular Hamiltonian, as well as the self energy matrices, become magnetic in nature

and the Green's function for the molecular part of a spin valve becomes [75]:

$$G_M^\sigma(E, \varepsilon) = [E \times S - H_M^\sigma(\varepsilon) - \Sigma_L^\sigma(\varepsilon) - \Sigma_R^\sigma(\varepsilon)]^{-1} \quad (3.43)$$

where σ represents the different spin states (\uparrow or \downarrow) of an electron.

Similarly, the spin-polarized self-energy matrices are expressed as [75]:

$$\Sigma_{L,R}^\sigma = C_{L,R}^{\sigma\dagger} G_p^\sigma C_{L,R}^\sigma \quad (3.44)$$

where the spin-polarized Green's function of the leads G_p^σ is given as

$$G_p^\sigma = -i\pi\eta^\sigma \times I \quad (3.45)$$

If G_{pL}^σ and G_{pR}^σ are the respective Green's function of the left and right lead?

then, in the case of PC, we get

$$G_{pL}^\sigma = -i\pi\eta^\sigma \times I; G_{pR}^\sigma = G_{pL}^\sigma \quad (3.46)$$

But, in the case of APC where the leads have opposite magnetic orientation, we have two different possibilities.

For $\sigma = \uparrow$

$$G_{PR}^{\downarrow} = -i\pi\eta^{\downarrow} \times I; G_{PL}^{\uparrow} = -i\pi\eta^{\uparrow} \times I \quad (3.47)$$

and for $\sigma = \downarrow$

$$G_{PR}^{\uparrow} = -i\pi\eta^{\uparrow} \times I; G_{PL}^{\downarrow} = -i\pi\eta^{\downarrow} \times I \quad (3.48)$$

where η^{\uparrow} and η^{\downarrow} are the respective DOS per electron in the unit cell for UP and DOWN spin states. The spin-polarized bulk DOS of magnetic electrodes is calculated using the periodic density functional theory. To bring the energy level of the semi-infinite electrodes and the active scattering region at the same scale, the Fermi energy of the bulk electrode is aligned with the Fermi energy of the active scattering region at equilibrium. The equilibrium Fermi energy of the active scattering region for PC and APC is given by the highest occupied molecular orbital (HOMO). The finite lead at each end of the active scattering region and the respective semi-infinite electrode are assumed to have the same magnetic domain [75].

Now, let us consider the transport in the case of the spin-filtering device. As it is built from a non-magnetic electrode, the Green's function for the lead would be spin-unpolarized. The molecular Hamiltonian and the self-energy function, on the other hand, would be spin-polarized because of a magnetic channel. The Green's function of the molecular part of the active scattering region and the rest of the transport theory would be same as that of a spin-valve device.

Chapter 4

Semiconductor Core-Shell Nanowire

Field Effect Transistors[†]

4.1 Introduction

Semiconductor core-shell nanowires are one-dimensional radial heterostructures having a different atomic composition in the core and the shell region [6–29]. Due to its unique electronic structure [8], this nanowires [6–29] have shown exciting promise in recent years

[†]Portion of this chapter is adapted from the Nano Letters vol.16, page 3995-4000, year 2016 by Kamal B. Dhungana, Meghnath Jaishi, and Ranjit Pati (Kamal B. Dhungana initiated this project and is not a part of his thesis; the major portion of the calculation, analysis and writing work for this project is done by Meghnath Jaishi under the guidance of Prof. Ranjit Pati) and the Nanoscale vol.9, page 13425-13431, year 2017 by Meghnath Jaishi and Ranjit Pati. Copyright: Appendix A - DOI: 10.1021/acs.nanolett.6b00359 & Appendix B - DOI: 10.1039/c7nr05589g

with applications in quantum computing [12, 24], field effect transistors [6, 8, 17, 18, 21], Josephson junctions[9], thermoelectric materials[19], and Esaki tunnel diodes[26, 85]. The valence band offsets in these nanowires help to reduce the carrier scattering at the nanowire surface and provide a unique opportunity to drive the carrier transport through either core or shell region [6–8, 11, 18, 21]. The recent improvements in synthesis techniques have made it possible to prepare these nanowires in high yield with reproducible electronic properties coupled with the ability to control their diameter as well as the core-shell interface [6, 8, 86, 87].

Furthermore, these nanowires provide us with an excellent opportunity of coaxial gating which helps to suppress the off state leakage current for high-performance FET[6, 22]. Due to these important features and its compatibility to the present Si-based technology, the core-shell nanowire is considered as a viable alternative for the next-generation electronics. For instance, the Ge-Si core-shell nanowire with transparent contacts has been demonstrated to exhibit ballistic transport (mean free path ~ 500 nm) [8] behavior at a low bias. The scaled transconductance and ON current in this heterostructure are reported to be 3 to 4 times higher than that observed in state-of-the-art metal oxide semiconductor field effect transistors (MOSFETs) [8]. These materials also do not require doping [7, 8] and are compatible with the current CMOS technology as dry or wet oxidation approach at elevated temperature can be used to form an insulating oxide layer around the nanowire for coaxial gating[6, 22]. High-performance Esaki tunnel diodes have also been fabricated

from small-diameter Ge/Si core-shell nanowires vertically grown on Si substrate[85]. Significant enhancement in mobility is also reported for a coherently strained Ge-Si core-shell nanowire channel [28]. Programmable nanowire field effect transistors (FETs) made out of Ge-Si core-shell nanowires have also been proposed [20]. In the case of a Si-Ge core-shell nanowire FET, a significant enhancement in carrier mobility is observed upon reducing the Si-core size [30]. These pioneering experimental works [6–8, 13, 20, 30, 86] provide an ideal testing ground for quantum theory to investigate transport phenomena in this low dimensional system.

There have been numerous theoretical works carried out to understand the electronic structure, energetics, quantum confinement effects, the role of doping, core-shell composition dependent strain, and thermoelectric properties in Ge-Si core-shell nanowires [88–104]. But, only limited attention has been given thus far to comprehend the observed electron transport phenomena in the semiconductor core-shell nanowire-metal junction[13, 105]. Electron transport in a low dimensional nanoscale junction is a non-equilibrium quantum mechanical process[42, 72]; it cannot simply be assessed adequately from the energy band diagram of the current carrying channel structure alone; the effect of the external bias including the electrostatic gating effect as well as the metal/nanowire contact structure need to be considered explicitly to gain insights into the transport phenomena. Therefore, a detailed understanding of carrier transport in a nanoscale junction requires a first principles approach that does not make any assumption on electronic structure, charge and potential profile of the device. So far, only a semi-classical, ballistic transport model [13] has been

adopted to analyze the observed superior performance of the Ge-Si core-shell nanowire FET. However, a visual manifestation of the electronic quantum path within the Ge-Si core-shell nanowire FET in a nonequilibrium condition would provide a detailed insight into the quantum origin of its functionality, which is not attainable by a semi-classical approach.

In this chapter, the results of work done to investigate the quantum transport properties of semiconductor Si-Ge and Ge-Si core-shell nanowire quantum dot field effect transistors of different core diameter are presented. The first section of this chapter explains the observed superior performance of Si-Ge core-shell nanowire field effect transistor in comparison to its homogeneous silicon counterpart. Similarly, the results of quantum transport study that explains the observed anomalous gate driven negative differential resistance behavior in Ge-Si core-shell nanowire field effect transistor at a higher gate bias is discussed in the next section.

4.2 Superior Performance of a Si-Ge Core-Shell Nanowire Field Effect Transistor

The sustained advancement in semiconductor core-shell nanowire technology has unlocked a tantalizing route for making next-generation field effect transistor (FET). Understanding how to control carrier mobility of these nanowire channels by applying a gate field is the

key to developing a high-performance FET. Herein, we have identified the switching mechanism responsible for the superior performance of a Si-Ge core-shell nanowire quantum dot FET over its homogeneous Si counterpart. A quantum transport approach is used to investigate the gate-field modulated switching behavior in electronic current for ultranarrow Si and Si-Ge core-shell nanowire quantum dot FETs. To avoid unintended scattering, the unsaturated surface states of the nanowire quantum dots are passivated by hydrogen atoms. Irrespective of channel length, our calculations yield excellent gate field induced switching behavior in current for both the pristine Si and the Si-Ge core-shell heterostructure nanowire quantum dots. Within the gate bias range considered here, the transconductance, dI_{sd}/dV_g , is found to be much higher in the case of a Si-Ge core-shell nanowire FET than in the Si nanowire FET; this suggests a much higher mobility in the Si-Ge nanowire device. The gate bias dependent transmission and participating spatial pathway (frontier orbital in the active scattering region) are analyzed to understand the observed superior performance of the Si-Ge core-shell nanowire quantum dot FET. For the ON state, the gate-field induced transverse localization of the wave function restricts the carrier transport to the outer (shell) layer with p_z orbitals providing the pathway for tunneling of electrons in the channels. The higher ON state current in the Si-Ge core-shell nanowire FET is attributed to the p_z orbitals that are distributed over the entire channel; in the case of Si nanowire, the participating p_z orbital is restricted to a few Si atoms in the channel resulting in a higher tunneling barrier and thus the smaller ON state current. For the OFF state, no quantum states are available within the chemical potential window to observe any appreciable current at a low bias.

4.2.1 Computational Methods

The cross-sectional and the extended perspective view of the relaxed $\langle 110 \rangle$ Si and Si-Ge core-shell nanowires used in this investigation are shown in Figure 4.1. A periodic density functional theory (DFT) [41] that employs plane wave basis functions and generalized gradient approximation (GGA) for the exchange-correlation is used to determine their electronic structures.

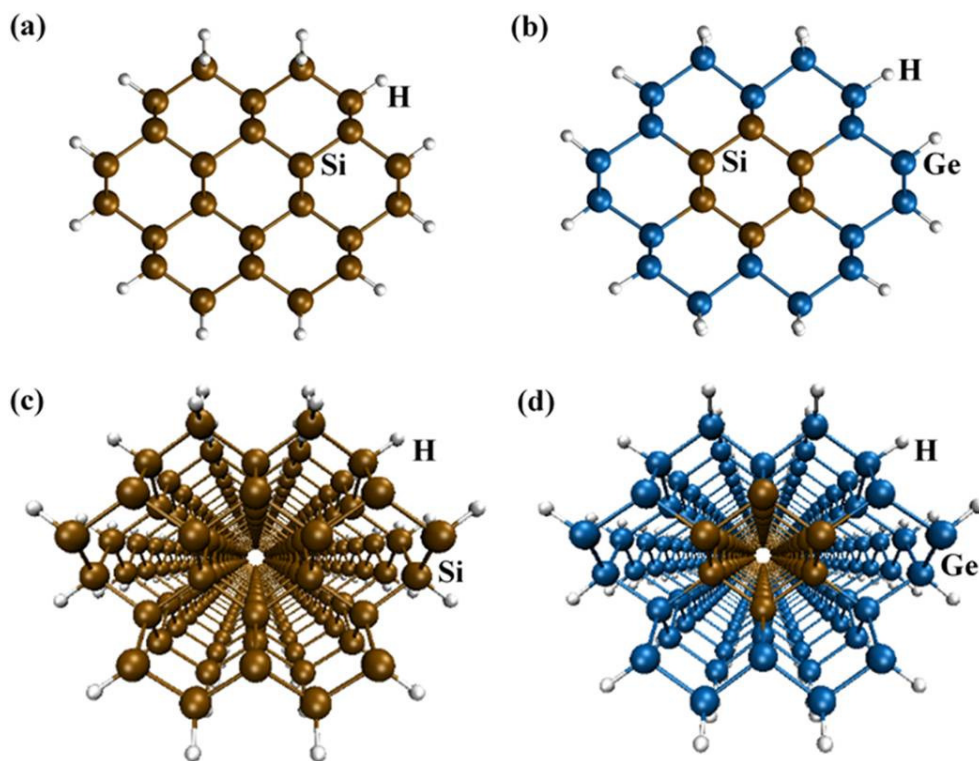


Figure 4.1: Optimized structures of the H-passivated Si and Si-Ge core-shell nanowires along the $\langle 110 \rangle$ direction. A cross-sectional view of (a) Si nanowire and (b) Si-Ge core-shell nanowire; extended view of (c) Si nanowire and (d) Si-Ge core-shell nanowire. (Reprinted with permission from K. B. Dhungana, M. Jaishi, and R. Pati, *Nano Letters* 2016, 16, 3995–4000. Copyright (2016) American Chemical Society.)

We have used the projector augmented wave (PAW) pseudopotentials to describe the valence-core interactions. For the geometry optimization, the atomic structure of the nanowires are allowed to relax without symmetry constraint until the residual force on each atom becomes less than 0.01 eV/\AA ; the energy convergence criterion is set at 10^{-6} eV . The optimum lattice parameter of the nanowire is obtained by minimizing the total energy with respect to the variation of lattice parameter along the z-axis; the lattice parameters are found to be 3.90 and 4.09 \AA for the Si nanowire and Si-Ge core-shell nanowire, respectively. Table 4.1 and 4.2 show the respective optimized coordinates of the atoms in the unit cell of Si and Si-Ge core-shell nanowires. We have the Vienna *ab initio* simulation code (VASP) [106, 107] to perform the calculation. The kinetic energy cutoff of 18.37 Ry and a supercell comprised of 40 atoms (24 Si and 16 H for the Si nanowire; 6 Si, 18 Ge and 16 H for the Si-Ge core-shell nanowire) are considered. To minimize the spurious interaction between the nanowire and its periodic images, we have considered a supercell of 35 \AA along the x- and y-direction to ensure large enough vacuum space (more than 20 \AA) between the nearest H atoms of the neighboring nanowires. The Monkhorst-Pack (MP) scheme with the $(1 \times 1 \times 7)$ k-point grid is used to sample the Brillouin zone. To ensure the accuracy of our electronic structure calculations, extensive convergence tests are carried out by varying the k-point mesh and the vacuum space used in the supercell. Changing the supercell size from 35 to 40 \AA along the x- and y-direction yields only a change of 5 meV in total energy (less than 0.12 meV per atom). Varying the k-point from $(1 \times 1 \times 7)$ to $(1 \times 1 \times 13)$ also leads to a much smaller change in the fundamental gap (less than 1 meV).

Table 4.1

The optimized coordinates of the atoms in a $\langle 110 \rangle$ Si nanowire unit cell. (Reprinted with permission from K. B. Dhungana, M. Jaishi, and R. Pati, *Nano Letters* 2016, 16, 3995–4000. Copyright (2016) American Chemical Society.)

Translational lattice parameter = 3.90 Å				
Serial Number	Atom	X(Å)	Y(Å)	Z(Å)
1	Si	13.0086	7.62523	1.9518
2	Si	14.94758	8.91663	2.30214
3	Si	16.88404	7.62203	1.95181
4	Si	18.81782	8.92459	2.2767
5	Si	18.83384	10.26854	0.32409
6	Si	20.74803	11.64953	0.3028
7	Si	20.74645	12.98028	2.25426
8	Si	18.83237	14.36226	2.23464
9	Si	18.81726	15.70674	0.28142
10	Si	16.88606	17.01318	0.60749
11	Si	14.94915	15.71696	0.26796
12	Si	13.0115	17.0077	0.62225
13	Si	11.08147	15.70117	0.29832
14	Si	11.06522	14.35811	2.24982
15	Si	9.14692	12.98197	2.26385
16	Si	9.14808	11.6517	0.31174
17	Si	11.0657	10.27526	0.32448
18	Si	11.0785	8.93214	2.27622
19	Si	13.00733	12.99725	2.2612
20	Si	14.95033	14.35808	2.2226
21	Si	16.89327	12.99591	2.25783
22	Si	16.89357	11.63386	0.31005
23	Si	14.94886	10.2753	0.34764
24	Si	13.00725	11.63707	0.31241
25	H	13.03438	17.2265	2.1115
26	H	9.85112	16.57204	0.31501
27	H	20.04821	16.57775	0.29427
28	H	7.92773	13.86974	2.26044
29	H	21.96922	13.86255	2.25433
30	H	21.97071	10.76658	0.30341
31	H	7.93022	10.76234	0.31553
32	H	9.84622	8.06355	2.262
33	H	20.0467	8.05073	2.26778
34	H	16.86229	7.40096	0.46311
35	H	13.03061	7.40572	0.46284
36	H	13.0029	6.24663	2.54126
37	H	16.8829	6.24546	2.54586
38	H	16.8729	17.24054	2.09445
39	H	16.8808	18.38814	0.00996
40	H	13.00632	18.38603	0.03266

Table 4.2

The optimized coordinates of the atoms in a $\langle 110 \rangle$ Si-Ge core-shell nanowire unit cell. (Reprinted with permission from K. B. Dhungana, M. Jaishi, and R. Pati, *Nano Letters* 2016, 16, 3995–4000. Copyright (2016) American Chemical Society.)

Translational lattice parameter = 3.90 Å				
Serial Number	Atom	X(Å)	Y(Å)	Z(Å)
1	Si	13.00545	12.97187	2.18768
2	Si	13.00534	11.66018	0.14012
3	Si	14.94709	10.28418	0.14306
4	Si	16.88816	11.66054	0.14033
5	Si	14.94723	14.3485	2.18934
6	Si	16.88812	12.97133	2.18772
7	Ge	11.01264	14.37682	2.18563
8	Ge	8.95872	13.00474	2.18457
9	Ge	8.9588	11.62758	0.13706
10	Ge	11.01272	10.25496	0.13814
11	Ge	10.98494	8.84922	2.18549
12	Ge	12.97925	7.42596	2.18647
13	Ge	14.9478	8.91379	2.19133
14	Ge	16.91813	7.42828	2.17128
15	Ge	18.91173	8.85245	2.18711
16	Ge	18.88208	10.25772	0.13951
17	Ge	20.93817	11.62692	0.13734
18	Ge	20.93778	13.00457	2.18494
19	Ge	18.88186	14.37461	2.18733
20	Ge	18.91121	15.77964	0.13994
21	Ge	16.91896	17.2056	0.14669
22	Ge	14.94878	15.71925	0.14245
23	Ge	12.97958	17.20607	0.13977
24	Ge	10.98484	15.78287	0.13798
25	H	13.02428	18.14798	1.37363
26	H	9.66391	16.63092	0.13828
27	H	20.23468	16.62376	0.13941
28	H	7.72655	13.97638	2.18415
29	H	22.16759	13.97949	2.18423
30	H	22.16832	10.65226	0.13699
31	H	7.72681	10.65573	0.13665
32	H	9.6642	8.00101	2.18581
33	H	20.234	8.00649	2.18641
34	H	16.86794	6.51219	0.91887
35	H	13.03023	6.48658	0.95112
36	H	13.02338	6.48217	3.41878
37	H	16.87291	6.46171	3.38613
38	H	16.87336	18.14155	1.38499
39	H	16.8695	18.15148	3.01119
40	H	13.02823	18.14794	3.00098

change in the energy gap between valence and conduction band at the Γ -point). This clearly suggests that the use of Monkhorst-Pack (MP) scheme with $(1 \times 1 \times 7)$ k-point mesh to sample the Brillouin zone is sufficient to achieve the desired accuracy in energy band structure. The fundamental gaps for Si and Si-Ge core-shell nanowires are found to be 1.73 and 1.24 eV, respectively. Both nanowires exhibit direct band gaps at Γ point, which are consistent with previous reports [97–100]. The significant reduction ($\sim 28\%$) in the energy band gap of the Si-Ge core-shell nanowire is due to the intrinsic strain caused by the lattice mismatch at the Si-Ge interface [97]. To gain deeper insights into the strain caused by the lattice mismatch, we analyze the relaxed atomic structures of Si and Si-Ge core-shell nanowires. In the case of a Si nanowire, the Si-Si distances are found to be 2.37 Å for the core Si atoms and 2.35 Å for the surface Si atoms that are saturated by H atoms. The core-shell interfacial Si-Si distances are found to be 2.38 Å. The Si-H bond lengths are found to vary between 1.51 to 1.50 Å depending upon whether the corresponding Si atom is passivated by one or two hydrogen atoms. A similar variation in the bond lengths is reported in H-passivated Si nanowire [108]. For the Si-Ge core-shell nanowire, the Si-Si distances are stretched to 2.43 Å in the core region exhibiting a 2.5% tensile strain, which is in agreement with the previous result [97]. The surface Ge-Ge distances are found to be 2.47 Å, Ge-H bond lengths vary between 1.57 to 1.55 Å and the interfacial Si-Ge distances are found to be 2.46 Å.

Then, we recourse to a real space bias-dependent single particle many-body Green's function approach [42, 72, 75, 76, 109, 110] to model the Si and Si-Ge nanowire quantum dot FETs. A fragment of the optimized nanowire directed along the $\langle 110 \rangle$ direction is used as

a channel between a pair of semi-infinite gold electrodes to model an open device structure; 24 gold atoms are explicitly included in the active scattering region of the device to incorporate the charging effect on the nanowire. To discern the role of the channel from contacts, we have used the same interface geometry for both the nanowire FETs. It should be noted that the growth direction of Si and Ge nanowires depends upon the size of the nanowires: they most likely prefer to grow along the $\langle 110 \rangle$ direction when the diameter of the nanowire becomes less than 20 nm [111, 112]. Because the unsaturated surface states of the nanowire are passivated by hydrogen atoms and electrons are strongly confined to the nanowire, we term the nanowire channel as a quantum dot.

For our current calculation, we have used the *posteriori* hybrid density functional method (B3LYP) (see section 2.11) [70, 76] that includes a part of the exact Hartree-Fock (HF) exchange and is proven to give better result for conductance than the conventional density functional approach (LDA/GGA) (see section 2.9 & 2.10) [76]. The inclusion of exact exchange from the HF method corrects partly the self-interaction error that occurs in conventional DFT. Though a true dynamical exchange-correlation corrected potential[113] with a higher level GW approach [114] would provide a much better description of transmission through the channel, its complete implementation is prohibitively difficult here. We have used the LAND2DZ pseudopotential Gaussian basis set[70] to describe the atoms in the active scattering part of the device. A single particle dipole interaction term $\vec{\epsilon}_g \cdot \sum_i \vec{r}(i)$ is included in the core Hamiltonian to simulate the effect of the electrostatic gating[76, 77]. The gate field, $\vec{\epsilon}_g$, is applied in the direction perpendicular to the channel axis (x-axis); $\vec{r}(i)$

is the coordinate of the i^{th} electron. We have aligned the Fermi energy of the active scattering region of the device with that of the bulk gold electrode at equilibrium[75]. The gate bias, V_g , is obtained from the voltage drop across the radial direction for each applied gate field. The self-consistent inclusion of dipole interaction term in the Hamiltonian allows us to include both first and higher order Stark effects explicitly in our calculations[76, 77].

4.2.2 Results and Discussions

4.2.2.1 Current-Voltage Characteristics

Current-voltage characteristics for the Si and Si-Ge core-shell nanowire quantum dot FETs are presented in Figure 4.2. For a small bias range considered here, both FETs show linear I-V characteristic in the absence of gate bias. When the gate bias is included, source-drain currents for the FETs increase nonlinearly with an increase in bias; a linear and a saturated regime (ON-state) in the current, which is a typical feature of an FET, is clearly noticeable for a higher gate bias. A similar FET feature has been reported in the Si nanowire transistors [115], fabricated using atomic force microscopy nanolithography with channel width as small as 4 nm. To confirm the current-voltage characteristics obtained here as a general feature of these quantum dot FETs irrespective of channel lengths, we have presented results for two different channel lengths. Though the same number of atoms are considered to model the channel, the channel length in the Si nanowire quantum dot FET is slightly

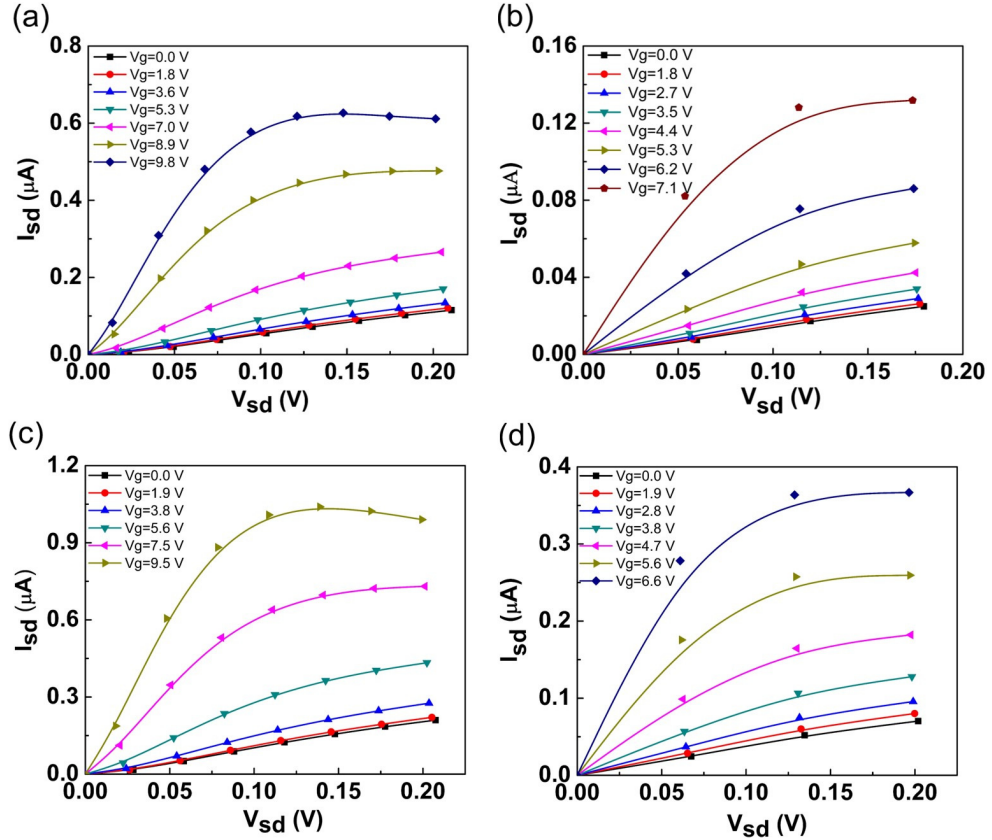


Figure 4.2: Gate bias dependent current-voltage characteristics. (a, b) Si nanowire quantum dot FETs of channel lengths 13.65 and 17.55 Å, respectively. (c, d) Si-Ge core-shell nanowire quantum dot FETs of channel lengths 14.30 and 18.40 Å, respectively. (Reprinted with permission from K. B. Dhungana, M. Jaishi, and R. Pati, *Nano Letters* 2016, 16, 3995–4000. Copyright (2016) American Chemical Society.)

smaller than that in the Si-Ge nanowire FET due to a lattice mismatch between Si and Ge. For similar dimensions (for example, Figure 4.2b,d), the Si-Ge nanowire FET exhibits a higher current than the Si nanowire FET at the same gate bias. For the quantitative comparison of performance between Si and Si-Ge nanowire FETs, we have plotted source-drain current as a function of gate bias (Figure 4.3a,b) for the fixed source-drain bias of ~ 0.2 V. Despite having a longer channel length than its homogeneous Si counterpart, the Si-Ge core-shell nanowire quantum dot FET yields the higher ON-state current.

4.2.2.2 Transconductance

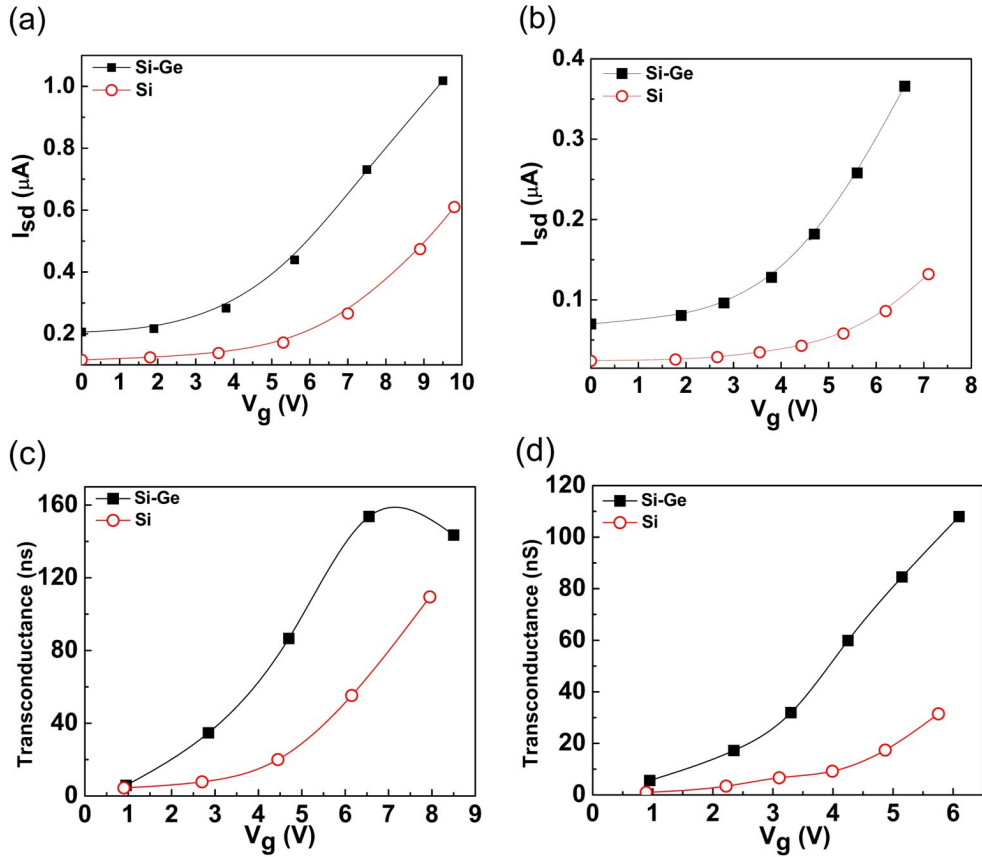


Figure 4.3: Source-drain current (I_{sd}) and transconductance as a function of gate bias (V_g) for the Si and Si-Ge core-shell nanowire quantum dot FETs at a fixed source-drain bias of ~ 0.2 V. (a, c) Channel lengths for the Si and Si-Ge nanowire devices are 13.65 and 14.30 Å, respectively. (b, d) Channel lengths for the Si and Si-Ge nanowire devices are 17.55 and 18.40 Å, respectively. (Reprinted with permission from K. B. Dhungana, M. Jaishi, and R. Pati, *Nano Letters* 2016, 16, 3995–4000. Copyright (2016) American Chemical Society.)

To further substantiate the results obtained from the current-voltage characteristics, we have plotted transconductance - a key metric in benchmarking the transistor performance, using the consecutive data points from the I_{sd} versus V_g plot (Figure 4.3a,b), the transconductance is calculated as $dI_{sd}/dV_g = (I_{sd}(n+1) - I_{sd}(n))/(V_g(n+1) - V_g(n))$. We have assigned

this transconductance value to a gate bias of $(V_g(n+1) + V_g(n))/2$; n is the index of the data sets. The results for two different channel lengths are summarized in Figure 4.3c,d. Irrespective of the gate bias and the channel length, the transconductance is found to be substantially higher in the Si-Ge core-shell nanowire than in the Si nanowire FET. For example, for the longer channel length (Figure 4.3d), the transconductance at $V_g = 1.5V$ is found to be 1.68 nS and 9.69 nS for Si and Si-Ge nanowire FET respectively; dI_{sd}/dV_g is $\sim 475\%$ higher in the case of a Si-Ge core-shell nanowire FET. For a higher gate bias of 5.5 V, the dI_{sd}/dV_g in the Si-Ge nanowire FET is found to be 93.25 nS (244% higher) as compared to 27.09 nS for the Si nanowire FET. This suggests that the mobility, which is proportional to dI_{sd}/dV_g , would be much higher in the Si-Ge core-shell nanowire FET than in the Si nanowire FET for switching the device from the OFF state to the ON state.

4.2.2.3 Transmission

To understand the superior performance of the Si-Ge core-shell nanowire FET over the Si nanowire FET; we have calculated the transmission as a function of injection energy for different gate bias; transmission represents the sum of transmission probabilities over all eigenchannels in the device [75]. These results are summarized in Figure 4.4. Several remarks are in order. First, in the absence of gate bias, no transmission peaks are observable in the vicinity of Fermi energy resulting in a much smaller current for the OFF state. As the gate bias increases, more and more transmission peaks appear within the [-0.5 eV, 0.5 eV]

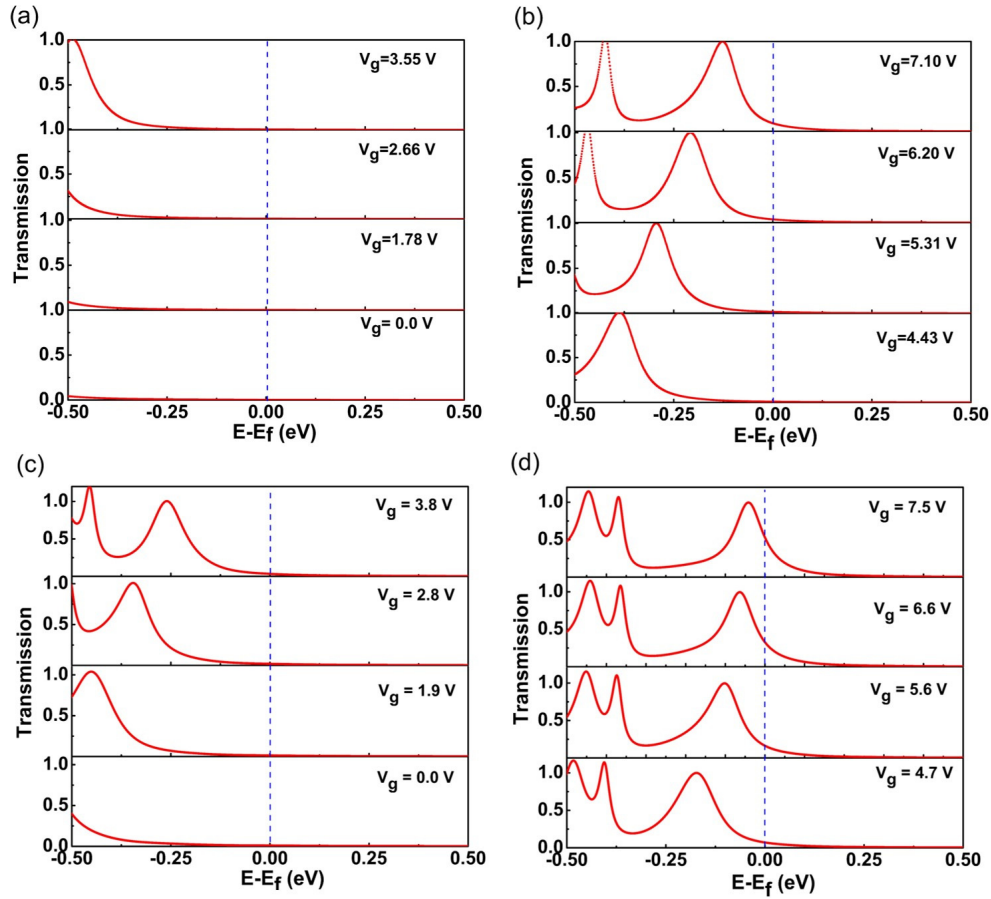


Figure 4.4: Transmission as a function of injection energy for different gate bias at equilibrium ($V_{sd} = 0.0$ V). (a, b) Data for a Si nanowire FET of channel length 17.55 \AA . (c, d) Data for a Si-Ge core-shell nanowire FET of channel length 18.40 \AA . (Reprinted with permission from K. B. Dhungana, M. Jaishi, and R. Pati, *Nano Letters* 2016, 16, 3995–4000. Copyright (2016) American Chemical Society.)

energy window. For a higher gate bias, the number of transmission peaks that appear within the energy window is higher in the case of a Si-Ge core-shell nanowire FET than in the Si nanowire FET. This explains the higher ON state current in the Si-Ge core-shell nanowire FET. Second, a strong gate bias induced shift in transmission peak position toward the Fermi energy is noted for the Si-Ge nanowire FET. This unambiguously explains why a smaller gate bias is required to switch the Si-Ge nanowire FET from the OFF state to the

ON state relative to that in the Si nanowire FET. It should be noted that we have considered the transmission energy window range from -0.5 eV to +0.5 eV in order to elucidate the gate bias induced shifting of transmission peak positions. For our current calculation, we have integrated the transmission function between the chemical potential window (CPW), which are determined from the voltage drop at the electrodes [75–77], for V_{sd} of 0.2 V, the CPW is [-0.1 eV, 0.1 eV].

A close examination of currents for shorter channel lengths also shows a negative differential resistance (NDR) behavior [116] at a higher gate bias (Figure 4.2a,c). To understand this intriguing behavior, we have calculated the transmission as a function of source-drain bias in the Si-Ge core-shell nanowire quantum dot FET at a gate bias of 9.5 V. For brevity, we have considered only the Si-Ge nanowire FET of channel length 14.30 Å. The source-drain bias of 0.14 V (the peak current state) and 0.20 V (a valley current state following the peak current state) are considered; the results are presented in Figure 4.5. Figure 4.5a shows a shift in transmission peak positions away from the Fermi energy as the bias increases from 0.14 to 0.20 V. As can be seen in Figure 4.5b, the chemical potential window increases with an increase in bias from 0.14 to 0.20 V. However, the value for the transmission coefficient decreases as we increase the bias leading to a decrease in area under the curve within the CPW. This results in a drop in current as we increase the bias from 0.14 to 0.20 V leading to an NDR behavior.

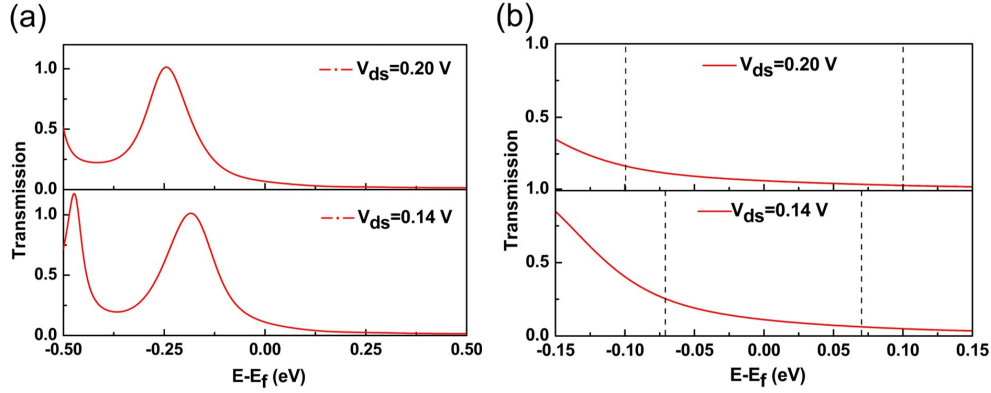


Figure 4.5: Transmission as a function of injection energy for different source-drain bias ($V_g = 9.5$ V; channel length is 14.30 \AA) in the Si-Ge core-shell nanowire FET. (a) Transmission in the energy window of $[-0.5 \text{ eV}, 0.5 \text{ eV}]$. (b) Zoomed-in version of the transmission in the energy window of $[-0.15 \text{ eV}, 0.15 \text{ eV}]$; the dotted lines represent the chemical potential window for the respective applied bias. (Reprinted with permission from K. B. Dhungana, M. Jaishi, and R. Pati, *Nano Letters* 2016, 16, 3995–4000. Copyright (2016) American Chemical Society.)

4.2.2.4 Orbital Level Explanation

Transmission clearly explains the observed superior performance of Si-Ge core-shell nanowire FET over its homogeneous Si counterpart, however, several questions arise: Why does the Si-Ge core-shell nanowire FET exhibit a stronger response to the gate bias than Si nanowire FET? Does the core Si layer or the shell Ge layer provide the pathway for electron transport in the Si-Ge nanowire FET? To answer these subtle questions, we have analyzed the frontier orbitals in the active scattering part that contribute to the transmission (highest occupied orbital in this case) in the ON-state for both the channels. Orbital analysis shows that for the ON state, the gate field-induced transverse localization (direction perpendicular to the channel axis) of the wave function restricts the carrier transport to the shell layer. In the case of the Si nanowire channel, the outer Si layer offers the pathway for

electron transport. For the Si-Ge core-shell nanowire channel, electrons tunnel through the shell Ge layer of the channel. In both cases, the p_z orbitals in the channel that couple to the s-orbitals of the Au lead provides the spatial pathway for electron tunneling as shown in Figure 4.6. For the ON state, in the case of the Si-Ge core-shell nanowire channel, the p_z orbitals are distributed over the entire channel length (Figure 4.6b), which leads to the higher ON-state current. On the other hand, the participating p_z orbitals are restricted to a few Si atoms in the outer layer of the channel for the Si nanowire FET (Figure 4.6a). The stronger response to the gate bias observed in the Si-Ge nanowire FET as compared to the Si nanowire FET can be understood as follows. First, due to a strong structural asymmetry

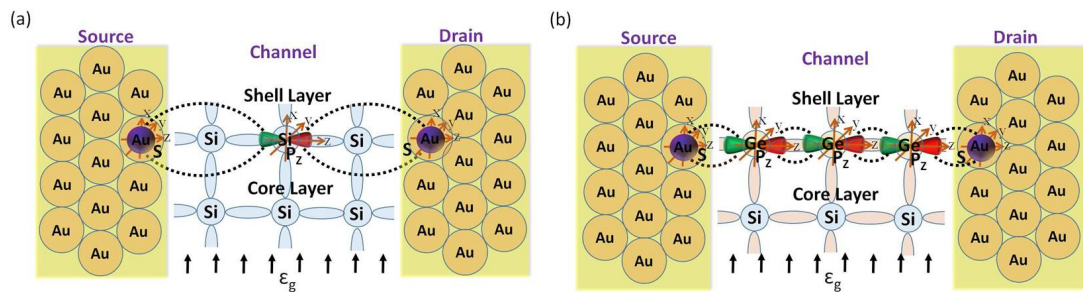


Figure 4.6: A schematic to elucidate the electronic orbital control mechanism for the superior performance of a (b) Si-Ge core-shell nanowire quantum dot FET over (a) the Si nanowire quantum dot FET. For the ON state, carrier transport is restricted to the shell layer. The p_z orbitals provide the pathway for tunneling of electrons. (Reprinted with permission from K. B. Dhungana, M. Jaishi, and R. Pati, *Nano Letters* 2016, 16, 3995–4000. Copyright (2016) American Chemical Society.)

in the radial direction, the symmetry of the wave function in the Si-Ge nanowire is broken along the direction perpendicular to the channel-axis (in the absence of gate field). This results in a strong mixing of broken symmetry eigen-channel states upon the application of the transverse gate field, which causes a shift of eigen-channel toward the Fermi energy

(Figures 4.4c,d). Second, in the Si-Ge core-shell nanowire FET, the lattice mismatch induced strain in the radial direction develops a strong dipole moment and polarizability in the transverse direction as shown in Table 4.3, which results in a much stronger response to the transverse electric field via the Stark effect.

Table 4.3

Dipole moment and polarizability. Components of dipole moment (α) and polarizability (β) for the Si and Si-Ge core-shell nanowire junctions. The channel lengths for Si and Si-Ge core-shell nanowires are 17.55 Å and 18.40 Å, respectively. (Reprinted with permission from K. B. Dhungana, M. Jaishi, and R. Pati, *Nano Letters* 2016, 16, 3995–4000. Copyright (2016) American Chemical Society.)

Nanowire	Dipole moment (a.u.)			Polarizability (a.u.)					
	α^x	α^y	α^z	β^{xx}	β^{yx}	β^{yy}	β^{zx}	β^{zy}	β^{zz}
Si	-0.71	0.52	-0.46	3976.74	-1.23	3591.14	-3.22	-25.77	6051.23
Si-Ge	-1.05	0.26	0.04	4387.76	-1.72	3883.38	-2.72	-25.9	7081.26

4.2.2.5 Length-dependent Transport

We have also calculated the current-voltage characteristics of Si and Si-Ge core-shell nanowires in a two-probe set up for additional channel lengths (at $V_g = 0.0$ V) as shown in Figure 4.7. The results reveal the electron tunneling decay constant to be 0.37 \AA^{-1} in the case of the Si nanowire as compared to the 0.24 \AA^{-1} for the Si-Ge core-shell nanowire which reaffirms our conclusion of superior-mobility in the Si-Ge nanowire device. We also note that even though the diameter of the channel considered in our study is relatively smaller (~ 1.4 nm) than that used in the experimental measurement, we expect the proposed switching mechanism and the observed superior performance behavior of the Si-Ge

core-shell nanowire FET to hold for a larger diameter due to the following reasons. DFT

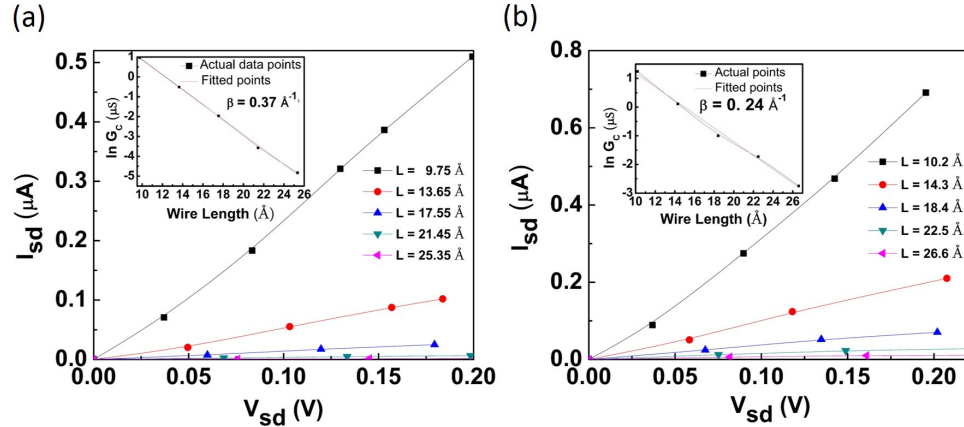


Figure 4.7: Variation of current with the source-drain bias for different channel lengths (L) of (a) Si nanowire junction and (b) Si-Ge core-shell nanowire junction, in the absence of gate bias. The I_{sd} is fitted to a straight line to calculate the conductance (G_C) for different wire lengths (L). The inset shows the $\ln(G_C)$ vs. L plot, which is fitted to a straight line to calculate the electron tunneling decay constant (β) of 0.37 and 0.24 \AA^{-1} for Si and Si-Ge core-shell nanowire junction respectively. (Reprinted with permission from K. B. Dhungana, M. Jaishi, and R. Pati, *Nano Letters* 2016, 16, 3995–4000. Copyright (2016) American Chemical Society.)

calculations based on a local density approximation show that due to the lattice mismatch at the core-shell interface, the strain to core atoms initially increases and then almost saturates when we increase the shell thickness to increase the diameter of the Si-Ge core-shell nanowires from 2.5 to 4.7 nm [97]. On the basis of this result, we expect the strain in the shell layer of the Si-Ge core-shell nanowire to increase if we increase the core thickness to increase the diameter. The increase of radial strain in the nanowire with the increase of diameter would increase the polarizability resulting in a stronger response to gate bias via the Stark effect, which would significantly boost the ON state current value in the Si-Ge nanowire FET. This would then lead to a higher ON/OFF current ratio and transconductance in the Si-Ge core-shell nanowire FET as compared to that in the Si nanowire FET.

Because the radial strain would saturate after we reach an optimum diameter, the polarization will saturate as well as the ON/OFF ratio and the transconductance.

4.2.2.6 Conclusions

In summary, using an exhaustive first-principles quantum transport approach, we have unraveled the gate field-induced switching mechanism which is responsible for the superior performance of the Si-Ge nanowire quantum dot FET over the Si nanowire FET. The Si-Ge core-shell nanowire FET exhibits a much stronger response to the gate field due to the Stark effect as compared to the Si nanowire FET. The transconductance is found to be substantially higher in the Si-Ge core-shell nanowire FET. In the case of a Si-Ge nanowire FET (for the ON state), the gate field-induced transverse localization of the wave function restricts the carrier transport to the shell Ge layer and the p_z orbitals that are distributed over the entire channel provide the pathway for electron tunneling. In contrast, for the Si-nanowire FET, the p_z orbitals that contribute to the current for the ON state are restricted to a few Si-atoms in the outer Si-layer. This results in a higher tunneling barrier in the Si-nanowire FET as compared to that in the Si-Ge core-shell nanowire FET. We expect that the electronic orbital level understanding gained in this study would prove useful for designing a new generation of coreshell nanowire FET.

4.3 Imaging the Quantum Path of Electron in Real Space

Inside a Ge-Si Core-Shell Nanowire Transistor

Catching the electron in action in real space inside a semiconductor Ge-Si core-shell nanowire field effect transistor (FET), which has been demonstrated (J. Xiang, W. Lu, Y. Hu, Y. Wu, H. Yan and C. M. Lieber, *Nature*, 2006, 441, 489) to outperform the state-of-the-art metal oxide semiconductor FET, is central to gaining unfathomable access into the origin of its functionality. Here, using a quantum transport approach that does not make any assumptions on electronic structure, charge, and potential profile of the device, we unravel the most probable tunneling pathway for electrons in a Ge-Si core-shell nanowire FET with orbital level spatial resolution. Our calculation yields excellent transistor characteristics as noticed in the experiment [8]. Upon increasing the gate bias beyond a threshold value, we observe a rapid drop in drain current resulting in a gate bias driven negative differential resistance behavior and switching in the sign of transconductance. We attribute this anomalous behavior in drain current to the gate bias induced modification of the carrier transport pathway from the Ge core to the Si shell region of the nanowire channel. A new experiment involving a four-probe junction is proposed to confirm our prediction on gate bias induced decoupling.

4.3.1 Quantum Modeling

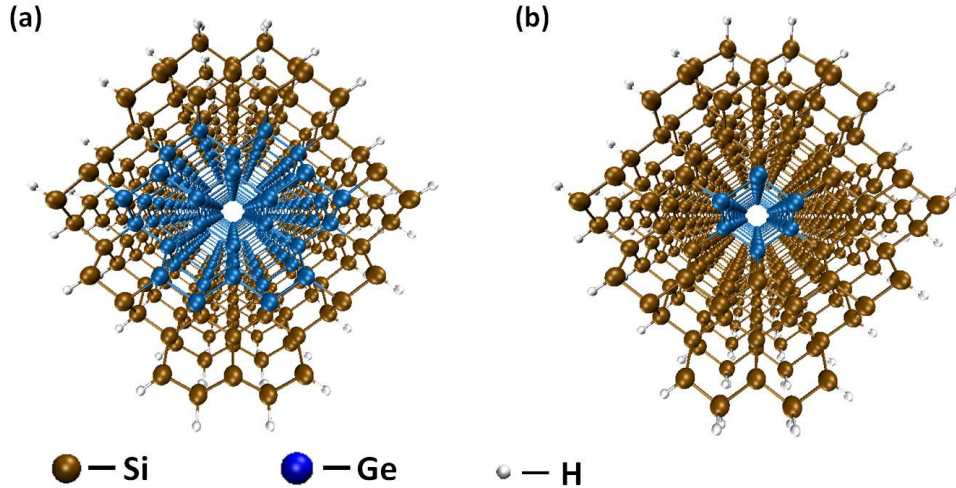


Figure 4.8: Atomic model of the Ge-Si core-shell nanowire. A perspective view of the optimized nanowire structure along the $\langle 110 \rangle$ direction. (a) Core (Ge) diameter is 11.7 Å. (b) Core (Ge) diameter is 4.7 Å. (Reprinted with permission from M. Jaishi, and R. Pati, *Nanoscale* 2017, 9, 13425–13431. Copyright (2017) Royal Society of Chemistry.)

The atomic model of the Ge-Si core-shell nanowires (for two different core diameters) used in our investigation is illustrated in Fig. 4.8; unsaturated surface states are passivated by hydrogen atoms to avoid unintended scattering during the carrier transport. We have considered the nanowire along the $\langle 110 \rangle$ direction as it has been reported to be the preferred growth direction for Ge-Si core-shell nanowires with a diameter smaller than 20 nm[8]. A periodic density functional theory (DFT) that employs plane wave basis sets and a generalized gradient approximation for the exchange-correlation part is used to optimize the atomic coordinates of Ge-Si core-shell nanowires and determine its energy band structure. We have used the projector augmented wave (PAW) approach to include the valence-core

interaction. During the geometry optimization, structural relaxations are carried out without symmetry constraint until the residual force on each atom reduces to $0.01 \text{ eV } \text{\AA}^{-1}$; the convergence criterion for the total energy is set at 10^6 eV . We have used a supercell of 35 \AA along the x and y-direction to avoid spurious interaction between the nanowire and its replicas; the equilibrium lattice parameter is obtained by minimizing the total energy with respect to the variation of primitive unit cell length along the z-axis. The $1 \times 1 \times 7$ k-point grid within the MonkhorstPack (MP) scheme, which has been reported to be sufficient to achieve the desired accuracy in energy band structure of semiconducting core-shell nanowires[117], is used to sample the Brillouin zone. We have used the Vienna *ab initio* simulation package (VASP) to perform this calculation[106, 107]. The optimized primitive unit cell lengths along the z-axis (wire axis) are found to be 3.96 \AA for the model nanowire shown in Fig. 4.8a and 3.91 \AA for the nanowire in Fig. 4.8b. The optimized coordinates of atoms in the unit cell of Ge-Si core-shell nanowires with the Ge-core diameters of 4.7 and 11.7 \AA are shown in Table 4.4 and 4.5 respectively. The expansion of lattice parameter due to an increase of Ge core thickness in the core-shell nanowire (Fig. 4.8a) is expected as the bulk Ge lattice parameter (5.658 \AA) is higher than that of Si (5.430 \AA). A similar trend in lattice parameter with the variation in core thickness has been reported in Ge-Si core-shell nanowires[88, 89]. Bond length analysis in optimized structures shows that the Ge-Ge bond lengths for the core-Ge in Fig. 4.8b is under compressive strain ($\sim 0.8\%$) as compared to the bond lengths in the core structure of Fig. 4.8a.

Table 4.4

Optimized atomic coordinates in the unit cell of Ge-Si core-shell nanowire grown along $\langle 110 \rangle$; Ge-core diameter is 4.7 Å; lattice parameter is 3.91 Å. (Reprinted with permission from M. Jaishi, and R. Pati, *Nanoscale* 2017, 9, 13425–13431. Copyright (2017) Royal Society of Chemistry.)

Serial Number	Atom	X(Å)	Y(Å)	Z(Å)
1	Ge	13.40939	13.19978	0.343533
2	Ge	15.41443	14.6291	0.344314
3	Ge	17.42524	13.20633	0.343256
4	Ge	17.42851	11.73809	2.297581
5	Ge	15.42357	10.30864	2.297846
6	Ge	13.41284	11.7314	2.298
7	Si	13.45014	7.605664	0.342602
8	Si	15.42644	8.906776	0.342842
9	Si	17.40756	7.612876	0.340909
10	Si	21.27749	11.79481	2.295661
11	Si	21.27478	13.16284	0.34135
12	Si	17.38901	17.33058	2.300016
13	Si	15.41155	16.03094	2.299463
14	Si	13.43066	17.32602	2.301072
15	Si	9.560493	13.14257	0.342611
16	Si	9.563571	11.77403	2.297065
17	Si	5.716806	13.11722	0.339229
18	Si	25.11934	13.15295	0.337419
19	Si	25.12154	11.81878	2.292
20	Si	5.720001	11.78279	2.294034
21	Si	23.17207	9.079847	0.335673
22	Si	7.679529	9.0507	0.337488
23	Si	19.39577	10.35182	2.295081
24	Si	23.21028	10.42775	2.291092
25	Si	11.45071	10.33749	2.296799
26	Si	7.636336	10.39883	2.292792
27	Si	7.665144	15.85873	2.299941
28	Si	23.16017	15.88468	2.299247
29	Si	19.388	14.59959	0.343571
30	Si	23.20304	14.53642	0.343327
31	Si	11.442	14.58687	0.34468
32	Si	7.62732	14.50992	0.34422
33	Si	11.4878	15.94099	2.30028
34	Si	9.550457	17.29796	2.305634
35	Si	19.3367	15.95312	2.299244
36	Si	21.26991	17.31555	2.304434
37	Si	19.35028	8.998013	0.339489

Continued on next page

38	Si	21.28725	7.641165	0.332927
39	Si	11.50221	8.983601	0.341376
40	Si	9.570169	7.619544	0.33591
41	Si	21.2358	18.6568	0.35107
42	Si	17.3791	18.68575	0.344556
43	Si	13.43705	18.68161	0.345457
44	Si	9.581287	18.64018	0.352026
45	Si	21.25736	6.299181	2.286691
46	Si	17.40166	6.257301	2.296813
47	Si	13.46091	6.250301	2.298395
48	Si	9.605137	6.277435	2.289822
49	Si	19.3463	4.89959	2.309652
50	Si	15.43392	4.919628	2.336795
51	Si	11.52147	4.885299	2.313056
52	Si	19.3203	20.04873	0.332036
53	Si	15.40683	20.01725	0.307924
54	Si	11.49265	20.03994	0.331909
55	Si	19.2952	21.38916	2.285868
56	Si	15.40588	21.37308	2.25839
57	Si	11.51584	21.38099	2.285405
58	Si	19.32519	3.558583	0.356326
59	Si	15.43711	3.564036	0.386968
60	Si	11.54882	3.544487	0.359638
61	Si	17.34342	22.6691	2.611173
62	Si	13.46682	22.66503	2.612065
63	Si	13.50182	2.26427	0.036755
64	Si	17.37635	2.271493	0.035766
65	H	4.483465	13.98582	0.338636
66	H	26.34777	14.02826	0.336219
67	H	26.35332	10.94826	2.293286
68	H	4.490911	10.90854	2.294685
69	H	24.41427	8.223427	0.337124
70	H	6.440373	8.190032	0.339011
71	H	6.422316	16.7147	2.300359
72	H	24.39907	16.74626	2.300504
73	H	22.45632	19.54382	0.350633
74	H	8.357311	19.52264	0.350502
75	H	22.48219	5.417975	2.288908
76	H	8.383883	5.391972	2.292173
77	H	20.51161	22.28047	2.301186
78	H	10.29834	22.27109	2.300461
79	H	20.54495	2.672271	0.342343
Continued on next page				

80	H	10.33331	2.652602	0.345849
81	H	17.31873	22.88799	0.190512
82	H	17.33588	24.0482	2.022505
83	H	13.49149	22.88427	0.191526
84	H	13.47568	24.04376	2.022829
85	H	13.52879	2.036616	2.459404
86	H	13.51125	0.8894	0.63372
87	H	17.34876	2.041989	2.458127
88	H	17.37282	0.896354	0.633548

Table 4.5

Optimized atomic coordinates in the unit cell of Ge-Si core-shell nanowire grown along $\langle 110 \rangle$; Ge-core diameter is 11.7 Å; lattice parameter is 3.96 Å. (Reprinted with permission from M. Jaishi, and R. Pati, *Nanoscale* 2017, 9, 13425–13431. Copyright (2017) Royal Society of Chemistry.)

Serial Number	Atom	X(Å)	Y(Å)	Z(Å)
1	Ge	13.41796	7.43168	3.265047
2	Ge	15.42623	8.874996	3.266321
3	Ge	17.43972	7.438885	3.263995
4	Ge	21.48012	11.7411	1.282765
5	Ge	21.47743	13.21566	3.263426
6	Ge	17.4222	17.5059	1.289895
7	Ge	15.41336	16.06344	1.288673
8	Ge	13.39951	17.499	1.289365
9	Ge	9.35808	13.1958	3.265823
10	Ge	9.361645	11.72068	1.285247
11	Ge	13.39783	13.19282	3.267877
12	Ge	15.41567	14.61379	3.268619
13	Ge	17.43804	13.19942	3.266333
14	Ge	17.44049	11.74614	1.285964
15	Ge	15.42319	10.32479	1.286333
16	Ge	13.40093	11.73932	1.287528
17	Ge	19.45496	10.32253	1.283503
18	Ge	11.39172	10.30851	1.285474
19	Ge	19.44816	14.62885	3.266896
20	Ge	11.38266	14.61584	3.268358
21	Ge	11.36116	16.07803	1.288823
22	Ge	19.46482	16.09093	1.287477
23	Ge	19.47707	8.86065	3.263145
24	Ge	11.37517	8.84622	3.265095
25	Si	5.60446	13.11989	3.26221
26	Si	25.23259	13.15342	3.258715
Continued on next page				

27	Si	25.23522	11.81526	1.277888
28	Si	5.607594	11.7814	1.281391
29	Si	23.36241	8.947122	3.255456
30	Si	7.489799	8.9189	3.258739
31	Si	23.41883	10.2902	1.276233
32	Si	7.428697	10.26204	1.279528
33	Si	7.475896	15.99072	1.2896
34	Si	23.35037	16.0157	1.286891
35	Si	23.41125	14.67275	3.26551
36	Si	7.41921	14.64702	3.268363
37	Si	9.367335	17.4519	1.29615
38	Si	21.45451	17.47072	1.294118
39	Si	21.47079	7.486862	3.253768
40	Si	9.386508	7.465036	3.256393
41	Si	21.33001	18.80349	3.275827
42	Si	17.38635	18.89856	3.269141
43	Si	13.43049	18.89176	3.268614
44	Si	9.487955	18.78548	3.277831
45	Si	21.35079	6.153448	1.272599
46	Si	17.40889	6.045923	1.284891
47	Si	13.4536	6.038655	1.285965
48	Si	9.511399	6.131875	1.275184
49	Si	19.40412	4.76385	1.29369
50	Si	15.43379	4.716309	1.327077
51	Si	11.4632	4.749073	1.295981
52	Si	19.37812	20.18595	3.257675
53	Si	15.40608	20.22117	3.229049
54	Si	11.43558	20.17421	3.259191
55	Si	19.33797	21.51572	1.276751
56	Si	15.40483	21.55816	1.243103
57	Si	11.47325	21.50447	1.278367
58	Si	19.36816	3.433633	3.274915
59	Si	15.43674	3.379242	3.313535
60	Si	11.50494	3.419135	3.277307
61	Si	17.37834	22.80732	1.592667
62	Si	13.42848	22.80286	1.593999
63	Si	13.4649	2.12696	2.965656
64	Si	17.41285	2.134083	2.964797
65	H	4.303361	13.88501	3.260802
66	H	26.52973	13.92502	3.257209
67	H	26.53488	11.04791	1.276663
68	H	4.310495	11.00968	1.280036
Continued on next page				

69	H	24.60484	8.089003	3.254612
70	H	6.250462	8.056266	3.257949
71	H	6.233953	16.8498	1.289127
72	H	24.59004	16.87788	1.286709
73	H	22.50201	19.75579	3.272856
74	H	8.312959	19.73421	3.275176
75	H	22.52646	5.205878	1.274374
76	H	8.339404	5.179732	1.276591
77	H	20.53552	22.43286	1.289447
78	H	10.27438	22.41976	1.289876
79	H	20.56784	2.519477	3.262566
80	H	10.30908	2.499517	3.264598
81	H	17.3626	23.04672	3.079274
82	H	17.41146	24.17567	0.979171
83	H	13.44387	23.04163	3.080615
84	H	13.38951	24.17102	0.981004
85	H	13.48113	1.883454	1.480264
86	H	13.43197	0.76136	3.584024
87	H	17.39523	1.889539	1.479473
88	H	17.45198	0.768292	3.583394

Upon decreasing Ge core diameter from 11.7 Å to 4.7 Å, the Ge-Si core-shell interface bond lengths decrease by 0.4%. To elucidate the impact of these structural differences on the electronic structure of these nanowires, atom decomposed energy band structure together with charge density profiles at valence band maximum and conduction band minimum are plotted in Fig. 4.9. Both nanowires (Fig. 4.8a and b) exhibit valence band offset between the Ge-core and Si-shell with a direct band gap at the Γ point; the respective fundamental gaps are found to be 0.89 eV and 0.90 eV, which are consistent with the previous results [88, 89, 93, 94]. From Fig. 4.9a and b, one can also notice that the core Ge atoms primarily contribute to the valence band at the Γ point and the shell Si atoms to the conduction band irrespective of their core diameter. This behavior is also evident from

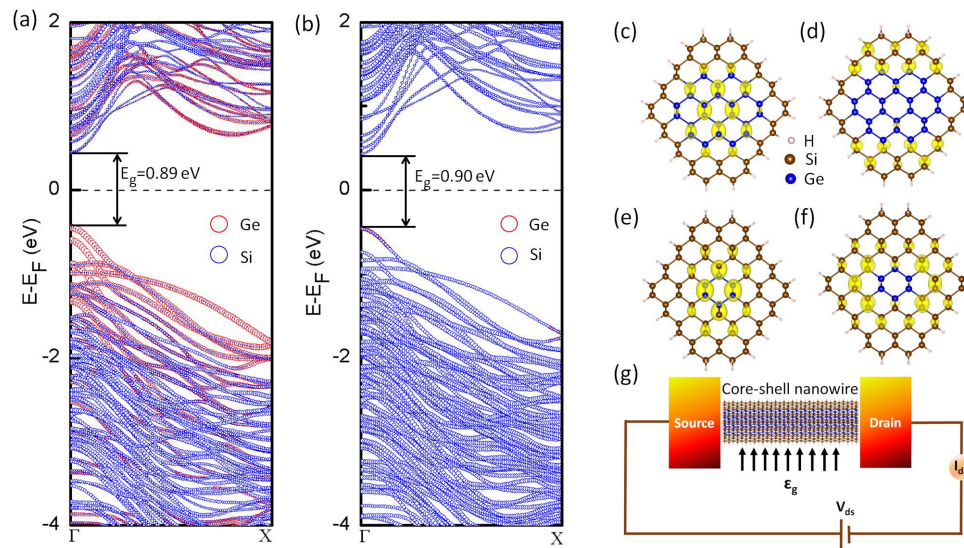


Figure 4.9: Electronic band structure, band-decomposed charge density, and device configuration. Atom decomposed electronic band structure of surface passivated Ge-Si core-shell nanowires. (a) Ge core-diameter 11.7 Å. (b) Ge core-diameter 4.7 Å. Size of the circle determines the weightage of the atom. (c) & (d) Represent charge density plot (2D) at valence band maximum (VBM) and conduction band minimum (CBM) respectively for core diameter 11.7 Å. (e) & (f) Represent charge density plot at VBM and CBM respectively (core diameter 4.7 Å). (g) Schematic representation of a core-shell nanowire field effect transistor. (Reprinted with permission from M. Jaishi, and R. Pati, *Nanoscale* 2017, 9, 13425–13431. Copyright (2017) Royal Society of Chemistry.)

the band decomposed charge density plots (Fig. 4.9c-f), which show a strong localization of wave function into the Ge-core region of the nanowire for the valence band maximum; for the conduction band minimum, the wave function is localized on the shell Si atoms. However, a vivid difference in band structure is noticeable between two nanowires as we move away from the high symmetry Γ point; Ge wave function contributes significantly to the conduction band edge near the X-point for the bigger Ge-core nanowire. In contrast, Si wave function dictates the conduction band for the smaller Ge-core nanowire. Since the main focus of this investigation is to unravel the functionality of the Ge-Si core-shell nanowire FET at the electronic level, we construct a prototypical nanowire junction by

sandwiching a finite segment of the optimized $\langle 110 \rangle$ Ge-Si core-shell nanowire between a pair of semi-infinite gold electrodes (Fig. 4.9g); two representative junctions are modeled using nanowire channels of different core diameters with the electrode to electrode distance of ~ 2 nm. To mimic the nanowire junction in experimental measurement, and to circumvent the problem associated with the conductivity mismatch and charge trapping at the nanowire/lead interface, we passivated the unsaturated dangling states by hydrogen atoms at the interface as done for the unsaturated surface states of the nanowire. We term the core-shell nanowire channel as a quantum dot from here on due to confinement of electrons. As the nanowire quantum dot (QD) is allowed to exchange its energy and electrons with the semi-infinite leads upon contact, the junction constitutes an open system.

Subsequently, we recourse to a quantum transport approach [75, 76] to calculate the gate bias dependent electronic current in the open Ge-Si core-shell nanowire QD junction. The key quantity in this approach is the retarded many-body Greens function of the open nanowire QD-metal junction [42, 72, 75, 76, 110, 117–119] that includes the effect of applied bias, charging/broadening effects due to coupling with the semi-infinite electrode, and the electrostatic gating effect. As typically done, we divide the nanowire junction into two regions[75, 76]. The first part is the active scattering region, which consists of the core-shell nanowire QD and a finite number of gold atoms (24 gold atoms) from the contacts to include the charging effect on the nanowire. The second part is the semi-infinite gold electrode part, which is assumed to be unperturbed (retain its 3D bulk properties) when the scattering region is connected to the electrode; the active scattering part is open to the

semi-infinite electrodes through the bias dependent self-energy function[75, 76]. Electron-electron interaction in this many-body system is explicitly taken into account through the use of an orbital-dependent, *posteriori* hybrid density functional method (B3LYP) (see section 2.11) [70] that partially removes the self-interaction error by including part of the exact Hartree-Fock exchange interaction. This method has been found to provide a much better description of the transmission than that obtained with conventional, orbital-free local density functional approximation (LDA) or generalized gradient corrected approximation (GGA) (see section 2.9 & 2.10)[76]. A LANL2DZ pseudo potential Gaussian basis set[70] that includes scalar relativistic effects is used to describe the Ge and Si atoms in the device including the gold atoms from the lead; terminal H atoms are described by all-electron 6-311g* Gaussian basis set[70]. The dimension of the Hamiltonian matrix of the active scattering region is 3044×3044 for both the prototypes considered here. A single particle dipole interaction term $\vec{\epsilon}_g \cdot \sum_i \vec{r}(i)$ is included in the core Hamiltonian to mimic the electrostatic gating effect[76, 77]. $\vec{\epsilon}_g$, is the gate field applied in the direction perpendicular to the current carrying axis (x-axis) and $\vec{r}(i)$ is the coordinate of the i^{th} electron. The convergence criteria for energy, maximum density, and root mean square density are set to 10^6 , 10^6 , and 10^8 au respectively to ensure tight convergence during the self-consistent calculation; ultra-fine 99,590 pruned grids are used for numerical integration. The self-consistent inclusion of the dipole interaction term in the Hamiltonian allows us to include the first and higher order Stark effects, which are essential to examine non-linear transport phenomena[76, 77, 117]. The gate bias is obtained from the self-consistent voltage drop across the radial direction

of the nanowire for each applied \vec{E}_g . The Fermi energy of the active scattering region of the device is aligned with that of the bulk gold at equilibrium (the configuration where the left and right leads are at equal potential)[75, 76]. Coherent single particle scattering approach[42, 72] is used to calculate the gate bias dependent electronic current. The details of our method can be found in our peer-reviewed journal articles[75, 76].

4.3.2 Results and Discussion

4.3.2.1 Current-Voltage Characteristics

Fig. 4.10 shows the calculated current-voltage characteristics of the core-shell nanowire QD FETs for two representative channel structures (Fig. 4.8). In both cases, our calculations yield typical FET features with the source-drain currents (I_{ds}) rising initially and then saturating (ON-state) with the increase of applied bias (Fig. 4.10a and c) as observed in the experiment[8]. This non-linear behavior in I_{ds} persists for the entire gate bias range that we have considered here. However, as the gate bias increases beyond a threshold value (V_g^{th}), we find that the saturation current decreases. To further illustrate this intriguing finding, we plot the I_{ds} as a function of V_g for the fixed source-drain bias (Fig. 4.10b and d). First, we focus on a smaller gate bias range ($V_g < 2$ V). For a fixed V_{ds} , no appreciable change in I_{ds} is noticeable with the variation of V_g . When we increase the gate bias ($V_g > 2$ V), an upsurge in I_{ds} is seen until the gate bias reaches the V_g^{th} following which the drain current

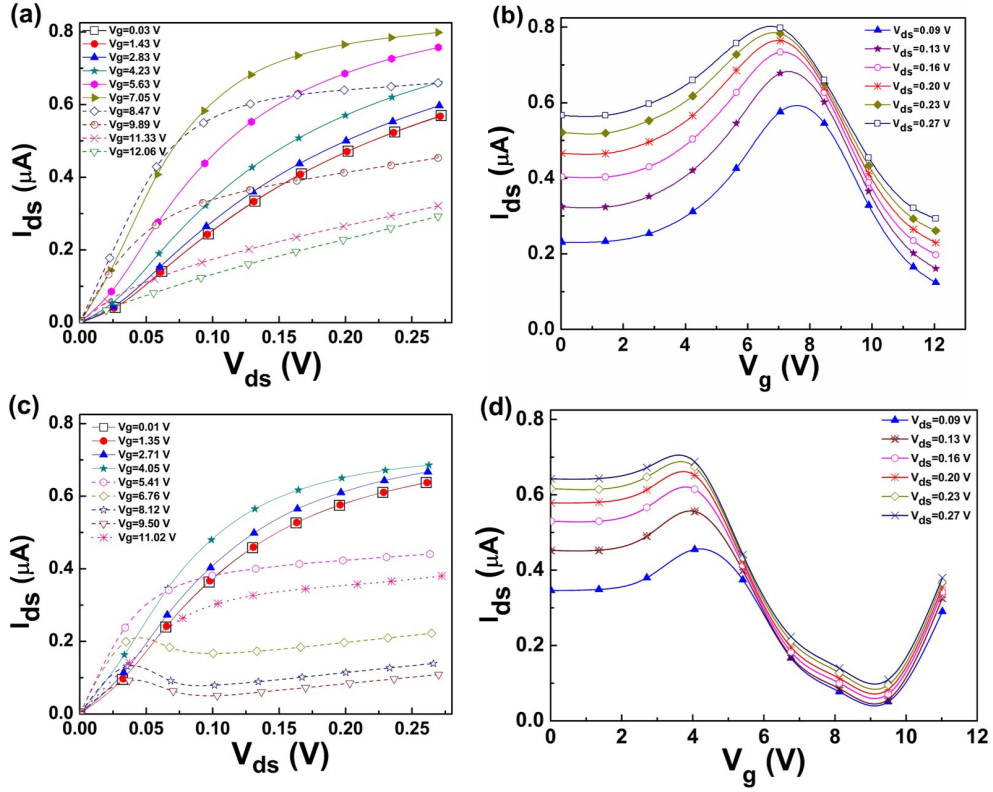


Figure 4.10: Current (I)-Voltage (V) characteristics of the transistor. (a, b) Ge-Si core-shell nanowire quantum dot FET with a core diameter of 11.7 Å. (c, d) Ge-Si core-shell nanowire quantum dot FET with a core diameter of 4.7 Å. (Reprinted with permission from M. Jaishi, and R. Pati, *Nanoscale* 2017, 9, 13425–13431. Copyright (2017) Royal Society of Chemistry.)

decreases rapidly to reach a valley point, resulting in a gate-bias-driven negative differential resistance (NDR) behavior. Both nanowire QD FETs exhibit the similar NDR feature in drain current. It is important to note here that the experimental transfer characteristics recorded from the Ge-Si core-shell nanowire FETs with much longer channel lengths of 1 μm and 190 nm also indicate rapid drops in I_{ds} with the increase of gate bias[8]; further increase of gate bias yields an increase in I_{ds} . Though we cannot make a quantitative comparison between our result and the experimental observation due to the much smaller size of the channel in our model, the rapid drop in I_{ds} with the increase of gate bias in our results

is similar to the observed decrease in drain current from the experimental measurement[8]. This remarkable agreement between our results and the experimental observation provides good confidence in the ability of our approach in describing a three-terminal nanowire FET. In the case of nanowire channel with a bigger Ge-core diameter, the V_g^{th} is found to be 7.05 V (Fig. 4.10b) and the peak to valley current ratio (PVR) varies from 4.65 to 2.72 with the increase of bias from 0.09 V to 0.27 V; for the smaller Ge core, V_g^{th} is found to be 4.05 V and PVR varies from 8.99 to 6.28 for the same applied bias range (Fig. 4.10d). We also did calculations at a low V_{ds} of 0.08 V which reveal a high PVR value of ≥ 18.87 when we increase the channel length of the smaller Ge-core FET from ~ 2 nm to ~ 2.44 nm; the result is shown in Figure 4.11b.

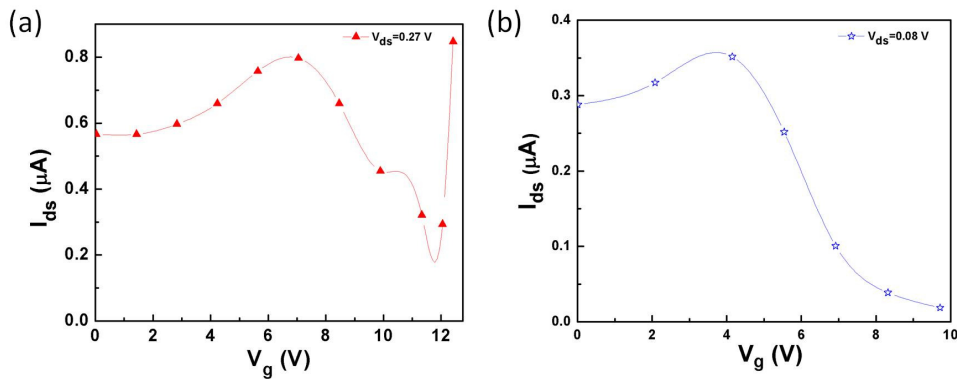


Figure 4.11: Drain current vs. Gate voltage plot at a fixed source-drain bias in a Ge-Si core-shell nanowire FETs; (a) Ge-core diameter 11.7 Å, and (b) Ge-core diameter 4.7 Å. (Reprinted with permission from M. Jaishi, and R. Pati, *Nanoscale* 2017, 9, 13425–13431. Copyright (2017) Royal Society of Chemistry.)

This clearly suggests that the threshold gate bias required to reach the peak current state as well as the PVR value in the nanowire QD FET can be tuned by changing the Ge core

diameter of the channel, which is also evident from the distinct valence band offsets found between Ge and Si for different core diameter (Fig. 4.9); channel length dependent study reveals that the PVR value can be substantially enhanced by increasing the channel length of the transistor. We note here that the PVR values presented here should represent the lower bound as the actual valley currents could be lower with a finer step size in the applied gate bias. The drop in PVR value with the increase of applied bias in our calculation is also in qualitative agreement with the experimental observation [8] that indicates a drop in ON/OFF current ratio with the increase of applied bias.

4.3.2.2 Transconductance and Transmission

To corroborate the observed anomalous behavior in I_{ds} with applied gate bias, we have calculated the transconductance ($g_m = dI_{ds}/dV_g$)[117] using the data plotted in Fig. 4.10b and d. The results are summarized in Fig. 4.12. Though the values of g_m vary from one device to the other, both FETs exhibit switching in the sign of transconductance. In the case of the FET with a bigger Ge-core channel (Fig. 4.12a), g_m switches sign from positive to negative at a higher gate bias as compared to the smaller Ge-core channel (Fig. 4.12c), which reconfirms our previous observation. To understand the origin of gate bias driven NDR and switching in the sign of g_m , we have calculated the gate bias dependent transmission function; I_{ds} is obtained by integrating the transmission function within the chemical potential window. For brevity, we have only considered the peak (ON) and the

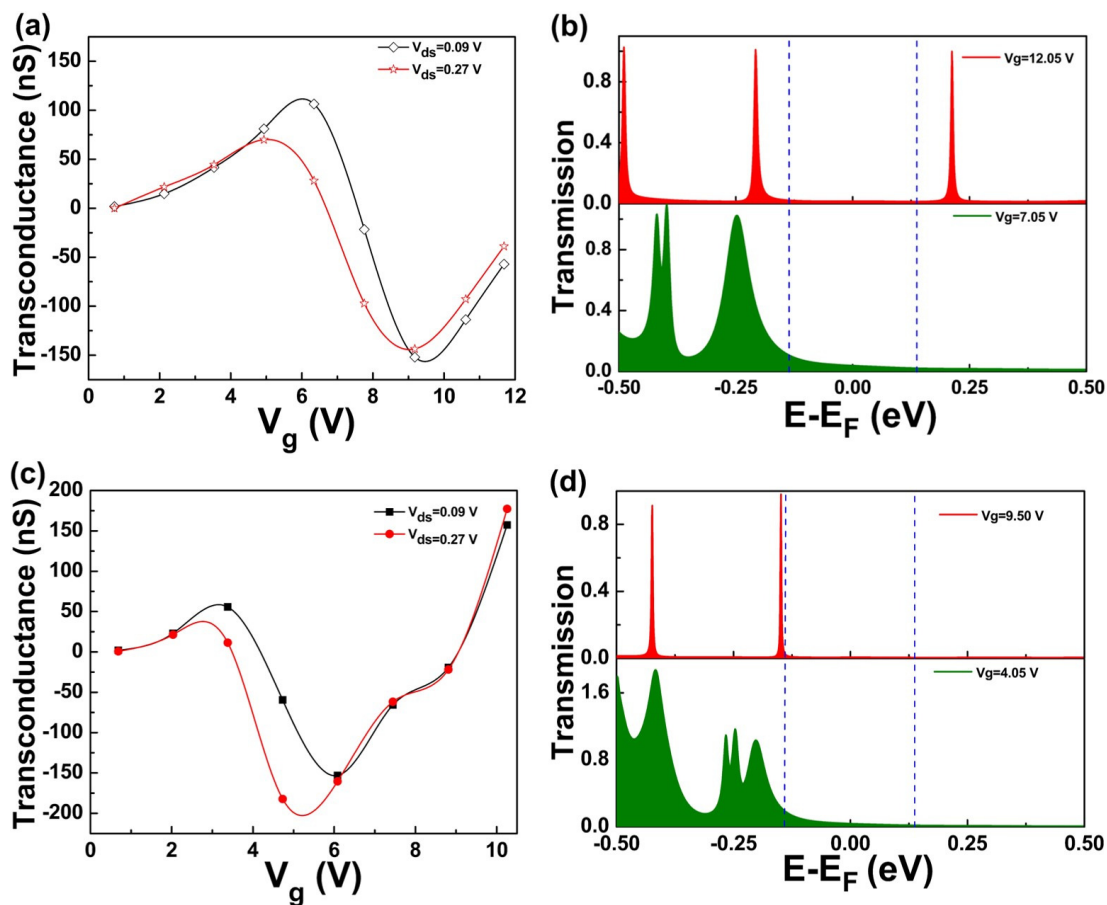


Figure 4.12: Transconductance and transmission function in two representative nanowire junctions. Gate bias dependent transmission is plotted at a fixed source-drain bias of $V_{ds} \sim 0.27$ V; dotted lines represent the chemical potential window. (a, b) Ge-Si core-shell nanowire quantum dot FET with a core diameter of 11.7 Å. (c, d) Ge-Si core-shell nanowire quantum dot FET with a core diameter of 4.7 Å. Lower panels in the transmission plots represent the ON states and upper panels represent the OFF states. (Reprinted with permission from M. Jaishi, and R. Pati, *Nanoscale* 2017, 9, 13425–13431. Copyright (2017) Royal Society of Chemistry.)

valley (OFF) current states at a low applied bias of 0.27 V. From the transmission plot (Fig. 4.12b and d), several features are clearly noticeable. First, both nanowire FETs exhibit similar characteristic with much-broadened transmission peaks for the ON state and sharper peaks for the OFF state. Second, none of the transmission peaks appear within the low bias electrochemical potential energy window (CPW) considered here. However, the

higher contribution from the tail end of the broadened transmission peak within the CPW leads to a much higher current for the ON state. We should note that the transmission peaks that are contributing to the current are from the frontier eigenstate with energy smaller than the Fermi energy. A closer examination of the transmission within the CPW reveals that the ratio of transmission coefficients between the ON and the OFF state is much higher in the smaller Ge core-channel than that in the bigger Ge-core, which reaffirms our finding of higher PVR value in the smaller Ge-core FET. Next, we turn our focus to the high gate bias regime beyond the OFF state. A sharp increase in drain current upon increasing gate bias is noticeable for the smaller Ge-core FET. To understand this, we analyze the transmission function at $V_g = 11.02$ V for the smaller Ge-core channel. Comparing the transmission at the valley current state ($V_g = 9.5$ V) to that at $V_g = 11.02$ V, we find that the transmission peak height in the vicinity of Fermi energy decreases upon increasing the gate bias. However, the shift in transmission peak position into the CPW upon increasing gate bias from 9.5 V to 11.02 V results in a sharp increase in drain current. A similar behavior in drain current is observed for the higher gate bias beyond the valley point in the case of the larger Ge core FET as shown in Figure 4.11a and 4.13a.

4.3.2.3 Role of Frontier Orbitals and Interfacial Coupling

To gain a deeper insight into the origin of observed transmission feature between the ON state and the OFF state, we have analyzed the coefficient of highest occupied molecular

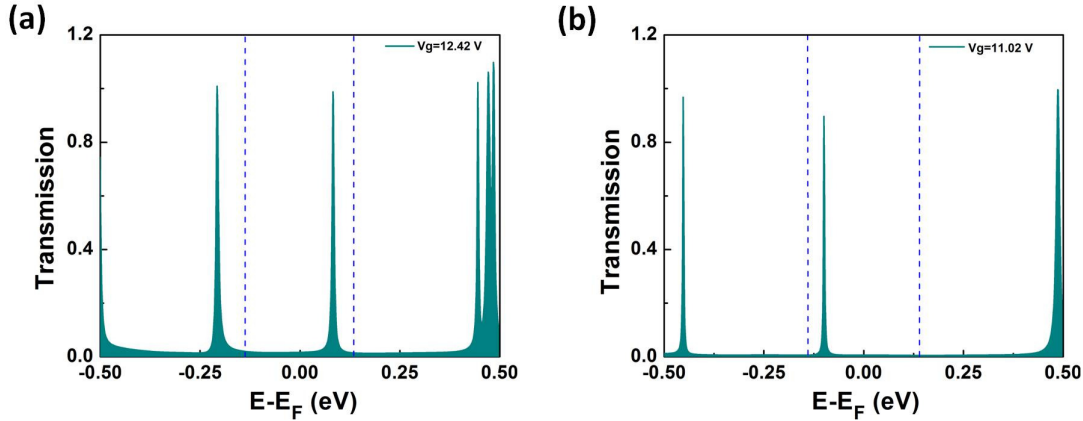


Figure 4.13: Gate bias dependent transmission at a fixed source-drain bias of V_{ds} (0.27 V) in Ge-Si core-shell nanowire FETs. (a) Ge-core diameter is 11.7 Å, (b) Ge-core diameter is 4.7 Å; dotted lines represent the chemical potential window. (Reprinted with permission from M. Jaishi, and R. Pati, *Nanoscale* 2017, 9, 13425–13431. Copyright (2017) Royal Society of Chemistry.)

orbital in the active scattering region (at respective gate bias points) that contributes to the transmission within the CPW for both the FETs. For the ON state, the dominant contribution comes from the p_z orbitals of the Ge atoms at the core/shell interface and s-orbitals of the Au lead; the electronic coupling between the s states and p_z states at the lead/nanowire interface is responsible for the strong broadening in transmission spectra. A closer examination reveals the p_z orbitals that form a channel along the current carrying axis (z-axis) provide the most probable tunneling pathway for electrons as shown in Fig. 4.14a.

It should be noted that in the case of a Si-Ge core-shell nanowire FET[117], though we did not find gate bias driven NDR feature as revealed here (for the same gate bias range), we found a similar behavior with p_z orbitals of the shell Ge forming a channel for electron tunneling at the ON state. This unambiguously establishes that the observed high performance behavior in Ge-Si or Si-Ge core-shell nanowire FET is dictated by the electron

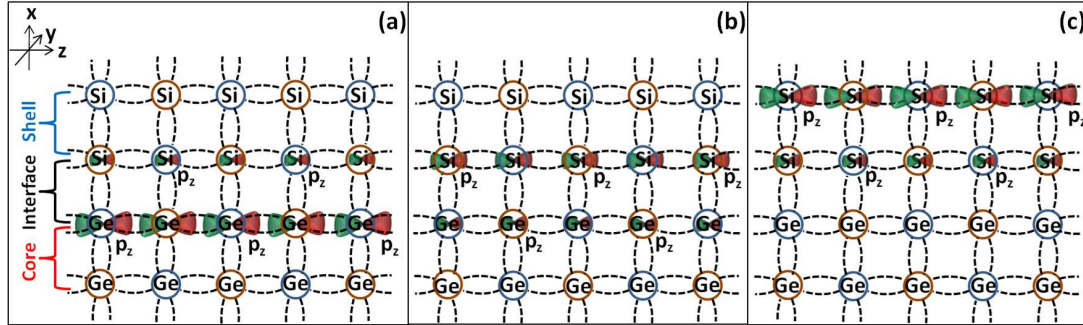


Figure 4.14: Decoupling of carrier transport. Schematic illustration of the gate biased induced decoupling of electron transport between the core and shell region of the Ge-Si core-shell nanowire channel in the x - z plane; z -axis is the current carrying axis; gate field is applied along the x -axis; alternative atoms are in different planes. (a) Peak state of the current (ON state): p_z orbital of the Ge atom at the core-shell interface provides the most probable tunneling pathway for carrier transport. (b) One of the intermediate states between the ON and OFF states shows the decreased participation of Ge with the increase of gate bias. (c) Valley state of the current (OFF state): p_z orbital at the shell Si atom provides the current path; core Ge atoms do not participate in tunneling. (Reprinted with permission from M. Jaishi, and R. Pati, *Nanoscale* 2017, 9, 13425–13431. Copyright (2017) Royal Society of Chemistry.)

tunneling through the p_z orbitals of the Ge layer and the Ge offers a low barrier height at the nanowire/lead interface in the ON state. Upon increasing the gate bias beyond the ON state, the gate field induced transverse localization of wave function along the x -axis (axis for the applied gate field) restricts the participation of Ge atoms in electron tunneling (Fig. 4.14b). For the OFF state, the molecular orbital that contributes to transmission is localized on the outer Si atoms of the shell layer (Fig. 4.14c) with almost no contribution from the gold resulting in a much weaker electronic coupling and large tunneling barrier between the nanowire and lead. This explains why we observe sharp transmission peaks for the OFF state. We thus can conclude that the gate bias induced decoupling of carrier transport between Ge-core and Si-shell is responsible for the observed NDR feature in Ge-Si core-shell nanowire QD FET.

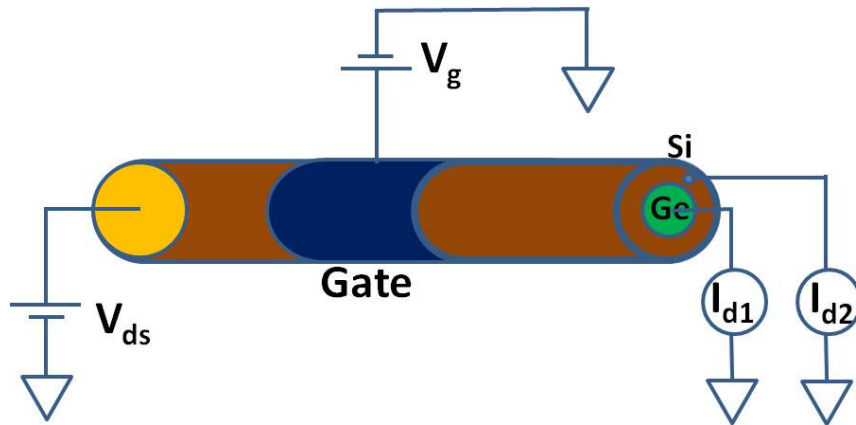


Figure 4.15: Sketch of the proposed experiment. Plausible four probe junctions for studying gate bias induced decoupling of carrier transport in co-axially gated Ge-Si core-shell nanowire junction. I_{d1} refers to the drain current from the Ge core and I_{d2} refers to the drain current from the Si shell of the nanowire. (Reprinted with permission from M. Jaishi, and R. Pati, *Nanoscale* 2017, 9, 13425–13431. Copyright (2017) Royal Society of Chemistry.)

A new experiment based on four-probe junctions with coaxial gating (Fig. 4.15) is proposed to validate our conclusion on decoupling of carrier transport between the core and the shell layer; the comparison of measured drain currents I_{d1} and I_{d2} at different gate bias would provide quantitative insights into the carrier decoupling in the Ge-Si core-shell nanowire channel.

4.3.2.4 Conclusions

In summary, we have used an exhaustive quantum transport approach to unravel the electronic quantum path in real space within a Ge-Si core-shell nanowire transistor in a nonequilibrium condition, which demonstrates, unambiguously, the gate bias induced carrier decoupling between the core and shell region of the nanowire. At the peak NDR state,

the p_z -orbital of the core Ge layer is found to strongly couple with the s -orbital of the gold electrode which results in a higher value of current, whereas, no such hybridization at the interface is found exist at the valley NDR state, which is contributed solely from the p_z -orbital in the shell Si-layer. We expect our present findings should solidify the core-shell nanowire technology, where controlled transport of electrons holds the key for their multifunctional usages such as in next-generation electronics and quantum computing.

Chapter 5

Tunnel Magnetoresistance in a Three Terminal Carbon Nanotube Junction

5.1 Introduction

Tunnel magnetoresistance (TMR) which underpins the modern high-density data storage device comes into effect due to the relative difference in resistance between the parallel and antiparallel spin configurations of the ferromagnetic electrodes with a semiconductor or an insulator tunneling channel sandwiched between them[120–123]. To build such a spin tunneling junction requires the channel material with a long spin-flip scattering length[31]; this is essential for maintaining the coherent transport of electron spin through the channel

of the magnetic tunnel junction (MTJ). Carbon nanotube (CNT), in this regard, is found to adequately fulfill the requirement by having a negligible spin-orbit coupling owing to its low atomic number. Also, the abundant isotope of carbon, carbon-12, is not affected by the magnetic hyperfine interaction due to the absence of any unpaired electron. These excellent features make semiconductor CNT, an ideal candidate for the channel in a MTJ[31]. For example, a long spin-flip scattering length of 130 nm has already been reported in a ferromagnetically contacted CNT tunnel junction[31]. The phase coherence length of 250 nm and the elastic scattering length of 60 nm have also been observed in a ferromagnetically contacted CNT junction[32]. Exploiting this CNT feature, several experimental groups have, so far, measured the TMR in two and three terminal MTJs built out of CNT[31, 33–40]; however, the difficulties in fabricating the reproducible ferromagnetic contacts have led to a wide variation in the measured TMR values[31, 33–40]. Of particular interest is an experimental result published by Sahoo et al. in 2005, where they have shown an oscillatory TMR behavior in three terminal CNT junctions contacted with ferromagnetic PdNi electrodes[37]. In this work, they have reported the TMR measurements in single and multi-wall CNT based MTJs with both of them showing the *aperiodic* oscillatory TMR coupled with multiple sign reversals[37]. The ability to control this intriguing TMR feature in a predictable manner could potentially lead to its multifunctional usages, however, what causes the CNT based MTJs to exhibit such an unusual TMR feature is still far from being known. Though quantum interference has been suggested to be the primary reason[37], no quantum mechanical description has, yet, been outlined to explain the observed oscillations

in TMR. In the following, using the real space density functional theory (DFT) in conjunction with the single particle many-body Green's functions approach, we have investigated the gate field driven magnetoresistive effects in an (8,0) single-wall carbon nanotube-nickel (SWCNT-Ni) MTJ. Irrespective of different source-drain bias, our calculations conform to the experimentally reported oscillatory TMR feature[37] accompanied by a wide variation in amplitude and TMR sign reversals. Within the considered gate bias range, calculated current in parallel (PC) and antiparallel (APC) configuration show a nonlinear behavior with crossovers between them noticed at multiple gate-bias points. Further analysis has revealed a much higher value of polarizability along the gate field applied y-axis for both PC and APC leading to the second-order Stark effect which clearly explains the observed nonlinear PC and APC current. The majority and minority spin current contributions for PC and APC show the spin injection efficiency to decrease with the increase in source-drain bias applied along the channel axis. The gate bias dependent transmission and frontier orbitals in the active scattering region are analyzed to understand the observed aperiodic TMR oscillations. We found the hybridization at the interface between s - and d -orbitals of the Ni electrode and p_z -orbital of the interfacial carbon atoms to change with the increase in the gate bias. This gate modulated change in coupling with different interfacial atoms participating at different gate bias regime leads to the changes in the spin-transport pathways along the channel resulting in a nonlinear current behavior. Inserting an oxide layer at the interface has resulted in a substantial increase in TMR accompanied with a much smoother oscillations; the observed improvement in TMR oscillation can be ascribed to the greater

control achieved at the interface due to the insertion of aluminum oxide tunnel barrier.

5.2 Computational Methods

We have considered a semiconductor single-wall carbon nanotube (SWCNT) of chirality (8,0) for our study. The electronic structure calculation of (8,0) SWCNT is performed using the periodic density functional theory (DFT) that employs plane wave basis functions and generalized gradient approximation (GGA=PW91). The valence-core interaction is described by using the projector augmented wave (PAW) pseudopotential. For geometry optimization, the atomic structure of the nanotube is allowed to relax without symmetry constraint until the residual force on each atom becomes ≤ 0.01 eV/Å; the convergence criteria for total energy is set at 10^{-6} eV. We have used a k-mesh of $1 \times 1 \times 17$ under the Monkhorst pack scheme to sample the Brillouin zone. The kinetic energy cut-off of 29.40 Ry and a supercell comprised of 32 carbon atoms are considered. The lattice parameter after the geometry of (8,0) SWCNT is optimized is found to be 4.27 Å. The diameter of the relaxed (8,0) SWCNT is found to be ~ 0.64 nm which is quite reasonable since the CVD synthesis of freestanding SWCNT of about 0.426 nm has already been reported[124]. To minimize the spurious interaction between the nanotube and its replicas, a large supercell of 30 Å along the x- and y-axis with a vacuum space of more than 20 Å is considered.

Table 5.1 summarizes the structure of our optimized (8,0) SWCNT in cartesian coordinates.

Table 5.1

The optimized coordinates of the atoms in an (8,0) SWCNT unit cell.

Translational lattice parameter = 4.27 Å				
Serial Number	Atom	X(Å)	Y(Å)	Z(Å)
1	C	8.12194	5.62116	4.00512
2	C	8.12194	5.62116	1.15288
3	C	7.64794	6.76917	1.87018
4	C	7.64794	6.76917	3.28782
5	C	6.76917	7.64794	4.00518
6	C	6.76917	7.64794	1.15282
7	C	5.62116	8.12193	1.87011
8	C	5.62116	8.12193	3.28789
9	C	4.37884	8.12194	4.00512
10	C	4.37884	8.12194	1.15288
11	C	3.23083	7.64794	1.87018
12	C	3.23083	7.64794	3.28782
13	C	2.35206	6.76917	4.00518
14	C	2.35206	6.76917	1.15282
15	C	1.87807	5.62116	1.87011
16	C	1.87807	5.62116	3.28789
17	C	1.87806	4.37884	4.00512
18	C	1.87806	4.37884	1.15288
19	C	2.35206	3.23083	1.87018
20	C	2.35206	3.23083	3.28782
21	C	3.23083	2.35206	4.00518
22	C	3.23083	2.35206	1.15282
23	C	4.37884	1.87807	1.87011
24	C	4.37884	1.87807	3.28789
25	C	5.62116	1.87806	4.00512
26	C	5.62116	1.87806	1.15288
27	C	6.76917	2.35206	1.87018
28	C	6.76917	2.35206	3.28782
29	C	7.64794	3.23083	4.00518
30	C	7.64794	3.23083	1.15282
31	C	8.12193	4.37884	1.87011
32	C	8.12193	4.37884	3.28789

The band structure calculation performed by taking the optimized (8,0) SWCNT show a direct band gap of 0.58 eV at the Γ point which is found to be consistent with the results reported previously[125–127]. Fig. 5.1 shows the band structure plot of (8,0) SWCNT. We have used the codes employed in the Vienna *ab-initio* simulation package (VASP)[106,

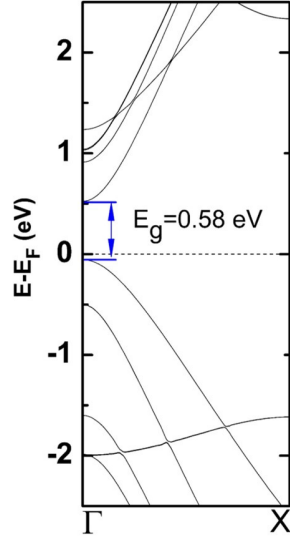


Figure 5.1: Band Structure plot of (8,0) SWCNT showing a fundamental gap of 0.58 eV at Γ point; the presence of a definite band gap ascertains the semiconductor behavior of (8,0) SWCNT.

107] to perform the periodic DFT calculation.

Then, we recourse to the spin-unrestricted *real space* DFT in conjunction with the spin-polarized coherent single particle many-body Green's functions approach to calculate spin transport in an (8,0) SWCNT-Ni MTJ. To construct the junction, a finite portion of CNT is sandwiched between the Ni source and drain electrodes; see section 3.3.3 of this thesis for a detail information of our method. Fig. 5.2 shows the schematic of a prototypical magnetic tunnel junction built out of semiconductor SWCNT for both PC and APC. For the real space electronic structure calculation, we used the *posteriori* hybrid DFT method (B3LYP) (see section 2.11 of this thesis for more details); an all-electron 6-311 G* [128] basis set is used for all the atoms in the active scattering region. A finite perturbative approach is used to include the source-drain as well as the gate bias effects self-consistently; see section 3.3

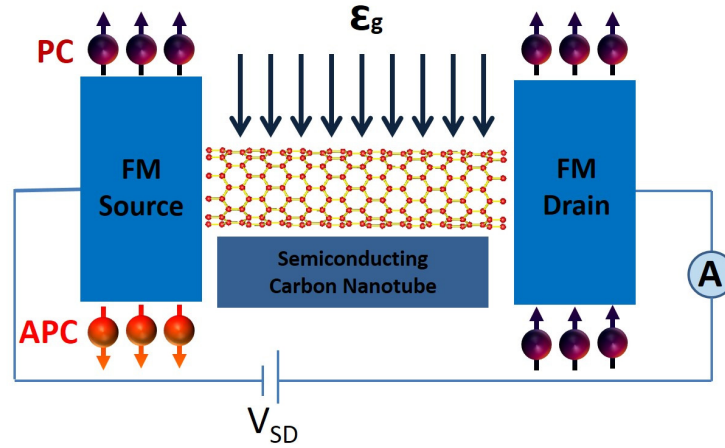


Figure 5.2: A three terminal (8,0) single-wall carbon nanotube-Ni magnetic tunnel junction; ϵ_g represents the gate field applied perpendicular to the channel axis. PC and APC refer to the parallel and antiparallel spin configuration of ferromagnetic source and drain electrodes.

of this thesis for further details. We have aligned the Fermi energy of the active scattering region with that of bulk Ni electrodes at equilibrium. The gate bias, V_g is obtained from the voltage drop across the radial direction for each applied gate field at equilibrium.

5.3 Results & Discussions

5.3.1 Magnetoresistance in CNT-based Tunnel Junction

Fig. 5.3 shows the calculated TMR for two different source-drain bias in an MTJ built out of semiconductor (8,0) SWCNT. The TMR is obtained using the expression $((I_{PC} - I_{APC})/I_{APC} \times 100 \%)$ [75]. Irrespective of different source-drain bias, we found

oscillations and sign reversals of the TMR with the increase of applied gate bias. It is important to note here that a similar TMR feature has already been reported experimentally in ferromagnetically contacted CNT junctions[37]. To explain this intriguing TMR features, we examined a representative case with $V_{DS} \sim 0.80$ V (Fig. 5.3a). The calculated TMR in the absence of gate bias (V_g) is found to be 22.32 % which is in agreement with the reported magnetoresistance of ~ 20 % in a two terminal CNT spin-valve junction[129].

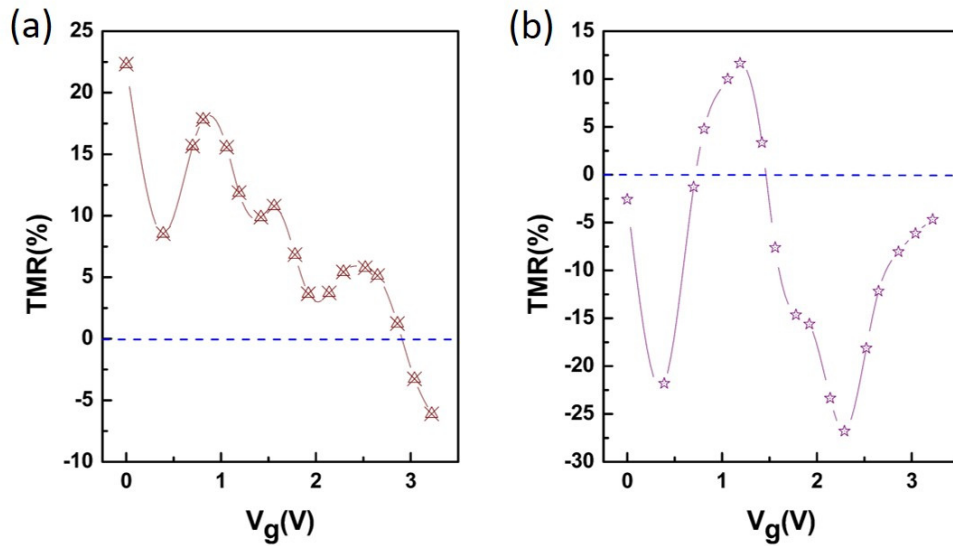


Figure 5.3: TMR in an MTJ built out of semiconductor (8,0) SWCNT. TMR is plotted as a function of gate bias for the fixed source-drain bias of (a) ~ 0.80 V and (b) ~ 1.55 V.

Upon increasing the gate bias from 0.0 V to 0.39 V, a rapid drop in TMR is noticed; a subsequent increase of V_g to 0.81 V causes a rise in TMR up to 17.82 %. Thereafter, a steady drop to 9.89 % is noticed in TMR following which it surges again to 10.78 % at $V_g=1.56$ V. This oscillatory TMR behavior persists as we go up to a higher gate bias; the sign reversal of TMR is seen at a higher gate bias. To ascertain the general nature

of the observed non-linear TMR feature, we calculated it again at a higher source-drain bias of ~ 1.55 V (Fig. 5.3b). Here, we found a negative TMR of -2.58 % at zero gate bias; upon increasing the gate bias, TMR is found to drop rapidly until it becomes -21.81 % at $V_g=0.39$ V following which it increases to a positive value of 11.65 % at $V_g=1.19$ V. A subsequent dip in TMR is observed again upon increasing the gate bias to higher values. This confirms that the gate-bias-driven oscillatory and sign reversal behavior of TMR in CNT junctions observed here is independent of applied source-drain bias. Despite a significant increase in amplitude along with multiple sign reversals in TMR noticed in our calculations for the higher source-drain bias (Fig. 5.3b), the oscillations in both cases ($V_{DS} \sim 0.80$ V (Fig. 5.3a) and $V_{DS} \sim 1.55$ V (Fig. 5.3b)) are found to be *aperiodic* in nature. This result is fully consistent with the *aperiodic* behavior of TMR reported in the experiment[37]. Though, quantitative comparison cannot be made between our results and the experiment[37] because of different length scales, chirality conditions as well as the lack of atomic-level structural information of the CNT/lead interfaces in the fabricated device, reproducing an oscillatory TMR feature as that of the experiment[37] provides confidence on the robustness of the our approach.

5.3.2 Current-Voltage Characteristics in (8,0) SWCNT-Ni MTJ

To analyze the oscillation and sign reversal TMR feature observed in a CNT-Ni MTJ, we have plotted the drain current (I_{DS}) as a function of gate bias (V_g) for both representative

configurations shown in Fig. 5.3. The current-voltage characteristics for the PC and APC are summarized in Fig. 5.4. Regardless of applied source-drain bias, I_{DS} vs. V_g plots (Fig. 5.4a & 5.4b) show a nonlinear behavior accompanied by crossovers between the PC and APC current. Examining the results from Fig. 5.4a, we found a higher current in PC (12.77 μA) than that of APC (10.44 μA) at $V_g=0.00$ V; this explains the higher positive value of TMR at zero gate bias (Fig. 5.3a). When we increase the gate bias to $V_g=0.39$ V, the current in the APC rapidly rises to 11.47 μA while a small drop in PC current to 12.45 μA is noticed; this results in a decrease in the difference between PC and APC current and hence, a smaller TMR value is noted at $V_g=0.39$ V (Fig. 5.3a). A subsequent increase in gate bias to $V_g=1.19$ V results in a rapid decrease of current in APC and a gradual drop in current for PC leading to a higher TMR value. An approximate in-phase behavior in PC and APC current is observed as we increase the gate bias to 2.65 V and 2.86 V respectively following which a crossover occurs at $V_g = -2.91$ V between the currents in PC and APC; this results in a negative TMR as shown in Fig. 5.3a. In the case of the higher source-drain bias (Fig. 5.4b), crossover between PC and APC currents are noted at several gate bias points resulting in multiple sign reversals and oscillatory behavior in TMR (Fig. 5.3b).

5.3.3 Spin-resolved Current-Voltage Characteristics

Since TMR is a spin-dependent phenomenon where both majority and minority spin carriers have their contributions in PC as well as APC current, a detailed analysis of the role

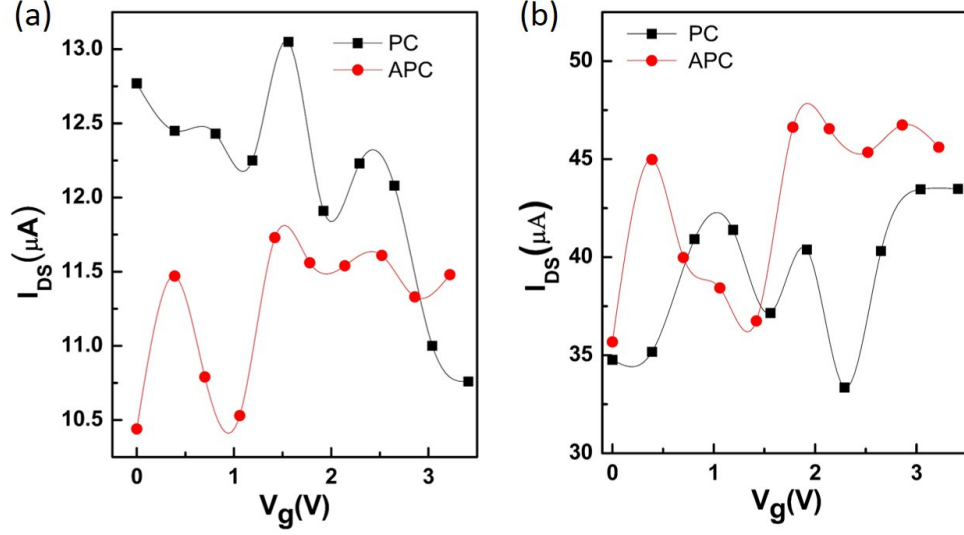


Figure 5.4: Current-voltage characteristics in an (8,0) SWCNT-Ni MTJ. Drain current (I_{DS}) is plotted as a function of gate bias (V_g) for the fixed source-drain bias of (a) ~ 0.80 V and (b) ~ 1.55 V; PC and APC refer to parallel and antiparallel spin alignments between the Ni electrodes.

played by these spin carriers would help to gain a deeper understanding of the observed TMR and spin behavior in CNT junction. The contributions from the majority and minority spin carriers to drain current as a function of gate bias is depicted in Fig. 5.5. For the source-drain bias of ~ 0.80 V (Fig. 5.5a), minority spin states' (Down) contribution is found to be appreciably larger than that of the majority states' (Up) in PC; the magnitude of spin injection factor, $\eta = (Up - Down)/(Up + Down)$, is found to be -0.22 at zero gate bias. While in the case of APC, the Up states' contribution is higher than that of the Down states' resulting in an η value of 0.20 at $V_g=0$ V. When we increase the source-drain bias from ~ 0.80 V to ~ 1.55 V (Fig. 5.5b), majority and minority spin states exchange their roles in PC; Up states' contribution to current is found to be higher than that of the Down states' over all the gate bias range considered here. The η values in PC and APC decreased to 0.01 and 0.08, respectively upon increasing the source-drain bias from ~ 0.80

V to ~ 1.55 V at zero gate bias. These observed values of η are much smaller than that found in a boron nitride nanotube-nickel junction[130], which suggests that an appropriate tunnel barrier at the CNT/Ni junction is necessary to boost the spin injection efficiency and TMR. A high TMR value varying from -80 % to 120 % has been observed [34–36, 131] in *weakly coupled* two terminal carbon nanotube based MTJs.

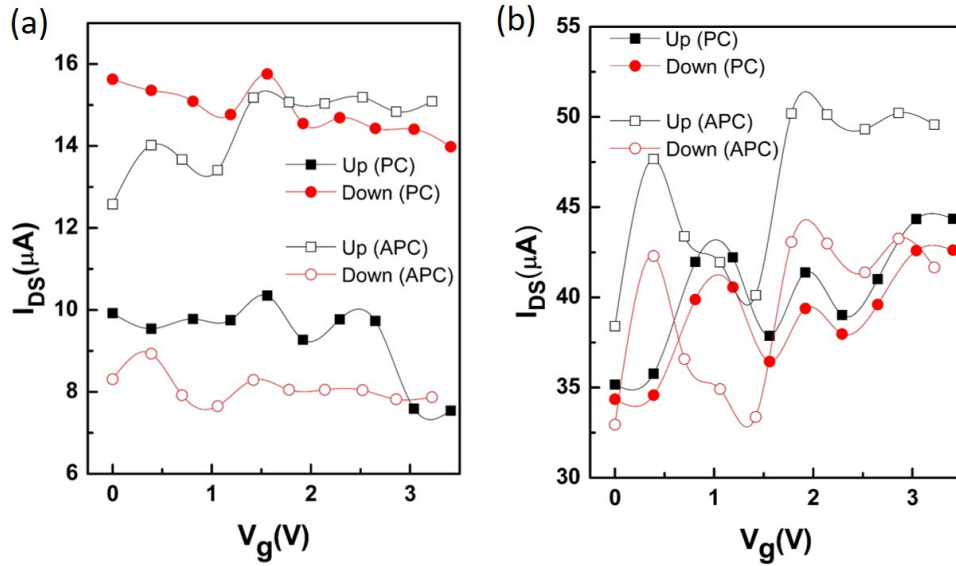


Figure 5.5: Spin-resolved current-voltage characteristics in an (8,0) SWCNT-Ni MTJ. Drain current (I_{DS}) contributions from the majority and minority spin carriers is plotted as a function of gate bias (V_g) for the fixed source-drain bias of (a) ~ 0.80 V and (b) ~ 1.55 V; Up and Down represent the respective drain current contributions from spin-up and spin-down electrons.

5.3.4 Multichannel Transmission Function

To understand the origin of the observed asymmetry between the majority and minority spin states' currents in PC as well as APC, we analyzed the multi-channel transmission function,

which is defined as the sum of transmission coefficients over all the eigenchannels; its integration within the chemical potential window gives us the drain current. For brevity, we have plotted the transmission as a function of injection energy for $V_{DS} \sim 0.80$ V at three different gate bias points; Fig. 5.6 shows the transmission plots within $[-0.5, 0.5]$ energy window for the majority and minority carriers in PC and APC. In the case of PC (Fig. 5.6a), Down-states' contribution to transmission is significantly higher than the Up-states in the vicinity of Fermi energy.

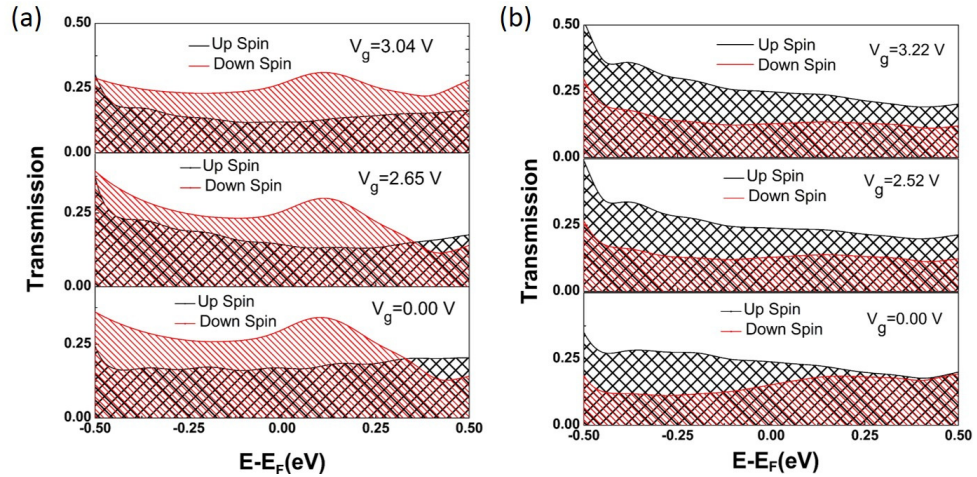


Figure 5.6: Spin-dependent transmission in a semiconductor SWCNT contacted with Ni electrodes. Transmission function is plotted at different gate bias for the fixed source-drain bias of ~ 0.80 V; (a) and (b) represent the majority (Up) and minority (Down) states' contribution to transmission in PC and APC, respectively.

This explains the higher observed spin-Down current in PC (Fig. 5.5a). When we increase the gate bias, the value of the transmission coefficient decreases in a non-linear way resulting in a decreasing Down-state current. However, in the case of APC (Fig. 5.6b), Up states' contribution is higher than that of the Down states resulting in a higher Up-state current; upon increasing gate bias, Up states' contribution to transmission increases leading to an

increase in the Up-state current. The observed broadening in transmission is due to the metal-induced broadening caused by strong chemical bonding at the channel-lead interface between the Ni atoms of the lead and the C-atoms of the nanotube channel.

5.3.5 Nonlinear Interfacial Coupling

Analysis of frontier spin orbitals in the active scattering part of the junction indicates a strong hybridization between the d - as well as s - states of Ni and the p - as well as s - states of C at the interface. A closer examination of the orbital coefficients reveals that different Ni atoms at the interface contribute to spin-dependent hybridization at different gate bias; some Ni atoms are strongly coupled to the interfacial C atoms than the others. The

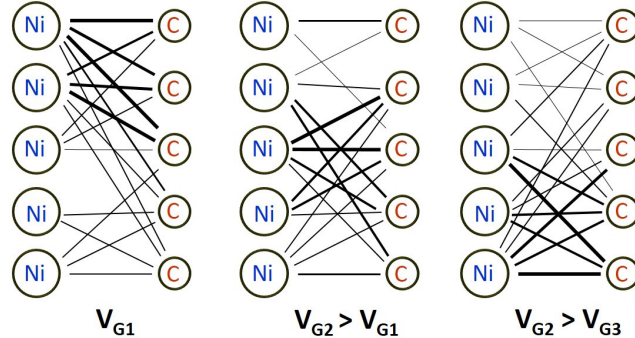


Figure 5.7: Schematic highlighting the distinct nature of the spin-dependent hybridization between the Ni and C atoms at the interface of the (8,0) SWCNT-Ni MTJ at different gate bias points. The width of the line indicates the strength of the coupling; V_{G1} , V_{G2} and V_{G3} refer to three different gate voltages.

schematic summarized in Fig. 5.7 highlights the nature of spin-dependent hybridization taking place at the CNT-Ni interface. Coupling change at the interface does not behave

Table 5.2

Dipole moment and polarizability. Components of dipole moment (α) and polarizability (β) in a CNT-Ni MTJ.

CNT-Ni junction	Dipole moment (a.u.)			Polarizability (a.u.)					
	α^x	α^y	α^z	β^{xx}	β^{yx}	β^{yy}	β^{zx}	β^{zy}	β^{zz}
PC	1.61	-0.05	0.09	1046.00	-158.52	1284.20	9.61	5.58	2932.18
APC	-0.43	0.04	-0.86	-618.24	-688.11	935.61	414.13	156.96	2835.90

linearly with applied gate bias due to the strong nonlinear Stark effect as evident from the calculated polarizability data (Table 5.2). The unique electron density distribution with distinct dipole moment and polarizability in PC and APC along the applied gate field direction (Y-axis) is responsible for the strong nonlinear response to the gate bias, which lead to an *aperiodic* oscillatory behavior of TMR in CNT-Ni MTJ.

5.3.6 Effects Induced by an Oxide Tunnel Barrier

Further investigations focused on achieving the predictable control over the observed oscillatory TMR feature is carried out by engineering a new junction structure with an aluminum oxide (Al_2O_3) tunnel barrier inserted at the CNT-Ni contacts. Fig. 5.8 summarizes the modulation of TMR and drain current due to Al_2O_3 tunnel barrier. For brevity, we have included only the results calculated at a source-drain bias 1.50 V. Within the considered gate bias range, TMR (Fig. 5.8a) is found to be entirely negative, however, the characteristic *aperiodic* nature of the TMR observed earlier is no more evident. For example, at $V_g = 0.00$ V, the TMR is found to be -7.68 % which goes down further to -84.66 % at

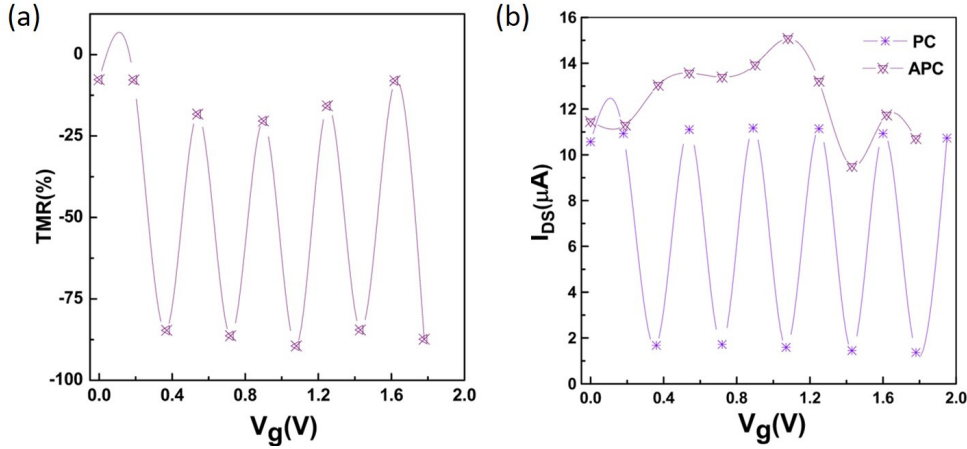


Figure 5.8: Tuning the spin-transport characteristics by inserting an Aluminum oxide (Al_2O_3) tunnel barrier at the (8,0) SWCNT-Ni contacts. (a) & (b) represent the respective TMR and I_{DS} vs. V_g plots at the $V_{DS} = 1.50$ V; PC and APC represent the parallel and antiparallel spin alignment of Ni electrodes.

a gate bias of 0.37 V beyond which the TMR is found to rise up again becoming -18.28 % at $V_g = 0.54$ V. A subsequent increase in gate bias causes a substantial drop in TMR reaching to similar a value observed at $V_g = 0.37$ V. This *periodic* oscillatory behavior is found to persists for the whole gate range considered in for our calculation. To substantiate the barrier modulated oscillatory TMR feature, we have analyzed the behavior of drain current for PC and APC within the same gate bias range (Fig 5.8b). In the absence of gate bias, we found the respective PC and APC currents to be 10.57 μA and 11.45 μA ; the slightly higher APC current explains the observed negative TMR of a smaller magnitude. Increasing the gate bias causes a dip in PC current while a smaller rise in APC is noted which justifies the TMR drop observed at $V_g = 0.37$ V; a similar consistency is observed for the rest of the gate bias range considered. While the current in APC behaves randomly for the complete gate bias range, the striking oscillatory behavior observed in PC current is

found to dominate the observed TMR feature. We expect this barrier modulated feature in TMR to persist regardless of source-drain bias applied along the channel axis. Achieving a predictable control over the oscillatory TMR feature is critical to its potential usages in various electronics applications.

5.4 Conclusions

We have found an *aperiodic* oscillatory TMR feature in a semiconductor (8,0) SWCNT-Ni magnetic tunnel junction which qualitatively agrees with the experimental TMR findings. Our *real space* DFT calculation revealed a distinct nature of hybridization at the CNT-Ni interface at each gate bias points responsible for the nonlinear spin tunneling behavior. The plausible removal of the observed *aperiodicity* in TMR oscillation is anticipated with the insertion of an insulating oxide tunnel barrier at the metal-semiconductor interface. We expect our theoretical result would provide a roadmap toward the predictable tuning of TMR in magnetic tunnel junctions for its multifunctional usages in next-generation electronics.

Chapter 6

Conclusions and Future Perspectives

6.1 Conclusions

This thesis describes the charge and spin-transport properties in one-dimensional nanoscale junctions using the first-principles density functional theory in conjunction with the coherent single particle many-body Green's functions (NEGF) approach. The first project of this thesis elucidates the superior performance of Si-Ge core-shell nanowire quantum dot field effect transistor (FET) in comparison to its pristine Si counterpart. In this work, we have identified the gate-modulated switching mechanism responsible for the superior FET performance of Si-Ge nanowire FET. For the on-state, the gate-field induced transverse localization of the wave function is found to restrict the carrier transport to the shell layer;

the p_z -orbitals provide the tunneling pathway for electrons through the channel in both Si-Ge and Si nanowires. The higher on-current observed in Si-Ge core-shell nanowire FET is explained by the distribution of p_z -orbitals over the entire channel of the device; for Si nanowire FET, the distribution of p_z - orbitals is found to be restricted to few shell-Si atoms leading to a smaller tunneling current. The Si-Ge nanowire FET is found to have a very high transconductance in comparison to Si nanowire suggesting higher values of mobility in Si-Ge nanowire junctions.

The second project of this thesis outlines the quantum transport properties of Ge-Si core-shell nanowire quantum dot FETs of two different Ge-core diameters. In this work, we have unlocked the most probable tunneling pathway for the electrons in Ge-Si nanowire FETs with the orbital-level resolution. Our calculations conform with the experimentally observed transport characteristics showing high-performance FET behavior below a certain threshold gate bias following which there is a gate-driven negative differential resistance (NDR) observed at higher gate bias. Our calculation revealed the gate-field induced decoupling of carrier transport between the core and shell regions of these nanowires, which clearly explains the observed gate-driven NDR; for peak state, the participatory p_z -orbitals in core-Ge layer is found to strongly couple with s -orbitals from the gold electrode while no such coupling at the nanowire/lead interface is observed for the valley current-state, which is contributed solely from the p_z orbitals in the shell Si-layer. We have proposed a four-probe experimental set-up to measure the drain current separately from the core and

the shell region in a surround gated Ge-Si core-shell nanowire junction to validate our prediction on the gate-induced decoupling of carrier transport between the core and the shell region.

In the final project of this thesis, we studied the spin transport in a semiconductor (8,0) single-wall carbon nanotube (SWCNT) contacted with ferromagnetic Ni electrodes. The spin-unrestricted DFT combined with the spin-polarized NEGF method is used to explore the magnetoresistive effects in a three-terminal CNT-Ni junction. Our calculations show an oscillatory tunnel magnetoresistance (TMR) accompanied by a sizable variation in width and amplitude with the increase in gate bias; TMR sign reversals are noted at higher gate bias. Though an exact comparison cannot be made between our theoretical results and experimental findings because of the lack of information regarding the interface structure, and chirality of the CNT as well as due to the difference in the length of the channel, our calculation holds a qualitative agreement with the results reported in the experiment. Our orbital-level analysis reveals a nonlinear spin-dependent hybridization at the interface between the *s*- and *d*- orbitals of the Ni electrodes and the p_z - orbitals of the interfacial carbon atoms in the channel; this non-linear variation in coupling at the interface is responsible for the oscillatory TMR behavior. Inserting an aluminum oxide layer as a tunnel barrier is found to result in a much smoother TMR oscillation by controlling the interaction at the nanotube/lead interface.

6.2 Future Perspectives — A bird's-eye view

Because of its unique electronic structure and quantum confinement effects, one-dimensional core-shell nanowires promise a wide range of functionalities in addition to its excellent charge transport feature. In regard to these possibilities, it would be worthy to extend the study of one-dimensional semiconductor core-shell nanowires considered in this thesis to explore some of the possible features described below.

1. First-principles DFT calculation of electronic thermal conductivity and phonon-dispersion relation to exploring the thermal transport features in $\langle 110 \rangle$ semiconductor Si-Ge and Ge-Si core-shell nanowires with and/or without doping.
2. Photo-voltaic applications of Si-Ge and Ge-Si core-shell nanowires by calculating the variation of absorption spectra with the photon energy for different lengths followed by the modeling of an appropriate Schottky junction to calculate the photocurrent density.
3. Spin transport in Si/Ge core-shell nanowire contacted to ferromagnetic junctions to explore the magnetoresistive effects for applications in next-generation electronics.

References

- [1] Waldrop, M. M. *Nature* **2016**, *530*, 144–147.
- [2] Editorial. *Nature* **2015**, *April 17*, *520*, 408.
- [3] Moore, G. E. *Electronics* **1965**, *38*(8), 114–117.
- [4] Moore, G. E. *IEDM Tech. Digest* **1975**, pages 11–13.
- [5] Markov, I. L. *Nature* **2014**, *512*, 147–154.
- [6] Lauhon, L. J.; Gudiksen, M. S.; Wang, D.; Lieber, C. M. *Nature* **2002**, *420*, 57–61.
- [7] Lu, W.; Xiang, J.; Timko, B. P.; Wu, Y.; Lieber, C. M. *PNAS* **2005**, *102*(29), 10046–10051.
- [8] Xiang, J.; Lu, W.; Hu, Y.; Wu, Y.; Yan, H.; Lieber, C. M. *Nature* **2006**, *441*, 489–493.
- [9] Xiang, J.; Vidan, A.; Tinkham, M.; Westervelt, R. M.; Lieber, C. M. *Nature Nanotechnology* **2006**, *1*, 208–213.
- [10] Lu, W.; Lieber, C. M. *Nature Materials* **2007**, *6*, 841–850.

- [11] Jiang, X.; Xiong, Q.; Nam, S.; Qian, F.; Li, Y.; Lieber, C. M. *Nano Letters* **2007**, *7*, 32143218.
- [12] Hu, Y.; Churchill, H. O. H.; Reilly, D. J.; Xiang, J.; Lieber, C. M.; Marcus, C. M. *Nature Nanotechnology* **2007**, *2*, 622–625.
- [13] Liang, G.; Xiang, J.; Kharche, N.; Klimeck, G.; Lieber, C. M.; Lundstrom, M. *Nano Letters* **2007**, *7*(3), 642–646.
- [14] Hu, Y.; Xiang, J.; Liang, G.; Yan, H.; Lieber, C. M. *Nano Letters* **2008**, *8*(3), 925–930.
- [15] Goldthorpe, I. A.; Marshall, A. F.; McIntyre, P. C. *Nano Letters* **2008**, *8*(11), 4081–4086.
- [16] Hao, X.-J.; Tu, T.; Cao, G.; Zhou, C.; H.-O., L.; Guo, G.-C.; Fung, W. Y.; Ji, Z.; Guo, G.-P.; Lu, W. *Nano Letters* **2010**, *10*, 2956–2960.
- [17] Zhao, Y.; Smith, J. T.; Appenzeller, J.; Yang, C. *Nano Letters* **2011**, *11*, 1406–1411.
- [18] Nah, J.; Dillen, D. C.; Varahramyan, K. M.; Banerjee, S. K.; Tutuc, E. *Nano Letters* **2012**, *12*, 108–112.
- [19] Moon, J.; Kim, J.-H.; Chen, Z. C. Y.; Xiang, J.; Chen, R. *Nano Letters* **2013**, *13*, 1196–1202.
- [20] Yan, H.; Choe, H. S.; Nam, S. W.; Hu, Y.; Das, S.; Klemic, J. F.; Ellenbogen, J. C.; Lieber, C. M. *Nature* **2011**, *470*, 240–244.

- [21] Dillen, D. C.; Kim, K.; Liu, E.-S.; Tutuc, E. *Nature Nanotechnology* **2014**, *9*, 116–120.
- [22] Zhang, L.; Tu, R.; Dai, H. *Nano Letters* **2006**, *6*(12), 2785–2789.
- [23] Parkinson, P.; Joyce, H. J.; Gao, Q.; Tan, H. H.; Zhang, X.; Zou, J.; Jagadish, C.; Herz, L. M.; Johnston, M. B. *Nano Letters* **2009**, *9*, 33493353.
- [24] Higginbotham, A. P.; Larsen, T. W.; Yao, J.; Yan, H.; Lieber, C. M.; Marcus, C. M.; Kuemmeth, F. *Nano Letters* **2014**, *14*, 3582–3586.
- [25] Fukata, N.; Yu, M.; Jevasuwan, W.; Takei, T.; Bando, Y.; Wu, W.; Wang, Z. L. *ACS Nano* **2015**, *9*(12), 1218212188.
- [26] Rocci, M.; Rossella, F.; Gomes, U. P.; Zannier, V.; Rossi, F.; Ercolani, D.; Sorba, L.; Beltram, F.; Roddaro, S. *Nano Letters* **2016**, *16*, 7950–7955.
- [27] Shahmohammadi, M.; Ganière, J.-D.; Zhang, H.; Ciechonski, R.; Vescovi, G.; Kryliouk, O.; Tchernycheva, M.; Jacopin, G. *Nano Letters* **2016**, *16*, 243249.
- [28] Conesa-Boj, S.; Li, A.; Koelling, S.; Brauns, M.; Ridderbos, J.; Nguyen, T. T.; Verheijen, M. A.; Koenraad, P. M.; Zwanenburg, F. A. ; Bakkers, E. P. A. M. *Nano Letters* **2017**, *17*, 22592264.
- [29] Wang, R.; Deacon, R. S.; Yao, J.; Lieber, C. M.; Ishibashi, K. *Semicond. Sci. Technol.* **2017**, *32*, 094002(1–11).

- [30] Hashemi, P.; Kim, M.; Hennessy, J.; Gomez, L.; Antoniadis, D. A.; Hoyt, J. L. *Appl. Phys. Lett.* **2010**, *96*(3), 063109.
- [31] Tsukagoshi, K.; Alphenaar, B. W.; Ago, H. *Nature* **1999**, *401*(6753), 572–574.
- [32] Bachtold, A. In *12th Int. Winter School on Electronic Properties of Novel Materials*; Kuzmany, H., Fink, J., Mehring, M., Roth, S., Eds., In proceedings; Am. Inst. Phys., New York, 1998; pages 65–68.
- [33] Mann, D.; Javey, A.; Kong, J.; Wang, Q.; Dai, H. *Nano Letters* **2003**, *3*, 1541–1544.
- [34] Zhao, B.; Mönch, I.; Vinzelberg, H.; Mühl, T.; Schneider, C. M. *Appl. Phys. Lett.* **2002**, *80*, 3144–3146.
- [35] Jensen, A.; Hauptmann, J. R.; Nygård, J.; Lindelof, P. E. *Phys. Rev. B* **2005**, *72*, 035419.
- [36] Dirnaichner, A.; Grifoni, M.; Prüfling, A.; Steininger, D.; Hüttel, A. K.; Strunk, C. *Phys. Rev. B* **2015**, *91*, 195402.
- [37] Sahoo, S. *An experimental investigation of spin polarized transport in carbon nanotubes* PhD thesis, University of Basel, **2005**.
- [38] Man, H. T.; Wever, I. J. W.; Morpurgo, A. F. *Phys. Rev. B* **2006**, *73*, 241401(R).
- [39] Preusche, D.; Schmidmeier, S.; Pallecchi, E.; Dietrich, C.; Hüttel, A. K.; Zweck, J.; Strunk, C. *J. Appl. Phys.* **2009**, *106*, 084314.

- [40] Morgan, C.; Metten, D.; Schneider, C. M.; Meyer, C. *Phys. Status Solidi B* **2013**, *250*, 2622–2626.
- [41] Parr, R. G.; Yang, W. *Density-Functional Theory of Atoms and Molecules*; Oxford University Press, New York, 1989.
- [42] Datta, S. *Electronic Transport in Mesoscopic Systems*; Cambridge University Press: Cambridge, UK, 1995.
- [43] Dhungana, K. B.; Jaishi, M.; Pati, R. *Nano Letters* **2016**, *16*, 3995–4000.
- [44] Jaishi, M.; Pati, R. *Nanoscale* **2017**, *9*, 13425–13431.
- [45] Roothan, C. C. J. *Rev. of Mod. Phys.* **1951**, *23*, 69–89.
- [46] Hartree, D. R. *The calculation of Atomic Structures*; John Wiley & Sons, New York, 1957.
- [47] Szabo, A.; Ostlund, N. S. *Modern Quantum Chemistry*; Dover Publications, Mineola, New York, 1996.
- [48] Hohenberg, P.; Kohn, W. *Phys. Rev.* **1964**, *136*, B864–B871.
- [49] Kohn, W. *Rev. Mod. Phys.* **1999**, *71*, 1253–1266.
- [50] Kohn, W.; Sham, L. J. *Phys. Rev.* **1965**, *140*, A1133–A1138.
- [51] Payne, M. C.; Teter, M. P.; Allan, D. C.; Arias, T. A.; Joannopoulos, J. D. *Rev. Mod. Phys.* **1992**, *64*, 1045–1097.

- [52] Burke, K. *J. Chem. Phys.* **2012**, *136*(15), 150901.
- [53] Becke, A. D. *J. Chem. Phys.* **1993**, *98*(7), 5648–5652.
- [54] Becke, A. D. *J. Chem. Phys.* **2014**, *140*(18), 18A301.
- [55] Perdew, J. P.; Burke, K.; Wang, Y. *Phys. Rev. B* **1996**, *54*, 16533–16539.
- [56] Oliveira, L. N.; Gross, E. K. U.; Kohn, W. *Phys. Rev. Lett.* **1988**, *60*, 2430–2433.
- [57] Carloni, P.; Rothlisberger, U.; Parrinello, M. *Acc. Chem. Res.* **2002**, *35*(6), 455–464.
- [58] Born, M.; Oppenheimer, R. *Annalen der Physik* **1927**, *389*(20), 457–484.
- [59] Slater, J. C. *Physical Review* **1929**, *34*, 1293–1322.
- [60] Sakurai, J. *Advanced Quantum Mechanics*, A-W series in advanced physics; Pearson Education, Incorporated, 1967.
- [61] Capelle, K. *arXiv:cond-mat/0211443* **2002**.
- [62] Thomas, L. H. *Math. Proc. Camb. Phil. Soc.* **1927**, *23*(5), 542548.
- [63] Dreizler, R. M.; Gross, E. K. U. *Density Functional Theory*; Springer-Verlag Berlin Heidelberg, 1990.
- [64] Ceperley, D. M.; Alder, B. J. *Phys. Rev. Lett.* **1980**, *45*, 566–569.
- [65] Perdew, J. P.; Burke, K.; Ernzerhof, M. *Phys. Rev. Lett.* **1996**, *77*, 3865–3868.
- [66] Grimme, S. *J. Comp. Chem.* **2004**, *25*(12), 1463–1473.

- [67] Grimme, S. *J. Comp. Chem.* **2006**, 27(15), 1787–1799.
- [68] Lee, C.; Yang, W.; Parr, R. G. *Phys. Rev. B* **1988**, 37, 785–789.
- [69] Vosko, S. H.; Wilk, L.; Nusair, M. *Can. J. Phys.* **1980**, 58(8), 1200–1211.
- [70] Stephens, P. J.; Devlin, F. J.; Chabalowski, C. F.; Frisch, M. J. *J. Phys. Chem.* **1994**, 98(45), 11623–11627.
- [71] Carroll, R. L.; Gorman, C. B. *Angew. Chem.* **2002**, 41(23), 4378–4400.
- [72] Di Ventra, M. *Electrical Transport in Nanoscale Systems*, Vol. 14; Cambridge University Press: Cambridge, New York, 2008.
- [73] De Broglie, L. *Found. Phys.* **1970**, 1(1), 5–15.
- [74] Sanvito, S. *Chem. Soc. Rev.* **2011**, 40, 3336–3355.
- [75] Mandal, S.; Pati, R. *ACS Nano* **2012**, 6(4), 3580–3588.
- [76] Mandal, S.; Pati, R. *Phys. Rev. B: Condens. Matter Mater. Phys.* **2011**, 84(5), 115306.
- [77] Dhungana, K. B.; Pati, R. *Appl. Phys. Lett.* **2014**, 104(4), 162404.
- [78] Landauer, R. *IBM J. Res. Dev.* **1957**, 1(3), 223–231.
- [79] Landauer, R. *J. Phys.: Cond. Mat.* **1989**, 1(43), 8099.
- [80] Binasch, G.; Grünberg, P.; Saurenbach, F.; Zinn, W. *Phys. Rev. B* **1989**, 39, 4828–4830.

- [81] Baibich, M. N.; Broto, J. M.; Fert, A.; Van Dau, F. N.; Petroff, F.; Etienne, P.; Creuzet, G.; Friederich, A.; Chazelas, J. *Phys. Rev. Lett.* **1988**, *61*, 2472–2475.
- [82] Parkin, S. S. P.; Kaiser, C.; Panchula, A.; Rice, P. M.; Hughes, B.; Samant, M.; Yang, S.-H. *Nature Materials* **2004**, *3*(12), 862–867.
- [83] Dhungana, K. B.; Pati, R. *JACS* **2014**, *136*(32), 11494–11498.
- [84] Jagadeesh, S. M.; Tiffany, S. S.; Taro, N. *J. Phys: Cond. Mat.* **2007**, *19*(16), 165202.
- [85] Fung, W. Y.; Chen, L.; Lu, W. *Appl. Phys. Lett.* **2011**, *99*, 092108(1–3).
- [86] Chang, H.-K.; Lee, S.-C. *Appl. Phys. Lett.* **2010**, *97*, 251912(1–3).
- [87] Lu, W.; Lieber, C. M. *J. Phys. D: Appl. Phys.* **2006**, *39*, R387R406.
- [88] Peng, X.; Tang, F.; Logan, P. In *Handbook of Nanomaterials Properties*; Bhushan, B., Luo, D., Schrickler, S. R., Sigmund, W., Zauscher, S., Eds.; Springer, 2014; chapter 2, pages 51–83.
- [89] Peng, X.; Tang, F.; Logan, P. *J. Phys.: Condens. Matter* **2011**, *23*(8), 115502.
- [90] Peköz, R.; Raty, J.-Y. *Phys. Rev. B: Condens. Matter* **2009**, *80*(7), 155432.
- [91] Park, J.-S.; Ryu, B.; Moon, C.-Y.; Chang, K. *Nano Letters* **2010**, *10*, 116121.
- [92] Yang, L.; Musin, R. N.; Wang, X.-Q.; Chou, M. Y. *Phys. Rev. B: Condens. Matter* **195325**, *77*(5), 195325.
- [93] Lee, H.; Choi, H. *Nano Letters* **2010**, *10*, 2207–2210.

- [94] Kim, J.; Lee, J. H.; Hong, K.-H. *J. Phys. Chem. Lett.* **2013**, *4*, 121–126.
- [95] Markussen, T. *Nano Letters* **2012**, *12*, 4698–4704.
- [96] Amato, M.; Palumbo, M.; Ossicini, S. *Phys. Rev. B: Condens. Matter Mater. Phys.* **2009**, *79*(4), 201302.
- [97] Peng, X.; Logan, P. *Appl. Phys. Lett.* **2010**, *96*(3), 143119.
- [98] Musin, R. N.; Wang, X.-Q. *Phys. Rev. B: Condens. Matter Mater. Phys.* **2004**, *92*(5), 165308.
- [99] Zhao, X.; Wei, C. M.; Yang, L.; Chou, M. Y. *Phys. Rev. Lett.* **2004**, *92*(4), 236805.
- [100] Peelaers, H.; Partoens, B.; Peeters, F. M. *Phys. Rev. B: Condens. Matter Mater. Phys.* **2010**, *82*(4), 113411.
- [101] Huang, S.; Yang, L. *Appl. Phys. Lett.* **2011**, *98*(3), 093114.
- [102] Trammell, T. E.; Zhang, X.; Li, Y.; Chen, L.-Q.; Dickey, E. C. *J. Cryst. Growth* **2008**, *310*, 3084–3092.
- [103] Liu, N.; Lu, N.; Yao, Y.-X.; Zhang, G.-P.; Wang, C.-Z.; Ho, K.-M. *J. Phys. D: Appl. Phys.* **2013**, *46*(5), 135302.
- [104] Shen, J.-N.; Wu, L.-M.; Zhang, Y.-F. *J. Mater. Chem. A* **2014**, *2*, 2538–2543.
- [105] Liu, N.; Zhang, L.; Chen, X.; Kong, X.; Zheng, X.; Guo, H. *Nanoscale* **2016**, *8*, 16026–16033.

- [106] Kresse, G.; Furthmüller. *J. Comput. Mater. Sci.* **1996**, *6*, 15–50.
- [107] Kresse, G.; Furthmüller. *J. Phys. Rev. B: Condens. Matter Mater. Phys.* **1996**, *54*(16), 11169–11186.
- [108] Nolan, M.; O’Callaghan, S.; Fagas, G.; Greer, J. C. *Nano Letters* **2007**, *7*, 34–38.
- [109] Waldron, D.; Haney, P.; Larade, B.; MacDonald, A.; Guo, H. *Phys. Rev. Lett.* **2006**, *96*(4), 166804.
- [110] Solomon, G. C.; Herrmann, C.; Hansen, T.; Mujica, V.; Ratner, M. A. *Nature Chemistry* **2010**, *2*, 223–228.
- [111] Wu, Y.; Cui, Y.; Huynh, L.; Barrelet, C. J.; Bell, D. C.; Lieber, C. M. *Nano Letters* **2004**, *4*, 433436.
- [112] Schmidt, V.; Senz, S.; Gösele, U. *Nano Letters* **2005**, *5*, 931935.
- [113] Sai, N.; Zwolak, M.; Vignale, G.; Di Ventra, M. *Phys. Rev. Lett.* **2005**, *94*(4), 186810.
- [114] Thygesen, K. S.; Rubio, A. *Phys. Rev. B: Condens. Matter Mater. Phys.* **2008**, *77*(22), 115333.
- [115] Martinez, J.; Martinez, R. V.; Garcia, R. *Nano Letters* **2008**, *8*, 36363639.
- [116] Pati, R.; McClain, M.; Bandyopadhyay, A. *Phys. Rev. Lett.* **2008**, *100*(4), 246801.
- [117] Dhungana, K. B.; Jaishi, M.; Pati, R. *Nano Letters* **2016**, *16*, 3995–4000.

- [118] Brandbyge, M.; Mozos, J.-L.; Ordejón, P.; Taylor, J.; Stokbro, K. *Phys. Rev. B* **2002**, 65(17), 165401.
- [119] Taylor, J.; Guo, H.; Wang, J. *Phys. Rev. B* **2001**, 63(13), 245407.
- [120] Julliere, M. *Phys. Lett. A* **1975**, 54, 225–226.
- [121] Slonczewski, J. C. *Phys. Rev. B* **1989**, 39, 6995–7002.
- [122] Moodera, J. S.; Kinder, L. R.; Wong, T. M.; Meservey, R. *Phys. Rev. Lett.* **1995**, 74, 3273–3276.
- [123] Fert, A. *Rev. Mod. Phys.* **2008**, 80, 1517–1530.
- [124] Takuya Hayashi, Y. A. K.; Matoba, T.; Esaka, M.; Nishimura, K.; Tsukada, T.; Endo, M.; Dresselhaus, M. S. *Nano Letters* **2003**, 3, 3.
- [125] Valavala, P. K.; Seel, M.; Pati, R. *Phys. Rev. B* **2004**, 70.
- [126] Zólyomi, V.; Kürti, J. *Phys. Rev. B* **2004**, 70.
- [127] Marzari, B. K. a. N. *Phys. Rev. Letters* **2006**, 96.
- [128] Gaussian 09, Revision B.01. Frisch, M. J.; Trucks, G. W.; Schlegel, H. B.; Scuseria, G. E.; Robb, M. A.; Cheeseman, J. R.; Scalmani, G.; Barone, V.; Mennucci, B.; Petersson, G. A.; Nakatsuji, H.; Caricato, M.; Li, X.; Hratchian, H. P.; Izmaylov, A. F.; Bloino, J.; Zheng, G.; Sonnenberg, J. L.; Hada, M.; Ehara, M.; Toyota, K.; Fukuda, R.; Hasegawa, J.; Ishida, M.; Nakajima, T.; Honda, Y.; Kitao, O.; Nakai,

H.; Vreven, T.; Montgomery, J. A.; Peralta, J. E.; Ogliaro, F.; Bearpark, M.; Heyd, J. J.; Brothers, E.; Kudin, K. N.; Staroverov, V. N.; Kobayashi, R.; Normand, J.; Raghavachari, K.; Rendell, A.; Burant, J. C.; Iyengar, S. S.; Tomasi, J.; Cossi, M.; Rega, N.; Millam, J. M.; Klene, M.; Knox, J. E.; Cross, J. B.; Bakken, V.; Adamo, C.; Jaramillo, J.; Gomperts, R.; Stratmann, R. E.; Yazyev, O.; Austin, A. J.; Cammi, R.; Pomelli, C.; Ochterski, J. W.; Martin, R. L.; Morokuma, K.; Zakrzewski, V. G.; Voth, G. A.; Salvador, P.; Dannenberg, J. J.; Dapprich, S.; Daniels, A. D.; Farkas.; Foresman, J. B.; Ortiz, J. V.; Cioslowski, J.; Fox, D. J. **2009**.

[129] Mehrez, H.; Taylor, J.; Guo, H.; Wang, J.; Roland, C. *Phys. Rev. Lett.* **2000**, *84*(12).

[130] Dhungana, K. B.; Pati, R. *Phys. Chem. Chem. Phys.* **2014**, *16*, 7996–8002.

[131] Samm, J.; Gramich, J.; Baumgartner, A.; Weiss, M.; Schönenberger, C. *J. Appl. Phys.* **2014**, *115*, 174309.

Appendix A

Copyrights

The copyright permission from the American chemical society for the article by K. B. Dhungana, M. Jaishi, and Ranjit Pati, *Nano Letters* 16, 3995-4000, (2016). The permission applies to chapter 4.



RightsLink®

[Home](#)
[Create Account](#)
[Help](#)


ACS Publications
Most Trusted. Most Cited. Most Read.

Title: Unlocking the Origin of Superior Performance of a Si-Ge Core-Shell Nanowire Quantum Dot Field Effect Transistor

Author: Kamal B. Dhungana, Meghnath Jaishi, Ranjit Pati

Publication: Nano Letters

Publisher: American Chemical Society

Date: Jul 1, 2016

Copyright © 2016, American Chemical Society

[LOGIN](#)

If you're a [copyright.com](#) user, you can login to RightsLink using your [copyright.com](#) credentials. Already a [RightsLink](#) user or want to [learn more?](#)

PERMISSION/LICENSE IS GRANTED FOR YOUR ORDER AT NO CHARGE

This type of permission/license, instead of the standard Terms & Conditions, is sent to you because no fee is being charged for your order. Please note the following:

- Permission is granted for your request in both print and electronic formats, and translations.
- If figures and/or tables were requested, they may be adapted or used in part.
- Please print this page for your records and send a copy of it to your publisher/graduate school.
- Appropriate credit for the requested material should be given as follows: "Reprinted (adapted) with permission from (COMPLETE REFERENCE CITATION). Copyright (YEAR) American Chemical Society." Insert appropriate information in place of the capitalized words.
- One-time permission is granted only for the use specified in your request. No additional uses are granted (such as derivative works or other editions). For any other uses, please submit a new request.

[BACK](#)
[CLOSE WINDOW](#)

Copyright © 2018 [Copyright Clearance Center, Inc.](#) All Rights Reserved. [Privacy statement](#). [Terms and Conditions](#). Comments? We would like to hear from you. E-mail us at customercare@copyright.com

Appendix B

Copyrights

The copyright permission from the Royal Society of Chemistry for the article by M. Jaishi, and R. Pati, *Nanoscale*, 9, 13425-13431, (2017). The permission applies to chapter 4.

 **Meghnath Jaishi** <mjaishi@mtu.edu>
to contracts-copy, ▾

Jan 8 (11 days ago) ☆ ↶ ▾

Dear Prof.,
I am writing to request the reuse of my full article published in the Nanoscale journal (Nanoscale, 2017, 9, 13425–13431) in one of the chapters of my Ph.D. dissertation. I would be highly grateful if you could provide a copyrights permission letter for the reuse of full article.
I would highly appreciate your help in this regard.
Thanks,

With Best Regards,
Meghnath Jaishi

⋮

Meghnath Jaishi
Graduate Student
Department of Physics
Michigan Technological University
Houghton, MI, 49931
[Email: mjaishi@mtu.edu](mailto:mjaishi@mtu.edu)
(906-281-8243)

 **CONTRACTS-COPYRIGHT (shared)** <Contracts-Copyright@rsc.org>
to me ▾

Jan 16 (3 days ago) ☆ ↶ ▾

Dear Meghnath

The Royal Society of Chemistry (RSC) hereby grants permission for the use of your paper(s) specified below in the printed and microfilm version of your thesis. You may also make available the PDF version of your paper(s) that the RSC sent to the corresponding author(s) of your paper(s) upon publication of the paper(s) in the following ways: in your thesis via any website that your university may have for the deposition of theses, via your university's Intranet or via your own personal website. We are however unable to grant you permission to include the PDF version of the paper(s) on its own in your institutional repository. The Royal Society of Chemistry is a signatory to the STM Guidelines on Permissions (available on request).

Please note that if the material specified below or any part of it appears with credit or acknowledgement to a third party then you must also secure permission from that third party before reproducing that material.

Please ensure that the thesis states the following:
Reproduced by permission of The Royal Society of Chemistry
and include a link to the paper on the Royal Society of Chemistry's website.

Please ensure that your co-authors are aware that you are including the paper in your thesis.

Regards
Gill Cockhead
Publishing Contracts & Copyright Executive

Gill Cockhead
Publishing Contracts & Copyright Executive
Royal Society of Chemistry,
Thomas Graham House,
Science Park, Milton Road,
Cambridge, CB4 0WF, UK
Tel [+44 \(0\) 1223 432134](tel:+44101223432134)

Follow the Royal Society of Chemistry:
www.rsc.org/follow

Winner of The Queen's Award for Enterprise, International Trade 2013